UNIVERSITY OF CALIFORNIA,
IRVINE

Liquid-Gas Heat and Mass Transfer at Supercritical Pressures

THESIS

submitted in partial satisfaction of the requirements
for the degree of

MASTER OF SCIENCE

in Mechanical and Aerospace Engineering

by

Jordi Poblador Ibanez

Thesis Committee:
Professor William A. Sirignano, Chair
Professor Derek Dunn-Rankin
Professor Said E. Elghobashi

2018

TABLE OF CONTENTS

LIST OF FIGURES

LIST OF TABLES

NOMENCLATURE

$[P_i]$	Parachor of species i
α_i, S_i	Functions in the SRK equation of state
Γ	Thermodynamic factor
λ	Thermal conductivity, W/(m K)
μ	Viscosity, kg/(ms)
ω_i	Acentric factor of species i
Φ_i	Fugacity coefficient of species i
ρ	Density, kg/m^3
σ_m	Surface tension of the mixture, N/m
A, B	Constants in the SRK equation of state
a_i, b_i	Attractive and repulsive parameter of species i
c	Growth rate of Kelvin-Helmholtz instability, 1/s
D	Fickian diffusion coefficients matrix, m^2/s
d_i	Driving force of species i due to diffusion of species, m^{-1}
D_{ij}	Binary diffusion coefficient between species i and j, m^2/s
f_i	Fugacity of species i
H	Enthalpy of the mixture, J
$h, \bar{h}$	Specific enthalpy and molar enthalpy of the mixture, J/kg or J/mole
$h_i, \bar{h}_i$	Specific enthalpy and molar enthalpy for species i, J/kg or J/mole
J_i	Diffusion mass flux of species i, kg/(m^{2}s)
k_{ij}	Binary interaction coefficient between species i and j

MW Molecular weight, kg/mole

N Number of species

p Pressure, Pa

R_u Universal gas constant, J/(K mole)

S Entropy of the mixture, J/K

s Specific entropy of the mixture, J/(kg K)

T Temperature, K

t Time, s

U Interface velocity, m/s

u Velocity, m/s

v Molar volume, m^3/mole

x Position or coordinate in the x-axis, m

X_i Mole fraction of species i

y Position or coordinate in the y-axis, m

Y_i Mass fraction of species i

Z Compressibility factor

Superscripts

$*$ Ideal gas property

M Mole-based

m Mass-based

Subscripts

c Critical property

g Gas phase

i Index for chemical species

l Liquid phase

r Reduced property

ACKNOWLEDGMENTS

I would like to thank Professor William A. Sirignano for having me in his team and guiding both me and this thesis during the past months. His expertise and passion about this field encourage me to pursue my objectives.

I would also like to thank Professor Derek Dunn-Rankin and Professor Said E. Elghobashi for finding time to be readers of this thesis. Their expertise and advise are always appreciated.

I would like to give special thanks to Professor Ahmed F. Ghoniem and his team members from the Massachusetts Institute of Technology for the helpful discussions about some topics of this thesis.

I am especially grateful to Professor Roger H. Rangel for giving me the opportunity to come to UCI and Dr. Pete Balsells for starting the Balsells Fellowship program, helping young catalan engineers bloom.

Finally, I also would like to thank all those people close to me. Arash and Albert, thank you for your warm welcome and all the help you have provided me during the development of this thesis. Irene, thank you for your support and patience. This wouldn't have been possible without you. Thank you Balsells fellows for sharing your days with me in those endless coffees and lunches. And thank you my family and old friends, for being here and 6,000 miles away at the same time. I miss you.

ABSTRACT OF THE THESIS

Liquid-Gas Heat and Mass Transfer at Supercritical Pressures

By

Jordi Poblador Ibanez

Master of Science in Mechanical and Aerospace Engineering

University of California, Irvine, 2018

Professor William A. Sirignano, Chair

This thesis presents a numerical study of the heat and mass transfer occurring when a cool liquid is suddenly introduced to a hotter gas at supercritical pressures. Different binary mixtures of heavy hydrocarbons and light gases are considered and fluid properties are obtained using a real-gas equation of state and various high-pressure models. Liquid-gas interface dynamics and mass and thermal diffusion for different pressures are analyzed. Then, a comparison with expected growth rates of the Kelvin-Helmholtz (KH) instability is provided to learn whether a phase equilibrium is well established before hydrodynamic instabilities can become important.

Two phases may still appear at supercritical pressures because mixture critical properties differ considerably from pure species critical properties. The diffusion time scales in both phases are comparable to the KH instability transient (i.e., 20-100 μs). That is, diffusion layers of 10 μm thickness in the liquid and 30 μm in the gas are observed for the oxygen/n-decane mixture, suggesting that variations of fluid properties around the liquid-gas interface may affect breakup mechanisms. Furthermore, condensation by increasing pressure can be observed, even at supercritical pressures, while the First and Second Law of thermodynamics are obeyed.

Chapter 1

Introduction

Combustion processes are present in many engineering applications where a source of power is needed. A clear example are the engines of our transportation vehicles, such as cars or airplanes, where thermal energy is converted into work and/or kinetic energy. In all these situations, fuel is injected into a gaseous environment (e.g., combustion chamber) where an oxidizing species is present, usually oxygen, and a combustion chemical reaction can happen.

This combustion reaction occurs when both reacting species are in the gaseous phase. If fuel is injected in the liquid state, it is necessary to understand how the jet will disrupt and form droplets. These droplets will vaporize due to the thermodynamic conditions of the surrounding gas and mix with it, allowing the chemical reaction to take place. This process is usually referred as atomization or spray formation and it is essential for good mixing of the reacting species, thus affecting the performance of the combustion processes and our final application.

Another key factor involved in the efficiency of the combustion process is pressure. It is well known that higher pressures increase the chemical reaction rate and produce higher specific energy conversion. Under these circumstances, specific impulse and thrust in many

types of engines (rocket engines, gas turbines or diesel engines) are also improved [8]. Consequently, there is a trend to move towards the design of combustion chambers allowing higher operating pressures. However, increasing the pressure up to supercritical pressures modifies the thermodynamics and fluid dynamics of the injection phenomena, which should be well understood to optimize the design of high-pressure combustion chambers.

Theories for liquid jet stream breakup, atomization and spray formation processes have been proposed for low-pressure flow conditions, where the disruption mechanisms are driven mainly by capillary forces and hydrodynamic instabilities, depending on the flow properties (e.g., surface tension, velocity, etc.). However, in high-pressure regimes, where a liquid stream is injected into a supercritical pressure gaseous domain, diffusion can become the main driver of the mixing process and a well-defined separation of the liquid and gas phases cannot easily be determined [9]. In fact, liquid injected into an environment exceeding its critical properties will experience a transition into a supercritical thermodynamic state. In this process, the liquid goes through a near-critical state where liquid-like densities and gas-like diffusivities will be present, with a mist appearance. Consequently, the classical gas-liquid interface seems to disappear even before supercritical conditions are achieved. This situation generates a reduced ratio of liquid/gas density, allowing aerodynamic interactions to become more important in the breakup mechanism [3]. As surface tension and enthalpy of vaporization approach zero at supercritical pressures, these interactions become even stronger [3],[8],[10]. Therefore, turbulence will become very important in this regime, even at low jet injection velocities.

Temperature in this fluid regime can affect the full transition of the liquid to a supercritical thermodynamic state. That is, chamber temperatures below the critical temperature of the liquid jet will not heat up the liquid sufficiently; so, a liquid state may still exist depending on the pressure magnitude. However, for supercritical chamber temperatures, the liquid temperature will eventually rise above its critical value, resulting in a supercritical fluid

state under high-pressure conditions.

The flow field experiences compressibility effects, which must be calculated accounting for real effects due to the high-pressure conditions; in this situation, no ideal-behavior assumptions should be considered. Moreover, solubility becomes relevant under these high-pressure conditions. Thus, not only the mixing of vaporized fuel and surrounding gas must be accounted for, but also the gas dissolving into the liquid phase. This phenomenon will modify the fluid properties aroud the liquid-gas interface, as well as the mixture critical properties. That is, the critical properties of the mixture will differ from those of the pure liquid jet, increasing its critical pressure and modifying the flow field [3]. Therefore, two phases may still appear even at pressures above the critical pressure of the injected liquid and the assumption that the liquid simply undergoes a transition from the liquid state to the supercritical state must be reviewed.

1.1 Literature review

This literature review is structured as follows: first, an analysis of traditional breakup mechanisms for subcritical pressure injection of liquid jets is presented, with the objective to understand the main concepts involved in the problem (jet stability, disruption structures formation, etc.). Useful information is found in [2], [11] and [12], where higher pressure conditions are present through a varying Weber number and gas-to-liquid density ratio. No real-gas effects nor species mixing are considered in these works though.

Thereafter, the transition from subcritical to supercritical pressure injection is addressed. To visually identify the main differences explained before, Mayer et al. [3] presents some experimental results comparing the behavior of the injection of a liquid jet into subcritical and supercritical pressures. Then, the jet injection into supercritical pressures is discussed thoroughly. The problem of modeling the supercritical vaporization, mixing and liquid jet injection is addressed in [10] and [13]. As it can be inferred from the references, supercritical jet injection involves turbulent mixing, since inertia forces become more dominant than in subcritical jet injection. Therefore, correspondent turbulence models should be developed to face this problem if it is desired to avoid dealing with the high computational costs of Direct Numerical Simulation (DNS). Turbulent mixing models for supercritical jet injection based on Large Eddy Simulation (LES) are developed in [14], [15], [16] and [17] to be applied to a study of gas jet injection into a high-pressure gaseous environment [5]. Also [18], [19], [20] and [21] propose some methodes related to LES application and selective mesh refinement. Due to the high-pressure conditions, we do not expect the liquid jet injection problem to behave much differently, as confirmed in [3]. Further studies that consider a liquid jet at the desired conditions are based on a Reynolds-Averaged Navier Stokes (RANS) turbulence model [8].

On the other hand, it is also important to study the interface dynamics between the

liquid and the gas phase under these high-pressure conditions. Some studies have focused on analyzing the pressure and temperature effects on the thickness of the liquid-gas interface, therefore trying to define the transition point between a well-defined liquid-gas interface and the typical single-phase transition behavior of the high-pressure liquid-gas interface [6],[9],[22]. Finally, some other works identify the main concerns to take into account to deal with high-pressure fluid behavior and the interface between the liquid and the gas phases [23],[24],[25],[26].

1.1.1 Subcritical liquid jet injection

Before proceeding to supercritical liquid jet injection, it is interesting to develop a brief overview of the same problem but at subcritical pressures. This will allow us to identify the main driving mechanisms of liquid breakup and how they are modified as the pressure regime changes.

The liquid breakup process can be divided into three subdomains according to the fluid mechanical behavior [11]. Upstream, the injector supplies the fluid into the combustion chamber and the liquid flow through the orifice can be affected by turbulence, cavitation and other phenomena occurring downstream. The second subdomain is between the orifice and the point where the disintegration process of the stream begins. In this region, the liquid is distorted typically in a wavelike motion of the surface. Finally, the third subdomain is from the early stages of the disintegration process to the final droplets array or spray formation. Many studies have been done for the liquid stream distortion and some computations have been performed for the disintegration cascade process [2],[12].

There are four main forces to be considered acting on the liquid: gravity force, inertia force, surface-tension force and viscous force. From these forces, three dimensionless independent groupings can be defined, plus two other groupings that eliminate the dependence

on velocity. If periodic disturbances are introduced, it may become useful to also include the Strouhal number in the analysis (see Table 1.1 and Table 1.2).

Table 1.1: Independent groupings appearing in the liquid breakup phenomena.

Reynolds	$Re = \frac{\rho_l L V}{\mu_l}$	Froude	$Fr = \frac{V^2}{gL}$
Weber	$We = \frac{\rho_l L V^2}{\sigma}$	Strouhal	$St = \frac{\omega L}{V}$

Table 1.2: Groupings eliminating velocity dependence in the liquid breakup phenomena.

Ohnesorge	$Oh = \frac{We^{0.5}}{Re} = \frac{\mu_l}{(\rho_l \sigma L)^{0.5}}$	Bond	$Bo = \frac{\rho_l g L^2}{\sigma}$

As a powerful example, it is interesting to study the round-jet injector case, since it is one of the most used configurations in combustion problems. According to Sirignano and Mehring [1], the main breakup mechanism acting on a round jet can be inferred through the Reynolds number and the Weber number based on the liquid jet (see Figure 1.1). For low Reynolds and Weber numbers (low-speed flows), the Rayleigh mechanism or capillary instabilities are the main drivers of liquid breakup. As these numbers increase, aerodynamic effects also increase and become the main drivers of the problem. In the atomization region, breakup occurs very close to the orifice. The diameter of the droplets decreases as we move from the Rayleigh mechanism region to the atomization region.

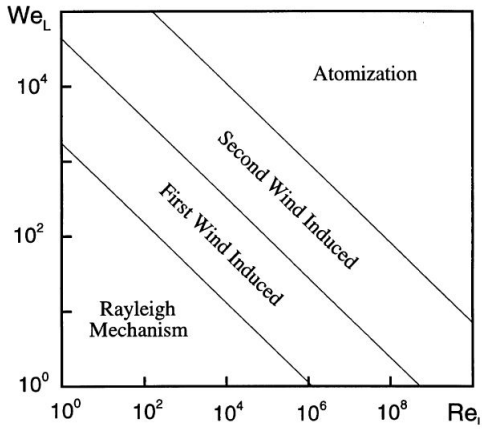

Figure 1.1: Disintegration modes as a function of the liquid Reynolds and Weber numbers (source [1]).

The capillary instability is due to the surface-tension force. Because surface tension always

acts in minimizing energy (i.e., minimize surface area for a given volume), this effect might be stabilizing or destabilizing depending on the geometry of the problem. For the round-jet problem, surface tension is destabilizing. However, for an ideally infinite liquid sheet, it would be stabilizing, since a planar sheet will always be the minimum possible surface area. This consideration is seen in Section 4.3.

For high-speed flows, aerodynamic effects become important and the so-called hydrodynamic instabilities are the main drivers of the breakup mechanism. In this regime, only at the last stages of the breakup process, capillary effects are important. These hydrodynamic instabilities are more interesting in the sense that they are the generators of different disruption structures such as lobes, holes, ligaments and bridges [2],[12]. The main hydrodynamic instabilities are the Kelvin-Helmholtz instability (KH), related to a discontinuity of the velocity component at the liquid-gas interface where a vortex sheet is formed, and the Rayleigh-Taylor instability (RT), which appears when an acceleration is present normal to the liquid-gas interface (e.g., gravity).

In a planar 2-D liquid-gas interface, it is proved that KH is always destabilizing, surface tension is always stabilizing and RT is only destabilizing if the fluid with higher density is sitting above the interface [11]. When all these effects are taken to a 3-D domain, they become the generators of non-axisymmetric instabilities which form the disruption structures that yield to the atomization or generation of droplets.

However, recent works from Jarrahbashi et al. [2],[12], showed that not only density differences through the RT instability explain the 3-D instabilities, but also vorticity dynamics around the generated disruption structures are important. In these works, fine-mesh simulations were performed for the axisymmetric behavior and fully 3-D behavior of a round jet, studying a wide range of liquid Weber and Reynolds numbers. These works take into account high gas density effects by varying the gas-to-liquid density ratio. Thus, some effects of high-pressure injection environment can be observed, but it does not exceed supercritical

pressure for the pure liquid and do not include species diffusion. What is explained in [2] and [12] is the evolution of the disruption cascade process and the role that vorticity dynamics play on it. Vorticity dynamics also explain the coherent structures that are formed and how they depend on the fluid properties through the aforesaid parameters (Re, We and gas-to-liquid density ratio) (see Figure 1.2).

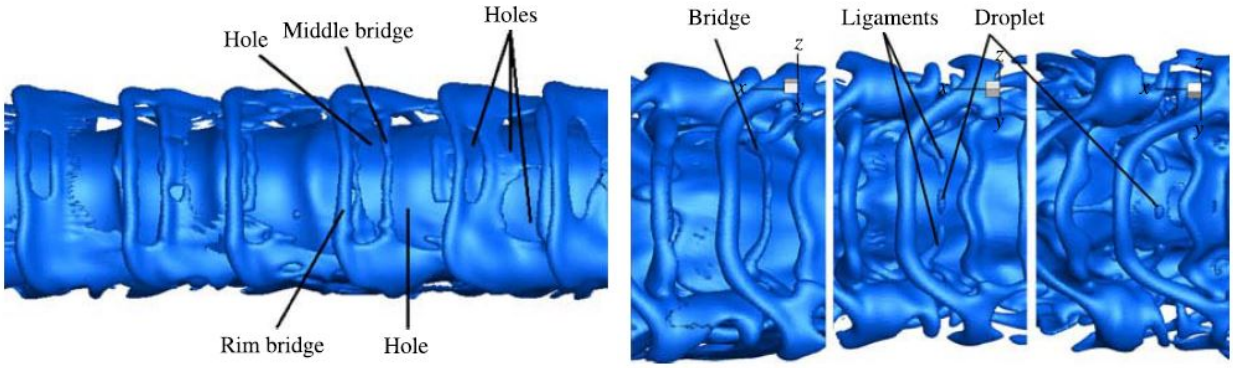

Figure 1.2: Re = 1,600 and We = 230,000 and gas-to-liquid density ratio 0.5 at different times (source [2]).

Interesting here is to address the problem of increasing the gas-to-liquid density ratio (i.e., going to higher pressures) to understand how the cascade of disruption structures is formed under these circumstances. Jarrahbashi et al. [2] provide some results that show how the lobe formation is slowed down as the gas density is increased, due to the increased inertia of the surrounding fluid. Therefore, this delays the disruption cascade occurrence in favor of the early formation of droplets and an increased growth rate of the two-phase mixture volume. This is, the vorticity structures concentrate more around the rim of the lobes, increasing the radially outward velocity allowing a larger liquid detachment from the main jet core to happen (i.e., radial development of the spray is enhanced). This effect is also qualitatively explained in [7]. Moreover, the effects of moving to a more aerodynamic-affected region are shown in Figure 1.3, where a more easily distorted jet is observed as Reynolds number increases.

Similar studies but for a 3-D planar liquid sheet are shown in Zandian et al. [4]. Again,

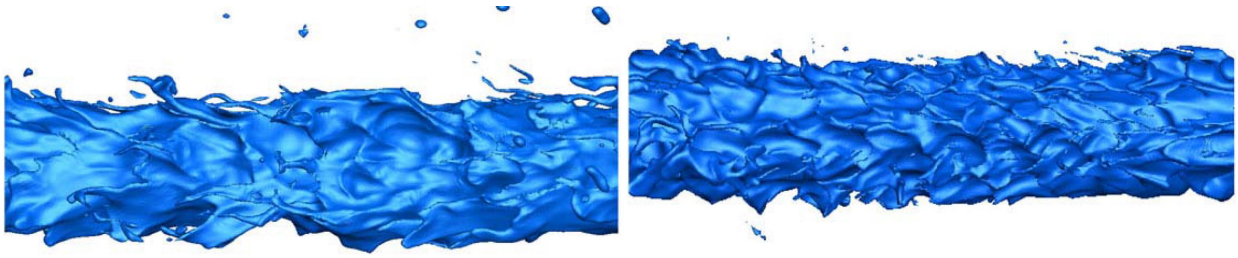

Figure 1.3: Effect of increasing Re number (from 320 on the left to 1,600 on the right) for a fixed We number (230,000) (source [2]).

this work does not include any species diffusion or real-gas effects.

1.1.2 Transition from subcritical to supercritical state

The understanding of liquid breakup at low pressures has been widely studied over the last decades. However, practical combustion chambers operate at high pressures, even well above the critical conditions of the injected liquid fuel. In this scenario, the classical breakup mechanisms must be reviewed since the liquid will experience a transition to a supercritical state and the liquid-gas interface will not be so easily identified. Furthermore, species diffusion will be present, modifying the fluid properties.

Visual aid is helpful to understand how breakup phenomena drastically change. Mayer et al. [3] performed some experiments involving injection of cryogenic propellants into a combustion chamber under high-pressure both in subcritical and supercritical conditions. With the use of flashlight photography and high-speed cinematography, they could capture the liquid breakup and atomization at different conditions. Because they provide cold-flow studies, the visual distortions due to chemical reactions (i.e., combustion) do not appear. More studies by the team of Chehroudi and Talley show similar results [27],[28],[29]. After that, both researchers have focused in the effects of acoustic disturbances on the liquid breakup at sub-, near- and supercritical conditions [30], as they are likely to be present in combustion chambers.

The cold-jet studies were divided into two types: full-scale studies, simulating same injector sizes and flow rates as in real applications, and subscale studies, using smaller elements and flows. The pressure is kept constant for each case study independently of the injected mass flow and covering a wide range of injection conditions and injector geometries. In all cases, temperature of the liquid and gas phase and injection velocity are also kept constant.

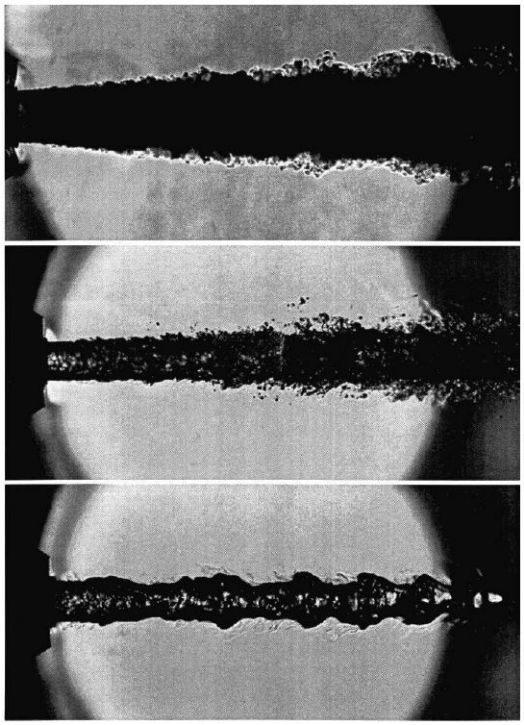

Figure 1.4: Liquid nitrogen injection into gaseous nitrogen at 4 MPa (top), 3 MPa (center) and 2 MPa (bottom) (source [3]).

Figure 1.4 shows the injection of LN_2 into GN_2 at different pressures. In all cases, the liquid nitrogen is injected at 105 K and the surronding gaseous nitrogen has a temperature of 300 K. That is, the nitrogen is injected at a subcritical temperature while the chamber temperature is supercritical (see Appendix A for different species properties). For subcritical pressures (i.e., 2.0 MPa), clear disruption structures from classical liquid breakup theories are present, similar as in [2]. However, as the pressure is increased, the atomization mechanisms change considerably. First, it is observed that the length scales of breakup decrease as the fluid is taken to higher pressures (i.e., 3.0 MPa). In this case, ligaments and droplets

formation can still be seen, but surface tension has been reduced as the critical pressure is approached and small-scale turbulent structures more easily disturb the liquid-gas interface. When the pressure exceeds the critical pressure of nitrogen (i.e., 4.0 MPa), no clear liquid-gas interface can be appreciated anymore and the problem is fully dominated by turbulent mixing, behaving as a single gas-like phase. In all three cases, the liquid nitrogen is heated up by the hotter gas and may reach supercritical temperatures at the liquid-gas interface. Nevertheless, we must be careful when explaining the physical processes that cause these observations.

Even though the results shown in Figure 1.4 are obtained by just increasing the chamber pressure maintaining constant all other parameters, it could be possible that what we are observing here is not related to pressure and temperature effects, but an effect of the increase of the Weber number (recall it is the ratio of inertia forces to surface tension forces). It could also be a combination between both. Therefore, justifying the disappearance of the classical breakup mechanisms because the liquid-gas interface has disappeared after reaching supercritical conditions might be misleading. This fact is also explained in the works from Dahms and Oefelein [6], [9] and [22].

What could be happening here is that, as pressure is increased up to supercritical pressures, the density of the gas increases and the surface tension decreases. The trend of these properties makes the Weber number increase, so the inertia forces become much more important than the surface tension. As seen in recent works from Jarrahbashi et al. [2] and Zandian et al. [4], the Weber number defined from the gas properties is one of the main parameters affecting the breakup mechanisms. As this number increases, the hole formation (perforation of the liquid stream) rate increases, together with the expansion rate of the jet. The higher expansion rate of the holes implies the formation of thinner bridges and ligaments, which break up under capillary instabilities into smaller droplets. Additionally, the characteristic time of this process is reduced, meaning that the first droplet breaking up

from the liquid jet appears sooner. The evolution of the ligaments and droplets formation and size with the Weber number is seen in Figure 1.5.

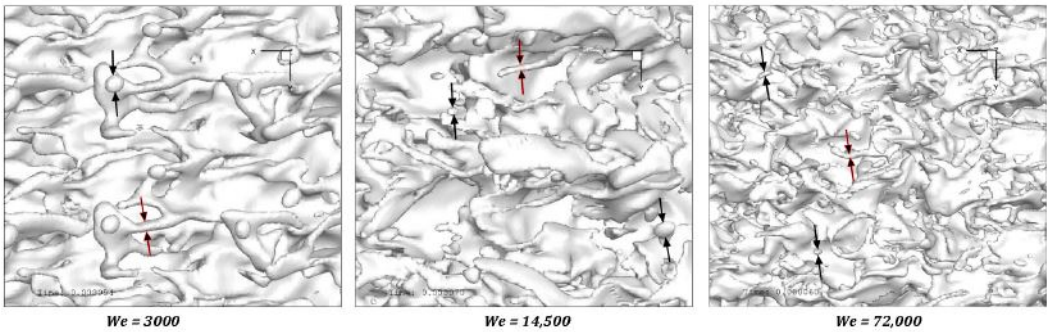

Figure 1.5: View of the liquid iso-surface for a planar liquid sheet varying We with all other parameters fixed (source [4]).

The Weber number effects could also correspond to the evolution seen in Figure 1.4, since small ligaments and droplets could not be easily seen and an expansion of the liquid jet is observed. Therefore, it is not clear what is really happening in these experimental results. Since we do not have information of the characteristic time of each possible physical process (heating up of the liquid jet up to a supercritical gas-like state or the Weber number effect on the breakup of the liquid jet into small droplets), we cannot conclude with precision what are the causes of what we are observing. Furthermore, [3] shows the effects of mixing between species due to diffusion. Figure 1.6 shows the injection of liquid nitrogen at 83 K into gaseous helium at 292 K and 5.5 MPa (supercritical conditions for nitrogen). In this configuration, the liquid-gas interface appears and disappears as the local mixture concentrations vary.

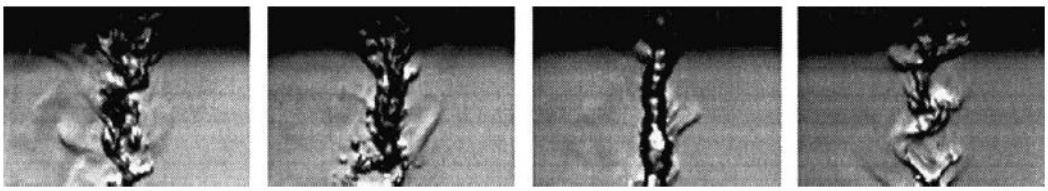

Figure 1.6: Image sequence at a fixed position of liquid nitrogen injected into helium at 5.5 MPa (source [3]).

In summary, a combination of different phenomena modifies the atomization process: the reduction of the surface tension and increase in the gas density allows aerodynamic forces to

play a more significant role and the transition from a subcritical to a supercritical state of the injected liquid is translated into the eventual disappearance of the liquid-gas interface, showing a gas-like behavior. Furthermore, this problem becomes more complex when several species are present. Local variations of pressure, temperature and mixture concentrations will be able to restore the liquid-gas interface. This phenomenon shows that the dissolution of gaseous species into a pure liquid species will create a mixture whose critical properties are modified with respect to the pure liquid itself. Precisely, its critical pressure increases, delaying the transition of the injected liquid to a supercritical fluid behavior. Thus, modeling the liquid-gas interface behavior close to the transcritical region of the fluid mixture becomes the real challenge. Some works by Dahms and Oefelein address this issue and are discussed in the following section [6],[9],[22],[31].

1.1.3 Supercritical liquid jet injection

This section focuses on the topic of this thesis. Here, some works dealing with supercritical jet injection considering real-gas effects and species mixing are presented.

In 2000, Yang [10] presented an overview of theoretical modeling and numerical simulation of supercritical behavior of the following topics: droplet gasification and combustion, spray field dynamics and multi-phase mixing and combustion processes, where the flame behavior is seen to be different depending on the fluid state (subcritical or supercritical). In Yang's work, the effects of thermodynamic non-idealities for supercritical behavior are emphasized, together with transport properties variations and the effects of high-pressure in the vapor-liquid equilibrium problem. These thermodynamic behavior changes modify the vaporization of the liquid. It is suggested to use an appropriate equation of state (EoS) to compute the thermodynamic properties (e.g., density, enthalpy, entropy and fugacity coefficients) and the phase equilibrium accounting for real-gas effects. Typical used EoS are of the cubic form,

but other more complex and accurate EoS also exist (e.g., Benedict-Webb-Rubin, BWR EoS [32],[33]). A more detailed review about cubic EoS is presented in Section 2.3.1.

Another important conclusion of this work is the influence of phase equilibrium in the shape and evolution of the liquid-gas interface before the critical conditions are achieved. One immediate result is that critical temperature of the mixture decreases as pressure is increased. This fact shows again the complexity of dealing with mixtures, since the definition of the liquid-gas interface will not only depend on the ambient pressure and temperature, but also on the changing mixture composition due to enhanced mass diffusion.

Similarly, Bellan presented the same year a critical review of investigations regarding subcritical and supercritical fluid behavior up to the date of her work [13]. One of the main things discussed in there is the computation of fluid properties. Clearly, the use of a real-gas EoS is needed (as explained in [10]), either by using a cubic EoS or any other approximation. For instance, some earlier models [34] tried to mix simpler EoS with some elaborated models for computing transport properties and solubilities at high pressures. This approximation is wrong since the fluid behavior computed through a simple EoS may not be in accordance with that of the elaborated model. Transport properties models (e.g., for computing thermal conductivity) must ensure that the low-pressure solution based on kinetic theory is recovered in the limit of low pressures. Furthermore, mass diffusivity becomes important and plays a dominant role in determining the supercritical behavior of the fluid. It is proved that mass diffusivity must be null at the critical point, thus the calculation of the mass diffusion coefficients must be done properly. For instance, Oefelein and Yang [35] used a weighted interpolation method between the gas and liquid regimes to determine the mass diffusion coefficients, but without guaranteeing a null value at the critical point. Another important phenomenon usually neglected in species formulation of the governing equations is the inclusion of the Soret and Dufour effects, which explain the mass flux due to temperature (e.g., energy) gradients and the energy flux due to mass concentration gradients,

respectively. However, Bellan suggests the inclusion of these terms if a better representation of the fluid behavior is desired, since it is not always clear if these effects can be neglected.

Another important conclusion discussed in [13] is the need of defining turbulence models. Supercritical liquid injection is seen to be dominated by aerodynamic forces in a turbulent mixing phenomena. Therefore, the definition of turbulence models to reduce the computational costs of simulating this problem is needed. This fact is more related to recent works of Bellan's research group in JPL, which have tried to develop LES models specialized for the injection phenomena from self-obtained DNS results [14],[15],[16],[17]. With this numerical progress, in 2017 Gnanaskandan and Bellan [5] have developed reliable DNS and LES numerical simulations of the round-jet injection problem into high-pressure conditions considering species mixing. The main objective is to test and validate the developed DNS and LES model. However, this work has only been done for gas jet injection, but the mechanics of the problem can be qualitatively extrapolated to the supercritical liquid injection case.

In [5], real-gas effects are considered through the Peng-Robinson equation of state (PR-EoS). Since PR-EoS is inaccurate when dealing with non-hydrocarbons species, a correction is introudced using the volum shift factor to enhance its accuracy. Soret and Dufour effects are also considered and all transport properties (viscosity, thermal conductivity, thermal diffusion coefficients and mass diffusion coefficients) are computed using multi-component mixing rules developed by Harstad and Bellan [36], valid for high pressures. The binary mass diffusion coefficients used in that work are also obtained from gas-valid correlations also developed by Harstad and Bellan [37]. With all these considerations, the governing equations, which include continuity, momentum, species continuity and total energy, together with the EoS, are solved using DNS and LES techniques. Some results of this work are shown in Figure 1.7.

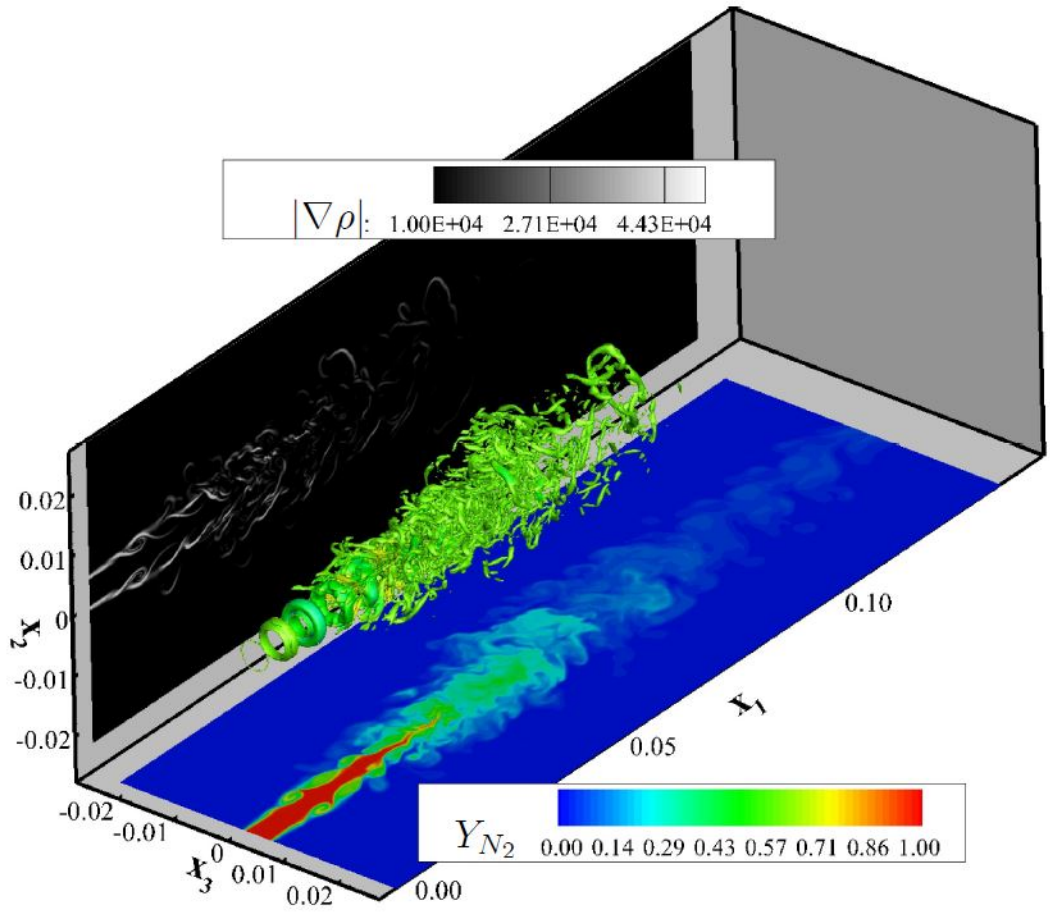

Figure 1.7: Results for nitrogen injected into carbon dioxide showing isocontours of different properties (source [5]).

Other works related to the numerical treatment of the problem are those of Huo and Yang [21], where another LES method is presented for supercritical combustion of a hydrogen gas jet being injected into gaseous oxygen. In Chen et al. [18] and Chen and Yang [19] some mesh-refinement techniques for multi-phase flow simulations are also presented to be able to capture the small scales of the problem. However, the most interesting work is that of Mak et al. [20], where an emulation technique is proposed based on a data bank from LES simulations that may help to reduce considerably the computational costs of future simulations in design problems.

Researchers such as Sierra-Pallares et al. [8] propose the introduction of RANS methods to solve the supercritical jet injection problem, so the computational costs of DNS or LES

do not appear. However, this kind of approach will not be able to capture the small scales and structures formed during the liquid atomization process and much work is still needed to be done to improve its performance.

The last works to comment in this section are those from Dahms and Oefelein ([6], [9], [22] and [31]) and Professor Ghoniem's research group from MIT ([23], [24], [25] and [26]).

In [22], the dynamics of the liquid-gas interface for high-pressure liquid injection is studied. The model uses non-equilibrium mean-field thermodynamics to show that the classical interpretation of the disappearance of the liquid-gas interface due to simply the vanishing of surface tension must be reviewed. It is suggested that the disappearance of the interface and the development of the dense-fluid mixing layer is initiated because the interface experiences a transition from molecular dynamics to a continuum regime. This is, the interface becomes much wider than the free molecular path. In this scenario, surface tension approaches zero value.

This fact contradicts the traditional theory that the interface disappears due to the heating up of the liquid to a supercritical state. This is further corroborated by experimental data [31] showing ligaments and droplets in liquid injection into supercritical pressures but at subcritical temperatures. The intention of [9] is to describe different regimes of liquid injection at high pressures and different mixture and flow conditions using the information provided by [6] and [22]. A dependence on the reduced temperature for the thickness of the interface is shown, proving that multi-phase interface structures vary for different mixture and flow conditions.

For high enough temperatures, a continuum length scale can be achieved and the interface behaves as a single-phase mixture. In this regime, it is stated that phase equilibrium assumptions and two-phase theory do not apply anymore. Especially important is the fact that the temperatures are not equal on each side of the interface. If temperature is still

low, two phases can still be identified and liquid breakup mechanisms are observed, even at supercritical pressures. To determine when this change in behavior occurs, the Knudsen-number criterion is used ($Kn = \lambda/l$), where λ is the mean free pathway of the molecules and l is the interface thickness. If $Kn < 0.1$, it is considered that we have entered a continuum region (see Figure 1.8).

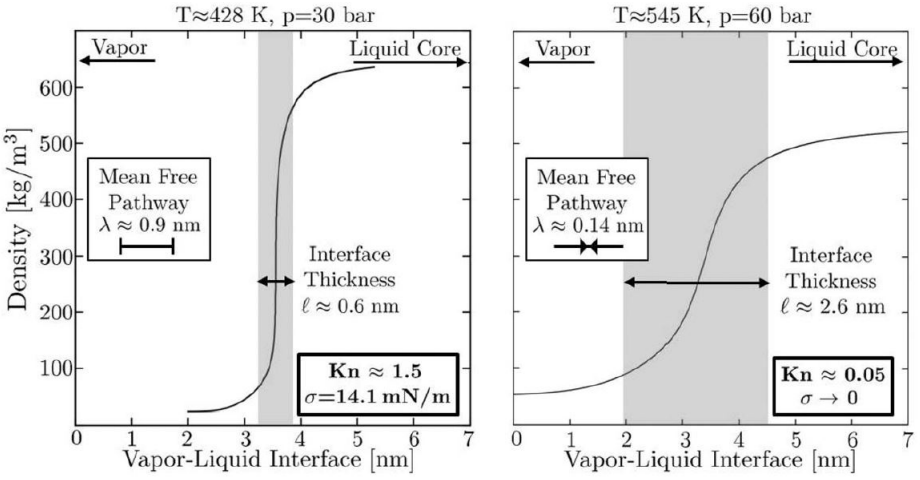

Figure 1.8: Interfacial density profiles and thicknesses for the low-temperature (left) and high-temperature (right) interface states of the n-dodecane/nitrogen mixture (source [6]).

It is important to state that this criterion yields into the predicted range of temperatures under classical phase equilibrium conditions. This is why, for temperatures close to the predicted critical point of the mixture, phase equilibrium predictions may be wrong according to Dahms and Oefelein. These results are important when modeling the interface behavior in the transcritical region of our fluid mixture.

However, this continuum length is reported to be less than 10 nm. In practical situations, the interface could be still treated as a discontinuity between the liquid and the gas phase even in this high-temperature regime. This is similar to the discontinuity associated to a shock wave, where in reality we are dealing with a continuous transition with large gradients if we look into the small scale. Furthermore, the effects showed in these works if the interface is treated as a continuum, such as the non-equality of temperatures on each side of the interface, are expected to be dissipated fast enough so we can still consider equal temperatures

when imposing equilibrium conditions at the interface. Nevertheless, the results reported by Dahms and Oefelein should be kept in mind for further works if we deal with high interface temperatures.

Finally, works by Ghoniem's research group in MIT have focused in the considerations to be taken into account when dealing with high-pressure multi-phase and multi-component flow. Especially interesting are He et al. [24] where the effects of non-ideal diffusion are analyzed and compared with ideal diffusion laws to find that the non-ideal model may predict slower diffusion processes due to the appearance of a diffusion barrier that the ideal model may not capture. Furthermore, in He and Ghoniem [23], a numerical model is presented to deal with the presence of a liquid-gas interface in our domain accounting for multi-component mass transfer. This last work becomes very interesting since it is related to the topic of this thesis.

1.2 Objectives

The literature review from the previous pages has shown us that supercritical liquid injection becomes a different problem than subcritical liquid injection. Therefore, it must be understood properly in order to improve the efficiency of future engineering applications.

It has been seen that at supercritical pressures, two phases may still exist under certain conditions. Therefore, experimental observations of supercritical liquid injection cannot be explained only as a fluid transition from liquid state to a supercritical state. Species mixing due to mass diffusion becomes an important phenomenon which changes the fluid properties across our domain, thus modifying the way the breakup of the liquid occurs. Furthermore, fluid conditions cannot be considered ideal and appropriate equations of state and models have to be used to compute fluid properties at high-pressure or high-density domains. Finally, turbulence plays an important role under these conditions and different numerical techniques may have to be considered to solve more efficiently the governing equations.

However, many of the recent simulations have only dealt with the gas jet injection problem at supercritical pressures and few studies have been done to account for a liquid jet. Therefore, the future interest lies in creating a powerful tool to solve the problem of liquid injection into high-pressure chambers.

With all this information, it is possible to create a clear list of objectives to achieve with this thesis:

- Develop a methodology to reproduce high-pressure or supercritical-pressure fluid behavior. That is, define which equation of state and which set of models are going to be used to compute real-fluid behavior. Also, define the equations to be solved and how the liquid-gas interface, if existing, has to be treated.
- Show where two phases can still exist at supercritical pressures. Using the selected

methodology, show that phase equilibrium conditions enhance mass diffusion at supercritical pressures modifying considerably the critical properties of the liquid mixture with respect to the pure liquid. Specifically, is the critical pressure of the liquid phase higher than the chamber pressure?

- Obtain characteristic times of the diffusive process. How fast does it occur? Does it modify considerably the fluid properties around the liquid-gas interface? What implications does it have?

- Compare the diffusion time scale to that of the breakup mechanism, especially of the hydrodynamic instabilities. That is, will these time scales be of the same order? Or is one process faster than the other? It could be estimated if the liquid breakup will occur before the existing mass diffusion has affected the fluid properties enough.

Chapter 2

Problem Statement and Governing Equations

2.1 Definition of the problem

The studied problem consists in analyzing the liquid-gas interface behavior of a liquid suddenly introduced into a high-pressure gaseous environment. The pure liquid species can be called "species B" and the pure gas species is called "species A". The pressure is going to be supercritical for the pure liquid species being injected. Close to the interface, a binary mixture of species A and B exists due to equilibrium conditions at the interface and the corresponding species diffusion. Studying this diffusion layer around the interface is of special interest.

The domain is set as seen in Figure 2.1, where the liquid is sitting on the left side of the interface and the gas falls on the right side. At $x = \infty^+$, only pure gas species A exist, while at $x = \infty^-$ only pure liquid species B is present. Temperature will be higher on the gas side than on the liquid side, but always remaining under the critical temperature of

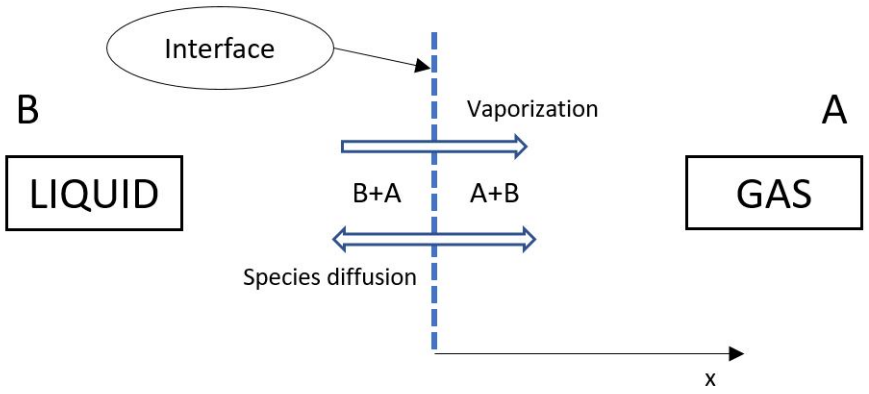

Figure 2.1: Sketch of the interface problem.

the pure liquid. In this situation, we expect to still have a compressed liquid phase for the pure liquid species. This difference in temperature will drive the vaporization of the liquid mixture across the interface.

Moreover, the interface will move in time. Therefore, it becomes critical to decide which frame of reference will be used. For simplicity, and under the assumption that momentum variations due to velocity are small compared to the constant high pressure throughout the domain, it is possible to work with a frame of reference fixed at the interface. In this case, it behaves as if $U = 0$, with U being the interface velocity. Physically, we will expect the liquid to flow into the interface, while gas will be flowing out of it, as the vaporization phenomenon occurs (if there is, indeed, vaporization). Otherwise, under certain conditions we could have a condensation where gas would be flowing into the interface and liquid would be flowing out.

2.2 Governing equations

The problem is mainly driven by diffusion forces, which relate to slow motion of the particles through the domain. Therefore, we expect small changes to occur as time marches. It can also

be assumed that fluid velocity will be small, so the momentum flux is going to be negligible compared to pressure. This fact, together with the assumption of constant pressure in the whole domain, makes it unnecessary to solve for the momentum equation. In this case, only the continuity equation, the species continuity equations and the energy equation become relevant. Their formulations for 1-D Cartesian coordinates are shown in the following lines.

The global continuity must be applied in both the gas and the liquid domains. For the gas phase, the differential form of the continuity equation becomes

$$\frac{\partial \rho_g}{\partial t} + \frac{\partial}{\partial x}(\rho_g u_g) = 0 \tag{2.1}$$

and for the liquid phase

$$\frac{\partial \rho_l}{\partial t} + \frac{\partial}{\partial x}(\rho_l u_l) = 0 \tag{2.2}$$

Furthermore, species continuity must also be satisfied. Chemical reaction is not considered in this development. The conservative form of the species continuity equation is

$$\frac{\partial}{\partial t}(\rho Y_i) + \frac{\partial}{\partial x}(\rho u Y_i) + \frac{\partial}{\partial x}(J_i) = 0 \tag{2.3}$$

After combining with Eq. 2.1 and Eq. 2.2, we obtain the non-conservative form of the equation for both phases and each species,

$$\rho_g \frac{\partial Y_{gi}}{\partial t} + \rho_g u_g \frac{\partial Y_{gi}}{\partial x} + \frac{\partial}{\partial x}(J_{gi}) = 0 \tag{2.4}$$

and

$$\rho_l \frac{\partial Y_{li}}{\partial t} + \rho_l u_l \frac{\partial Y_{li}}{\partial x} + \frac{\partial}{\partial x}(J_{li}) = 0 \tag{2.5}$$

where J_{gi} and J_{li} represent the diffusion mass flux of each species i in each phase. These mass fluxes are computed using the generalized Maxwell-Stefan equations (Eq. 2.50), which provide an effective procedure to include non-idealities in the diffusion process [23],[24].

Using the fact that $\sum_{i=1}^{N} Y_i = 1$, Eq. 2.1 is related to Eq. 2.4 and Eq. 2.2 to Eq. 2.5. Thus, from the $N+1$ equations we have, only N equations are needed to be solved.

The momentum equation, although it is not used in this work as stated before, would present the following non-conservative form, where gravity terms have been neglected and no specific form for the deviatoric stress tensor, $\bar{\bar{\tau}}$, is given as

$$\rho \frac{\partial u}{\partial t} + \rho u \frac{\partial u}{\partial x} = -\frac{\partial p}{\partial x} + \frac{\partial \tau_{xx}}{\partial x} \tag{2.6}$$

applicable to both phases, liquid and gas.

Under Newtonian fluid assumptions [38], the deviatoric stress tensor becomes

$$\bar{\bar{\tau}} = 2\mu\bar{\bar{\epsilon}} + \lambda(\nabla \cdot \bar{u})\bar{\bar{I}} = \mu(\nabla\bar{u} + (\nabla\bar{u})^T) + \lambda(\nabla \cdot \bar{u})\bar{\bar{I}} \tag{2.7}$$

For the 1-D case, it becomes $\frac{\partial \tau_{xx}}{\partial x} = (2\mu + \lambda)\frac{\partial^2 u}{\partial x^2}$. Assuming Stokes' hypothesis, where $\lambda \approx -\frac{2}{3}\mu$, the stress component becomes $\frac{\partial \tau_{xx}}{\partial x} = \frac{4}{3}\mu\frac{\partial^2 u}{\partial x^2}$.

Finally, an equation for energy is also needed. Recall it has been derived under assumptions of low-speed flow, where the viscous dissipation terms and the total derivative with respect to time of pressure have been neglected. Considering energy transport due to mass

diffusion and combining it with global continuity (Eq. 2.1 and Eq. 2.2) and species continuity (Eq. 2.4 and Eq. 2.5), we get, for the gas phase,

$$\rho_g \frac{\partial h_g}{\partial t} + \rho_g u_g \frac{\partial h_g}{\partial x} - \rho_g \sum_{i=1}^{N} h_{gi} \frac{\partial Y_{gi}}{\partial t} - \rho_g u_g \sum_{i=1}^{N} h_{gi} \frac{\partial Y_{gi}}{\partial x} - \frac{\partial}{\partial x}\left(\lambda_g \frac{\partial T}{\partial x}\right) + \sum_{i=1}^{N} J_{gi} \frac{\partial h_{gi}}{\partial x} = 0 \quad (2.8)$$

and, for the liquid phase,

$$\rho_l \frac{\partial h_l}{\partial t} + \rho_l u_l \frac{\partial h_l}{\partial x} - \rho_l \sum_{i=1}^{N} h_{li} \frac{\partial Y_{li}}{\partial t} - \rho_l u_l \sum_{i=1}^{N} h_{li} \frac{\partial Y_{li}}{\partial x} - \frac{\partial}{\partial x}\left(\lambda_l \frac{\partial T}{\partial x}\right) + \sum_{i=1}^{N} J_{li} \frac{\partial h_{li}}{\partial x} = 0 \quad (2.9)$$

Refer to Appendix C for the full development of the two previous expressions.

The previous equations require some fluid properties which need to be computed using a correspondent model or an equation of state. The discussion of how these parameters are obtained is shown in Section 2.3.

2.3 Thermodynamic relations

This section presents the necessary thermodynamic relations to compute the fluid properties of interest: density, enthalpy, fugacity, enthalpy of vaporization, entropy, diffusion mass flux, viscosity, thermal conductivity and surface tension.

2.3.1 The equation of state

The equations in Section 2.2 require the evaluation of some properties in order to be solved. Density ρ, enthalpy h, partial molar enthalpy $\bar{h_i}$ and fugacity coefficients Φ can be evaluated using an equation of state. An EoS mainly establishes a relation between the following parameters: pressure p, molar volume v and temperature T of the fluid.

The simplest equation of state we could think of is the ideal gas EoS (Eq. 2.10). However, this approach does not include any real effects and would totally fail to predict reasonable results in the range of temperatures and pressures we are looking at. Furthermore, it cannot predict liquid state properties.

$$pv = R_u T \tag{2.10}$$

The first modification to this ideal-gas equation is the "ideal" Van der Waals equation of state (VdW-EoS) (Eq.2.11), a simpler approach to account for high-density effects, but which allows us to explain better how the real-gas considerations are included [39].

$$p = \frac{R_u T}{v - b} - \frac{a}{v^2} \tag{2.11}$$

As it can be seen, two new parameters are included: the attractive parameter a and the repulsive parameter b. The latter corresponds to the first correction that can be done to the ideal gas EoS (Eq. 2.10), which is related to the volume occupied by the molecules themselves. Since we are considering high-density fluids, the volume of the molecules may not be negligible and should be subtracted from the physical volume that the fluid is occupying ($v^* = v - b$). On the other hand, a second correction needs to be done and it is related to the existing forces between the molecules. That is, the intermolecular attraction force can't

be neglected anymore due to the high-density consideration. In this situation, the actual force that the fluid exerts to the walls of the vessel containing it (i.e., pressure) is reduced by a certain amount related to the attractive parameter of the molecules (a/v^2).

However, the VdW-EoS considers the attractive and repulsive parameters to be constant under any thermodynamic state and are only fitted to provide good predictions in the gas state. Reasonably, it is expected that other parameters, such as the temperature or the acentric factor, will modify them and provide more accuracy to all range of fluid states. Therefore, it is needed to use an equation that predicts better real-gas effects in high-density fluids.

First, Redlich and Kwong [40] introduced a modification to the VdW-EoS, call it RK-EoS (Eq. 2.12), by saying that the attractive term depended on the square root of temperature. They also introduced some modification by adding the repulsive parameter to the denominator of the attractive parameter term.

$$p = \frac{R_u T}{v - b} - \frac{a/T^{0.5}}{v(v + b)} \tag{2.12}$$

Some years later, Soave [41] modified the original RK-EoS and proposed a more general temperature-dependent term $a(T)$, SRK-EoS (Eq. 2.13).

$$p = \frac{R_u T}{v - b} - \frac{a(T)}{v(v + b)} \tag{2.13}$$

In this work, the Soave-Redlich-Kwong EoS has been chosen due to its good performance in a wide range of fluid states, including sub-critical, near-critical and super-critical regions [42],[43]. Thus, it may represent both gas and liquid phase.

The three previous EoS (Eq. 2.11, Eq. 2.12 and Eq. 2.13) belong to the family of cubic

equations of state. Rearranging the SRK-EoS into a cubic form using the molar volume as the variable to solve for, we get

$$Z^3 - Z^2 + (A - B - B^2)Z - AB = 0 \tag{2.14}$$

In the previous equation, the compressibility factor Z and the parameters A and B are given by

$$Z = \frac{pv}{R_u T} \quad ; \quad A = \frac{ap}{(R_u T)^2} \quad ; \quad B = \frac{bp}{R_u T} \tag{2.15}$$

where the terms a and b are computed according to the quadratic mixing rules of the SRK-EoS, accounting for the pure species attractive and repulsive parameters a_i and b_i, respectively, as

$$a = \sum_{i=1}^{N} \sum_{j=1}^{N} X_i X_j (a_i a_j)^{0.5} (1 - k_{ij}) \quad ; \quad b = \sum_{i=1}^{N} X_i b_i \tag{2.16}$$

where k_{ij} are the so-called binary interaction coefficients, which are derived from experimental data in order to fit the results provided by the EoS. For hydrocarbon mixtures, assuming $k_{ij} = 0$ can be a good approximation [41],[44]. Nevertheless, the inclusion of these parameters for other types of mixtures, such as mixtures containing hydrogen, can become important.

The attractive and repulsive parameters for the pure species are obtained from the critical point of each species, assuming that the first and second derivative of pressure with respect to volume must be zero. They depend on the critical temperature, T_{ci}, critical pressure, p_{ci}, and reduced temperature, $T_{ri} = T/T_{ci}$. In this case, it is obtained that

$$a_i = 0.42748 \frac{(R_u T_{ci})^2}{p_{ci}} \alpha_i \quad ; \quad b_i = 0.08664 \frac{R_u T_{ci}}{p_{ci}} \tag{2.17}$$

where α_i is defined as

$$\alpha_i = [1 + S_i(1 - T_{ri}^{0.5})]^2 \tag{2.18}$$

being S_i a parameter depending on the acentric factors of each species, ω_i, originally defined by Soave as

$$S_i = 0.480 + 1.574\omega_i - 0.176\omega_i^2 \tag{2.19}$$

If we solve for the molar volume v, then it is possible to obtain the density of the mixture as $\rho = MW_{mix}/v$. The equation is applicable for each phase, gas or liquid.

A simplification that can be taken into account for this EoS comes from assuming a case where A and B are much smaller than 1 ($A << 1$ and $B << 1$). That is, the gas phase is close to ideal gas behavior. In this situation, if Eq. 2.14 is rearranged as

$$Z - 1 = \frac{B}{Z - B} - \frac{A}{Z + B} \tag{2.20}$$

it can be simplified using Taylor series expansion to find that

$$Z \approx 1 + B - A \tag{2.21}$$

where the compressibility factor becomes of order 1 ($Z \simeq 1$).

In gaseous regions where these assumptions are satisfied, it may become computationally more efficient to solve the EoS by using Eq. 2.21.

Improvements to the SRK-EoS

The SRK-EoS, as said before, is a well-balanced equation of state that can be implemented in problems that require of the evaluation of real-gas properties. It presents a good performance in the range of pressures and temperatures of interest. Furthermore, the fact that we are dealing with a cubic equation makes it easier and more efficient to be solved, since analytical solutions for cubic equations exist [45] or an iterative solver can be easily implemented.

However, this model may present some disadvantages. It usually predicts lower densities for the liquid phase and it may be strongly dependent on the binary interaction coefficients k_{ij} when working with mixtures to predict phase equilibrium compositions. Therefore, the representation of the critical point of the mixture may not be always accurate. Some results comparing the performance of this EoS with the reference program REFPROP from the National Institute of Standards and Technology (NIST) are shown in Appendix E.

Correcting the mismatch in liquid densities is left for further studies related to this work. At this point, testing the performance of the SRK-EoS in this issue could become tedious, since it will depend on the species being considered. Some works suggest that the Peng-Robinson equation of state (PR-EoS, [46]), also of cubic form but more complex than SRK-EoS, presents better performance in this issue [5],[14],[15],[23],[24],[47].

On the other hand, the influence of the interaction coefficients can be improved if enough information is known about them. The following lines address this subject with the objective to be able to implement values for k_{ij}. If these coefficients are unknown for any mixture we deal with, they are set to be equal to zero.

Graboski and Daubert introduced some modifications to the SRK-EoS for systems containing only hydrocarbons [44], systems containing CO_2, H_2S , N_2 and CO [48] and systems containing H_2 [49].

The hypothesis taken by Soave assuming that binary interaction coefficients are not relevant for hydrocarbon mixtures is confirmed in [44], but a modification to the S_i term is introduced for this type of mixtures based on an extended data bank. It is rewritten as

$$S_i = 0.48508 + 1.55171\omega_i - 0.15613\omega_i^2 \tag{2.22}$$

For systems containing hydrogen sulfide, nitrogen, carbon monoxide and carbon dioxide, interaction coefficients are introduced [48] to fit better the SRK-EoS to experimental data. In this case, the expression for S_i of Eq. 2.22 is also considered.

Finally, a modification to the α function of the SRK-EoS is presented for systems containing hydrogen [49]. Due to the extremely supercritical state of hydrogen, Eq. 2.18 cannot predict properly its behavior and the need of specific interaction coefficients for each hydrogen-containing mixture becomes critical to obtain good calculations using the original SRK-EoS. Assuming $k_{ij} = 0$, a new expression for α is found for hydrogen, as a function of its reduced temperature $T_{r,H_2} = T/T_{c,H_2}$, which can better reproduce experimental data without the need of interaction coefficients It is given by

$$\alpha_{H_2} = 1.202e^{-0.30228T_{r,H_2}} \tag{2.23}$$

Furthermore, this work presents a conversion from general binary interaction coefficients obtained using an α parameter for hydrogen as in Eq. 2.18 to the binary interaction coefficients that would be obtained using the new α function found in Eq. 2.23. Although the new

function is obtained from fitting experimental results with zero-value interaction coefficients, this conversion can improve the obtained results.

Other authors proposed further modifications to the α function [50] with the objective to reduce the need of interaction coefficients. This new function, Eq. 2.24, depends on the critical properties of the species and three coefficients: L, M and N. These coefficients are determined for each species from regression of pure-component vapor pressure. It can also be applied to hydrogen-containing mixtures and presents more accurate results than those using Eq. 2.23.

$$\alpha_i = T_{ri}^{N(M-1)} e^{L(1-T_{ri}^{NM})} \tag{2.24}$$

As it can be seen, the values of k_{ij} are crucial to obtain better matching between experimental data and the results predicted by the EoS. These values can usually be held constant independently of temperature and pressure. However, for many mixtures of interest, especially those containing hydrogen, values for the interaction coefficients are usually obtained for specific pressure and temperature ranges.

Pressure dependency is usually neglected. However, it would be interesting to obtain a general temperature-dependent function to obtain values for k_{ij} to obtain more precise coefficients. Soave et al. [51] presented general correlations for specific mixture groups to find the binary interaction coefficients as a function of temperature and the mixture species.

The method obtains the k_{ij} by comparing the fugacity coefficient equation (Eq. 2.43) obtained using the classical quadratic mixing rules of the SRK-EoS model with the fugacity coefficient equation obtained using Huron-Vidal mixing rules. Without loss of generality, these equations are compared for a binary system of component 1 at infinite dilution in component 2 to obtain that

$$\left(2(1-k_{12})\sqrt{\frac{a_1}{a_2}}-\frac{b_1}{b_2}\right)\frac{a_2}{R_uTb_2}=\left(\frac{a_1}{R_uTb_1}-\frac{\ln\gamma^{\infty}_{1(2)}}{\ln 2}\right) \tag{2.25}$$

where the activity coefficient $\gamma^{\infty}_{1(2)}$ is predicted by group contributions (Eq. 2.26 and Eq. 2.27).

$$\ln\gamma_i^{\infty}=b_i\left(\sum_j^N\varphi_j\sigma_{ij}-\frac{1}{2}\sum_j^N\sum_k^N\varphi_j\varphi_k\sigma_{jk}\right) \tag{2.26}$$

$$\varphi_i=\frac{X_ib_i}{\sum_{j=1}^N X_jb_j} \tag{2.27}$$

The new interaction coefficients σ_{ij} must follow some rules, as explained in [51]. The dependence of these coefficients with temperature are shown in Eq. 2.28 and Eq. 2.29, which present the particular correlation for nitrogen/alkanes mixtures and carbon dioxide/alkanes mixtures, respectively.

$$\sigma\left(\frac{\text{bar}}{\text{K}}\right)\left[\frac{\text{N}_2}{\text{alkane}}\right]=\left(\frac{57}{T(K)}\right)^{1.4} \tag{2.28}$$

$$\sigma\left(\frac{\text{bar}}{\text{K}}\right)\left[\frac{\text{CO}_2}{\text{alkane}}\right]=\left(\frac{118}{T(K)}\right)^{1.6} \tag{2.29}$$

Once the activity coefficient is known, it is possible to obtain k_{ij} by imposing the equality in Eq. 2.25. Some values for these coefficients are shown in Table 2.1.

Table 2.1: Binary interaction coefficients for the SRK-EoS obtained with Soave et al. model.

$\mathbf{CO_2/C_3H_8}$		$\mathbf{N_2/C_{10}H_{22}}$	
T (K)	k_{ij}	T (K)	k_{ij}
250	0.13518	250	0.08329
300	0.14073	300	0.07696
350	0.14846	350	0.06978
400	0.15801	400	0.06116
450	0.16920	450	0.05039
500	0.18203	500	0.03659

2.3.2 An equation for enthalpy

As stated before, enthalpy, h, can be predicted from the EoS. In the high-pressure regimes we are working in, the enthalpy will differ from that predicted by the ideal gas law by the addition of a departure function [52], given by

$$H - H^* = R_u T(Z-1) + \int_\infty^v \left[T\left(\frac{\partial p}{\partial T}\right)\Big|_v - p \right] \mathrm{d}v \tag{2.30}$$

where H^* is the enthalpy of the mixture under ideal gas law behavior.

In terms of the compressibility factor, the departure function becomes

$$H - H^* = R_u T(Z-1) + R_u T \int_\infty^v \left[T\left(\frac{\partial Z}{\partial T}\right)\Big|_v \right] \frac{\mathrm{d}v}{v} \tag{2.31}$$

$$Z = \frac{v}{v-b} - \frac{\frac{a(T)}{R_u T} v}{v(v+b)} \tag{2.32}$$

Introducing the SRK-EoS, expressed as Z(v,T) (see Eq. 2.32), in Eq. 2.31 and rewriting it in terms of specific enthalpy, we obtain the following expression, applicable both for the gas and the liquid phase,

$$h = h^*(T) + \frac{1}{MW_{mix}}\left(R_u T(Z-1) + \frac{T(\partial a/\partial T)|_{p,X_i} - a}{b}\ln\left[\frac{Z+B}{Z}\right]\right) \tag{2.33}$$

where $h^*(T)$ states for a more general temperature-dependent function for the ideal gas specific enthalpy, computed using Passut and Danner correlations [53]. In this work, a fifth-order polynomial to describe enthalpy behavior is considered (see Appendix D). Ideal gas enthalpy for a mixture can be computed as

$$h^*(T) = \sum_{i=1}^{N} Y_i h_i^*(T) \tag{2.34}$$

with $h_i^*(T)$ being the ideal gas enthalpy for the pure species i.

The partial molar enthalpy $\bar{h_i}$ can be derived taking the partial derivative of the mixture molar enthalpy $\bar{h}$ with respect to X_i at constant p, T and $X_{j\neq i}$ as

$$\bar{h_i} = \left(\frac{\partial \bar{h}}{\partial X_i}\right)_{p,T,X_{j\neq i}} \tag{2.35}$$

which is the common shortcut taken in many works instead of applying the rigorous definition of partial molar enthalpy as

$$\bar{h_i} = \left(\frac{\partial \bar{H}}{\partial n_i}\right)_{p,T,n_{j\neq i}} \tag{2.36}$$

Two things must be noticed before proceeding. Here, we are deriving the mixture molar enthalpy, while Eq. 2.33 provides the specific enthalpy per unit of mass. Therefore, to recover the enthalpy per unit mole we need to multiply the specific enthalpy by the molecular weight of the mixture ($\bar{h} = MW_{mix}h$). Furthermore, when taking this derivative, the $R_u T$ term is,

actually, $R_u T \sum_{i=1}^{N} X_i$, as seen in [25].

Applying Eq. 2.35 and rearranging terms, we get the partial molar enthalpy to be

$$\begin{aligned}\bar{h_i} = \bar{h_i^*}(T) + p\frac{\partial v}{\partial X_i}\bigg|_{p,T,X_{j\neq i}} - R_u T + \frac{A_1}{v+b}\left[A_2 - \frac{(\partial v/\partial X_i)|_{p,T,X_{j\neq i}}}{v}\right] \\ + \ln\left[\frac{v+b}{v}\right]\left(\frac{1}{b}\right)\left[T\left(\frac{\partial^2 a}{\partial X_i \partial T}\bigg|_{p,X_{j\neq i}} - \frac{\partial a}{\partial X_i}\bigg|_{p,T,X_{j\neq i}}\right) - A_1 A_2\right]\end{aligned} \tag{2.37}$$

where the coefficients A_1 and A_2 are

$$A_1 = T(\partial a/\partial T)|_{p,X_i} - a \tag{2.38}$$

$$A_2 = \frac{(\partial b/\partial X_i)|_{p,T,X_{j\neq i}}}{b} \tag{2.39}$$

Then, to recover the partial specific enthalpy per unit mass, it is only needed to divide the partial molar enthalpy by the molecular weight of each particular species,

$$h_i = \frac{\bar{h_i}}{MW_i} \tag{2.40}$$

The previous equations require the evaluation of some partial derivatives of a, b and v terms, which are found in Appendix B.

2.3.3 An equation for fugacity

The SRK-EoS can also be used to compute the fugacity coefficients. The fugacity coefficient is defined as the ratio between fugacity and pressure, which for each species in a mixture equals, using the definition of partial pressure,

$$\Phi_i = \frac{f_i}{p_i} = \frac{f_i}{pX_i} \tag{2.41}$$

Thus, fugacity acts as a partial pressure, but related to an accurate computation of the chemical equilibrium constant instead of the classical mechanical partial pressure. For an ideal gas, fugacity for each species will tend to be equal to their corresponding partial pressure.

The general thermodynamic relation for the fugacity of a component in a mixture [41] is

$$\ln[\Phi_i] = \int_{\infty}^{v} \left[\frac{1}{v} - \frac{1}{R_u T} \left(\frac{\mathrm{d}p}{\mathrm{d}n_i} \right)_{T,p,n_j} \right] \mathrm{d}v - \ln Z \tag{2.42}$$

which can be rewritten introducing the SRK-EoS as

$$\ln[\Phi_i] = \frac{b_i}{b}(Z-1) - \ln[Z-B] - \frac{A}{B}\left[2\left(\frac{a_i}{a} \right)^{0.5} - \frac{b_i}{b} \right] \ln\left[1 + \frac{B}{Z} \right] \tag{2.43}$$

2.3.4 The enthalpy of vaporization

The enthalpy of vaporization or latent heat of vaporization represents the necessary energy that requires the liquid phase to vaporize (i.e., evolve from liquid to gas phase) and is defined as

$$\Delta H_v = H_g - H_l \tag{2.44}$$

which in general will depend on temperature, pressure and mixture composition.

As seen in Eq. 2.69 in Section 2.4, knowing the enthalpy on both sides of the interface, it is possible to compute the enthalpy of vaporization of the mixture. However, sometimes we are interested in the enthalpy of vaporization associated to a specific species. In this case, evaluating the difference in partial enthalpy could be useful, but using the Clausius-Clapeyron equation (Eq. 2.45) provides an analytic procedure to estimate the heat of vaporization [54].

$$\frac{dP_{\text{sat}}}{P_{\text{sat}}} = \frac{\Delta h_v}{R_u}\frac{dT_{\text{sat}}}{T_{\text{sat}}^2} \tag{2.45}$$

The Clausius-Clapeyron equation can be evaluated in terms of the fugacity coefficients [55],[56] to obtain an expression for the enthalpy of vaporization for each component in the mixture as

$$\Delta\bar{h}_{v,i} = \bar{h}_{g,i} - \bar{h}_{l,i} = -R_u T^2 \frac{\partial}{\partial T}\left[\ln\frac{\Phi_{g,i}}{\Phi_{l,i}}\right] = -R_u T^2\left(\frac{\partial \ln \Phi_{g,i}}{\partial T} - \frac{\partial \ln \Phi_{l,i}}{\partial T}\right) \tag{2.46}$$

provided in J/mol. Dividing by the molecular weight of each species, we can get the enthalpy

of vaporization in J/kg, as $\Delta h_{v,i} = \Delta \bar{h}_{v,i}/MW_i$. However, the quantity to be reported is the enthalpy of the mixture. Thus, the enthalpy of vaporization should be obtained using Eq. 2.44.

The partial derivatives shown in Eq. 2.46 are found in Appendix B.

2.3.5 An equation for entropy

The SRK-EoS can also be used to obtain the entropy of our mixture in a similar manner to how enthalpy is obtained (see Section 2.3.2). The entropy will differ from the ideal gas entropy by a departure function [52], given in terms of Z as

$$S - S^* = R_u \ln(Z) + R_u \int_{\infty}^{v} \left[T \left(\frac{\partial Z}{\partial T} \right) \Big|_v - 1 + Z \right] \frac{\mathrm{d}v}{v} \tag{2.47}$$

Applying the expression for the SRK-EoS of Eq. 2.32, and rewriting in terms of specific entropy, we get

$$s = s^*(T) + \frac{1}{MW_{mix}} \left(\frac{1}{b} \left(\frac{\partial a}{\partial T} \right) \Big|_{p,X_i} \ln \left(\frac{Z+B}{Z} \right) + R_u \ln(Z-B) \right) \tag{2.48}$$

where $s^*(T)$ is the ideal gas entropy computed using Passut and Danner correlations [53] (refer to Appendix D for more details).

As it is done for enthalpy, the entropy of an ideal mixture can also be computed as

$$s^*(T) = \sum_{i=1}^{N} Y_i s_i^*(T) \tag{2.49}$$

2.3.6 Diffusion mass flux

The problem we are studying includes mass diffusion due to the variation of species concentration along our domain. That is why the terms J_{gi} and J_{li} appear in our equations, which represent the mass flux due to diffusion. As stated in [23], [24] and [47], using the generalized Maxwell-Stefan equations (Eq. 2.50) to compute these fluxes allows us to introduce non-idealities to the diffusion process. In this equation, D_{ij} represent the Maxwell-Stefan binary diffusion coefficients, generally different from the Fickian diffusion coefficients, and D_i^T are the generalized thermal diffusion coefficients. The term c refers to the molar density of the mixture.

As a matter of clarification, in our governing equations we deal with mass fluxes, J or J^m, to emphasize the mass-based behavior of these fluxes. In the following development, clear distinction between mass fluxes, J^m, and molar fluxes, J^M, is necessary.

$$\sum_{j\neq i} \frac{X_i X_j}{D_{ij}} \left(\frac{J_j^M}{cX_j} - \frac{J_i^M}{cX_i} \right) = d_i - \sum_{j\neq i} \frac{X_i X_j}{D_{ij}} \left(\frac{D_j^T}{\rho Y_j} - \frac{D_i^T}{\rho Y_i} \right) \nabla \ln T \tag{2.50}$$

The thermal diffusion term in Eq. 2.50, is neglected since temperature gradients are not large in our problem. Thus, the only driving force (i.e., d_i) for the diffusion process to occur is directly related to concentration gradients.

Under ideal mixture hypothesis, the driving force for component i is directly the gradient in molar concentration of that component ($d_i = \nabla X_i$). However, our problem conditions are far from being considered ideal. Thus, non-idealities must be included using the fugacity coefficient (Eq. 2.51). Note, if the mixture is ideal, $\Phi = 1$ and we recover the expression for the driving force under ideal assumptions.

$$d_i = \nabla X_i + X_i \sum_{j=1}^{N} \left. \frac{\partial \ln \Phi_i}{\partial X_j} \right|_{p,T} \nabla X_j \tag{2.51}$$

Developing Eq. 2.51 for a 1-D Cartesian problem, we obtain

$$d_i = \frac{\partial X_i}{\partial x} + X_i \sum_{j=1}^{N} \left. \frac{\partial \ln \Phi_i}{\partial X_j} \right|_{p,T} \frac{\partial X_j}{\partial x} \tag{2.52}$$

The summation of the driving forces is zero ($\sum_i^N d_i = 0$). Therefore, the summation of the diffusion fluxes must be zero ($\sum_i^N J_i^M = 0$) in order to solve the Maxwell-Stefan equations. Knowing this, we can present a general procedure to compute the mass fluxes J_i^m.

For a binary mixture, ($N = 2$), Eq. 2.50 can be easily simplified. Introducing the thermodynamic factor term, Γ_{12}, which provides a measure of the non-ideality of the mixture, we get

$$\Gamma_{12} = 1 + X_1 \left(\left. \frac{\partial \ln \Phi_1}{\partial X_1} \right|_{p,T} - \left. \frac{\partial \ln \Phi_1}{\partial X_2} \right|_{p,T} \right) \tag{2.53}$$

$$\frac{1}{c} \frac{X_1 X_2}{D_{12}} \left(\frac{J_2^M}{X_2} - \frac{J_1^M}{X_1} \right) = \Gamma_{12} \frac{\partial X_1}{\partial x} \tag{2.54}$$

which can be further simplified by knowing that $J_2^M = -J_1^M$ under the mole-based frame of reference (that is, working with mole fraction gradients), to obtain

$$J_1^M = -c \frac{\Gamma_{12}}{\frac{1}{D_{12}}(X_1 + X_2)} \frac{\partial X_1}{\partial x} = -cD^M \frac{\partial X_1}{\partial x} \tag{2.55}$$

However, we are interested in mass diffusion fluxes relative to the mass-averaged velocity.

Using Fick's law [57], for a binary mixture,

$$J_1^m = -\rho D^m \frac{\partial Y_1}{\partial x} \tag{2.56}$$

being ρ the mixture density.

From the previous equations we obtain that the mole-based and the mass-based Fickian diffusion coefficients, D^M and D^m, are equal for a binary mixture [47].

$$D^m = D^M = \frac{\Gamma_{12} D_{12}}{X_1 + X_2} = \Gamma_{12} D_{12} \tag{2.57}$$

Solving for J_1^m in Eq. 2.56 we can then obtain $J_2^m = -J_1^m$ under the new frame of reference. For mixtures of $N > 2$ the previous equations cannot be rearranged in that simpler way and have to be worked out differently [47],[57].

As a matter of clarification, we could have solved for the mass fluxes by expressing Eq. 2.54 in terms of J_1^m and J_2^m, but in that case, we would be solving for the mass fluxes relative to the molar-averaged velocity, instead of the mass-averaged velocity using mass fraction gradients. To solve Eq. 2.53 we also need to find the binary diffusion coefficient D_{12}. Notice that $D_{ij} = D_{ji}$ holds always true, so reversing the problem and solving for J_2 would give us the same results.

Since our fluid phenomena is mainly diffusive, being able to compute the diffusion coefficients for high-pressure conditions becomes crucial and necessary. Literature in this topic is broad, but few is said about the computation of these coefficients in the desired conditions. Mainly, some models and correlations have been developed from experimental data. Their accuracy is based on the available experiments up to date, but still they provide a reasonable value for those coefficients. It is expected that as the studied topic here is further investi-

gated in the following years, more studies about how the diffusive process behaves and how to compute these coefficients will appear.

One of the most easy-to-use models to compute diffusion coefficients is that of Riazi and Whitson [58], which presents a correlation based on the pseudocritical properties of the mixture, the low-pressure diffusion coefficient and the viscosity of the mixture to obtain the diffusion coefficient under high-density or high-pressure conditions. However, the correlations used to define this model are based on a small data bank, so it may fail to predict reasonable results for mixtures other than those used in their work. Another comment about Riazi and Whitson work is that they directly compute mass-based binary Fickian diffusion coefficients.

Ghoniem et al. ([23], [24], [25] and [26]) propose to use the Tracer Liu-Silva-Macedo model [59] to compute tracer diffusion coefficients together with Wesselingh and Krishna model [60]. However, those works are relatively old and somewhat difficult to implement. In the present work, it has been chosen to implement the work done by Leahy-Dios and Firoozabadi [47], which presents a more extended data bank and is directly related to the implementation of Maxwell-Stefan equations. One of the weaknesses of this model, though, is its high dependence on the other models being used in the present work. The thermodynamic factor and density will depend on the SRK-EoS and, as it has already been explained, the SRK-EoS is not always precise when computing liquid density and its results depend on the binary interaction coefficients. Furthermore, viscosity (i.e., the viscosity model chosen) will also influence the diffusion model. Nevertheless, many of the models computing diffusion coefficients depend on some measure to the viscosity model used in their correlations. Details on the formulation of this model are provided in Appendix B and Appendix D, and comments about its performance are made in Appendix E.

2.3.7 Viscosity and thermal conductivity

The energy equations (Eq. 2.8 and Eq. 2.9) require the evaluation of the thermal conductivity, λ, of the mixture, both in the gas phase and in the liquid phase. If we need to solve the momentum equation, we would also need to compute the viscosity of the mixture, μ, again for both phases.

To compute these properties, the general correlation method proposed by Chung et al. [61] is used. It has been obtained from an extended data bank including experimental data from dense fluids (i.e., at high pressures) and provides reasonably accurate results for mixtures. Moreover, only the critical properties and the acentric factors are needed to compute viscosity and thermal conductivity if the mixture is only composed by nonpolar fluids. For polar and associating fluids, it is needed to use also the dipole moment and an association parameter. Therefore, for our mixtures of interest, the correlation presented by Chung et al. becomes simple to use.

Details on the formulation of this model are found in Appendix D.

2.3.8 Surface tension

One of the objectives of this work is to obtain estimates of some instability parameters, such as growth rate and oscillation frequency for the Kelvin-Helmholtz instability. For this, we need to compute the surface tension of the liquid mixture in contact with the gas mixture (i.e., the surface tension at the liquid-gas interface). As recommended by Poling et al. [52], the Macleod-Sugden correlation (Eq. 2.58) is used to estimate the surface tension.

$$\sigma_m = \left([P_{Lm}]\rho_{Lm} - [P_{Gm}]\rho_{Gm} \right)^n \tag{2.58}$$

In the previous equation, surface tension of the mixture, σ_m, is provided in dyn/cm or mN/m, ρ_{Lm} and ρ_{Gm} are the liquid mixture density and the gas mixture density in mol/cm^3, respectively, and $[P_{Lm}]$ and $[P_{Gm}]$ are the parachor of the liquid mixture and the parachor of the gas mixture. The exponent n is usually taken to be 4, but some sources recommend using 3.6 for some specific mixtures instead. In the present work, the more general value of $n = 4$ has been chosen.

The parachor of the mixtures are computed accordingly to,

$$[P_{Lm}] = \sum_{i}^{N} \sum_{j}^{N} X_{li} X_{lj} [P_{ij}] \tag{2.59}$$

$$[P_{Gm}] = \sum_{i}^{N} \sum_{j}^{N} X_{gi} X_{gj} [P_{ij}] \tag{2.60}$$

where X_{gi} and X_{li} are the mole fractions of component i in the gas mixture and the liquid mixture. $[P_{ij}]$ is computed as,

$$[P_{ij}] = \lambda_{ij} \frac{[P_i] + [P_j]}{2} \tag{2.61}$$

In Eq. 2.61, λ_{ij} is a binary interaction coefficient, usually set to 1 if no experimental data is available to obtain a more reliable value. $[P_i]$ is the parachor of the pure component i. A methodology to compute the values of the parachor of each pure component is shown in Appendix D.

2.4 Matching conditions

To ensure the physical consistency of the model, some matching conditions must be satisfied at the interface between the liquid and the gas phase. These conditions are related to mass and energy balances (i.e., flux coming in from one side of the interface must equal the exiting flux) and thermodynamic equilibrium requirements.

At the interface, phase equilibrium laws prevail, which means that pressure, p, temperature, T, and chemical potential of each species, μ_{ci}, must be equal on each side of the interface [52],[55]. The chemical potential equality can be rearranged in terms of fugacity, and the three equilibrium conditions become,

$$p_l = p_g \tag{2.62}$$

$$T_l = T_g \tag{2.63}$$

$$f_{li} = f_{gi} \tag{2.64}$$

In this case, there is no interface curvature and capillary pressure. Therefore, the condition from Eq. 2.62 is automatically satisfied under our hypothesis of constant pressure throughout the domain. However, this statement must be verified in the simulations. On the other hand, the condition of Eq. 2.63 will impose a relation between temperature gradients on each side of the interface. Finally, the condition in Eq. 2.64 can be rewritten using the mole fractions of each species and the fugacity coefficient (Eq. 2.65), a parameter obtainable from the selected equation of state, as it has been shown before. Recall that the fugacity coefficient,

Φ, is a function of pressure, temperature and mole fractions of all species composing the mixture (Eq. 2.43).

$$X_{li}\Phi_{li} = X_{gi}\Phi_{gi} \tag{2.65}$$

Another condition to be satisfied at the interface is a mass balance for each species, since continuity of mass flux must be guaranteed. For each species we have,

$$\rho_g Y_{gi}(u_g - U) + J_{gi} = \rho_l Y_{li}(u_l - U) + J_{li} \tag{2.66}$$

where U is the interface velocity, which becomes an eigenvalue of the problem. That is, for any interface velocity, we obtain a different, but consistent, velocity field. In the present work, it is set to zero as discussed earlier.

Summation of Eq. 2.66 over all species provides an expression for the global mass balance (Eq. 2.67).

$$\rho_g(u_g - U) = \rho_l(u_l - U) \tag{2.67}$$

Finally, energy flux across the interface must also be balanced.

$$\rho_l u_l h_l - \lambda_l \frac{\partial T}{\partial x} + \sum_{i=1}^{N} J_{li} h_{li} - \rho_l U h_l = \rho_g u_g h_g - \lambda_g \frac{\partial T}{\partial x} + \sum_{i=1}^{N} J_{gi} h_{gi} - \rho_g U h_g \tag{2.68}$$

Eq. 2.68 can be rewritten as,

$$\rho_l(u_l - U)(h_l - h_g) - \lambda_l \frac{\partial T}{\partial x} + \sum_{i=1}^{N} J_{li} h_{li} = -\lambda_g \frac{\partial T}{\partial x} + \sum_{i=1}^{N} J_{gi} h_{gi} \tag{2.69}$$

where the term $(h_l - h_g)$ provides the energy of vaporization of the liquid.

The following Figure 2.2 shows an schematic of all the balances across the interface that must be taken into account.

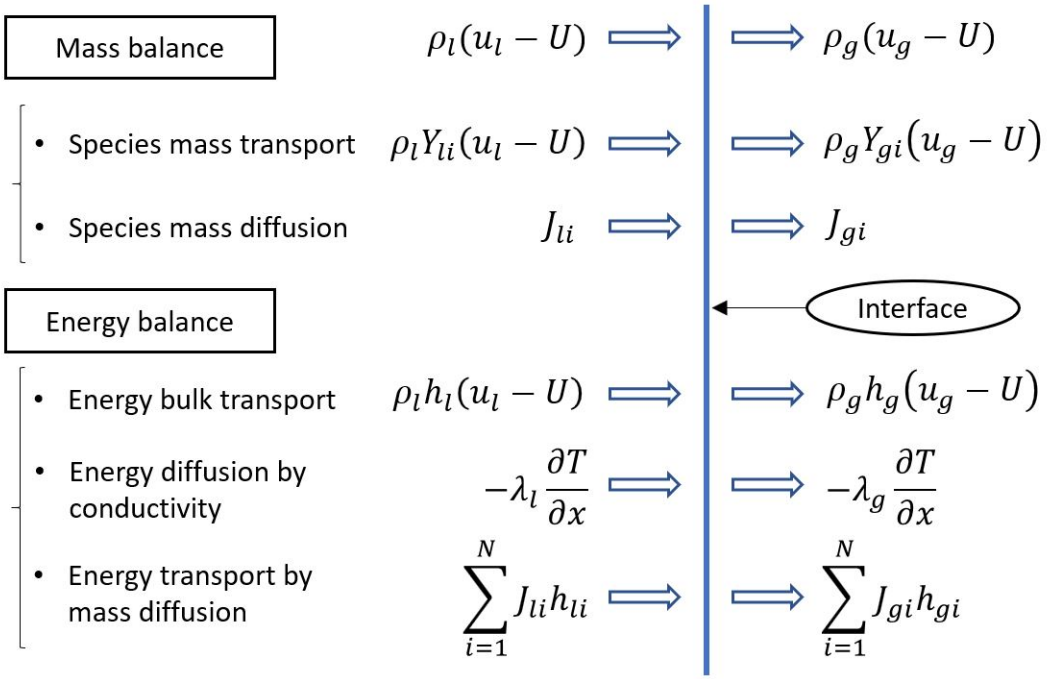

Figure 2.2: Mass and energy balances across the interface.

2.5 Methodology comparison

This section presents a comparison of the methodology applied by different researchers when solving high pressure or supercritical pressure conditions. That is, it identifies which equations of state are used, what fluid properties models, etc. Specifically, it is shown if the liquid phase is considered, what equation of state is implemented, which models are used for computing ideal gas properties, viscosity and thermal conductivity and if the diffusion model takes into account non-idealities (i.e., includes the evaluation of the thermodynamic factor) and what model is used to compute the diffusion coefficients.

Table 2.2: Methodology comparison between different works.

Work	Liquid	EoS	Ideal gas	μ	λ	Diffusion	D_{ij}
This work	Yes	SRK	Passut [53]	Chung [61]	Chung [61]	Non-ideal	Leahy [47]
Bellan [5]	No	PR	-	Poling [52]	Poling [52]	Non-ideal	Harstad [37]
Dahms [6]	Yes	BWR	CHEMKIN	Ely [62]	Ely [63]	-	Takahashi [64]
He [23]	Yes	PR	Yaws [65]	Chung [61]	Chung [61]	Non-ideal	TLSM [59]
Huo [42]	No	SRK	-	Chung [61]	Chung [61]	Ideal	Takahashi [64]
Jorda [43]	No	SRK	CHEMKIN	Chung [61]	Chung [61]	Ideal	Turns [54]

The reasons for selecting the methodology applied to the present work have been explained throughout the text, but summarizing them here is of special interest.

First, supercritical injection is crucial for liquid-based fuel injectors. Therefore, including this two-phase model was a requirement of this thesis. Then, the modeling of fluid properties has to take into account two main factors, which are accuracy and manageability of the implemented models. Because of this, the use of a cubic equation of state is preferable. It may not provide the same accuracy as other methods, but it becomes easy and efficient to implement in a numerical code and some modifications can be made to improve its performance.

Using further correlations to compute ideal gas properties, viscosity and thermal conductivity is also easy to implement in a code and the available methods provide enough accuracy

in the thermodynamic space of our simulations. Linking the code with other software, such as CHEMKIN, to obtain these properties may become tedious. Finally, due to our high-pressure conditions, the diffusion model had to be computed assuming non-idealities. In this model, the selected correlations to compute diffusion coefficients has been chosen according to accuracy provided and date of publication, since diffusion models improve as more experimental data becomes available.

Chapter 3

Numerical Method

3.1 Discretization of the equations

The governing equations are discretized using finite volume techniques or the finite-volume method (FVM), keeping in mind further modifications to work with 2-D and 3-D domains. For a 1-D domain, the control volumes are defined as seen in Figure 3.1, where the node of interest i (referred as P) is related to its neighbors $i+1$ (east, E) and $i-1$ (west, W). The definition of the cell width Δx and distances between nodes dxe and dxw is also defined in the same figure. It is important to note that the mesh does not need to be uniform, so the developed code could work for non-uniform meshes.

Another feature of the selected discretization is that the code works with a staggered mesh. This is, velocities are stored at the cell faces e and w, while all other variables (temperature, density, etc.) are stored in the nodes of each control volume. The diffusion mass flux is also computed at the cell faces, since it could be also related to a diffusion velocity term.

Moreover, when dealing with the interface, since its location is prescribed without neces-

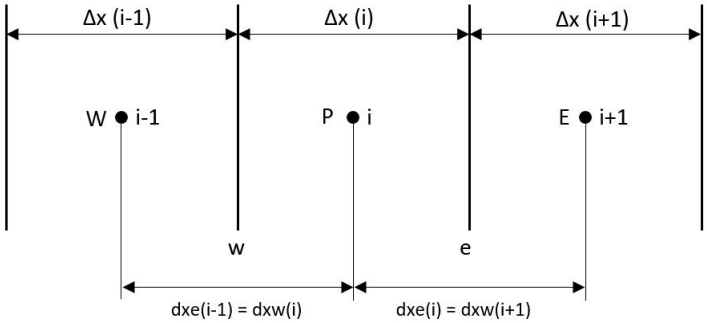

Figure 3.1: Control volume discretization of the 1-D domain.

sarily falling on a node, it will be treated as a face between the nodes on each side of it, IL and IR. As specified by the matching conditions, a discontinuity will exist for the following variables at the interface: species concentration, density and velocity.

Although it would be better to use the conservative forms of the governing equations if the finite-volume method is implemented; it can still be developed from the non-conservative equations. For further improvements of this work, especially once we move to 2-D or 3-D configurations, it may be necessary to rearrange the governing equations in conservative form and use the classical procedures of FVM.

Following FVM discretization techniques [66], the discretization of the governing equations from Section 2.2 is shown in the following lines. The temporal integration has been taken to be explicit first order approximation, which is shown to be enough for other works similar to this [23]. Explicit time integration allows us to treat the discretization of the equations in a simpler way, since the coupling of different terms could complicate things, especially in the energy equation (Eq. 2.8 and Eq. 2.9). The inclusion of explicit approaches with higher orders (Runge-Kutta methods) would ease the restrictions on the time step that explicit methods impose (in any case, more restrictive than implicit methods). However, since we are interested in the early stages of temporal evolution, at this point having a small time step is necessary.

The global continuity equation for each phase (Eq. 2.1 and Eq. 2.2) is discretized implicitly. It becomes

$$\frac{\rho_P^{n+1} - \rho_P^n}{\Delta t} V_P + [(\rho u)_e^{n+1} - (\rho u)_w^{n+1}] \Delta y \Delta z = 0 \tag{3.1}$$

The species continuity equation for each phase and species (Eq. 2.4 and Eq. 2.5) becomes

$$\rho_P^n \frac{Y_{P,i}^{n+1} - Y_{P,i}^n}{\Delta t} V_P + (\rho_P u_P)^n [Y_{e,i}^n - Y_{w,i}^n] \Delta y \Delta z + [J_{e,i}^n - J_{w,i}^n] \Delta y \Delta z = 0 \tag{3.2}$$

and the energy equation for each phase (Eq. 2.8 and Eq. 2.9) is discretized as

$$\begin{aligned} &\rho_P^n \frac{h_P^{n+1} - h_P^n}{\Delta t} V_P + (\rho_P u_P)^n [h_e^n - h_w^n] \Delta y \Delta z - \rho_P^n \sum_{i=1}^{N} h_{P,i}^n \frac{Y_{P,i}^{n+1} - Y_{P,i}^n}{\Delta t} V_P \\ &- (\rho_P u_P)^n \sum_{i=1}^{N} h_{P,i}^n [Y_{e,i}^n - Y_{w,i}^n] \Delta y \Delta z - \left[\left(\lambda \frac{\partial T}{\partial x} \right)_e^n - \left(\lambda \frac{\partial T}{\partial x} \right)_w^n \right] \Delta y \Delta z \\ &+ \sum_{i=1}^{N} J_{P,i}^n [h_{e,i}^n - h_{w,i}^n] \Delta y \Delta z = 0 \end{aligned} \tag{3.3}$$

In the previous equations, the subscript P refers to the node we are solving for, while the subscripts e and w refer to the faces of the cell associated to that node. The superscripts $n+1$ and n refer to the new time step and the old time step, respectively. Thus, we can see the explicit nature of the discretized equations.

The grid parameters V_P and Δy refer to the volume of the cell and the cell size in the y-direction, respectively. Since we are discussing a 1-D problem, $\Delta y = 1$ to make it non-dependent in that direction and $V_P = \Delta x \Delta y \Delta z = \Delta x$.

There are some clarifications to be made in this section. Recall that velocity and diffusion mass fluxes are evaluated at the cell faces and in Eq. 3.2 and Eq. 3.3 these variables are needed at the center of the cell. However, the center of the cell corresponds to the face of the staggered cells. That is, computing u_P can be done using the same procedure to compute $Y_{e,i}$. Since we are discussing a problem mainly driven by diffusion, velocities are small and, thus, we can use central differences to evaluate the different variables at the corresponding cell face, which is a second order scheme. Therefore, velocity and diffusion mass flux are evaluated at P as,

$$u_P = \frac{1}{2}(u_e + u_w) \tag{3.4}$$

$$J_{P,i} = \frac{1}{2}(J_{e,i} + J_{w,i}) \tag{3.5}$$

and variables such as enthalpy or mass fractions are evaluated at the cell faces as,

$$Y_{w,i} = \frac{1}{2}(Y_{P,i} + Y_{W,i}) \tag{3.6}$$

$$Y_{e,i} = \frac{1}{2}(Y_{P,i} + Y_{E,i}) \tag{3.7}$$

Finally, the temperature gradients evaluated at the cell faces is computed as,

$$\left(\frac{\partial T}{\partial x}\right)_e = \frac{T_E - T_P}{\mathrm{dxe}} \tag{3.8}$$

$$\left(\frac{\partial T}{\partial x}\right)_w = \frac{T_P - T_W}{\text{dxw}} \tag{3.9}$$

where dxe and dxw are the distances between nodes as defined in Figure 3.1.

3.2 Algorithm

The partial differential equations (PDE) from Section 2.2 are solved using the discretization techniques shown in Section 3.1. The temporal integration is done using a time-marching explicit method [67] as said before. However, some disadvantages of using this method exist. That is, the time step becomes bounded by the Courant-Friedrichs-Lewy (CFL) conditions [68],[69] (Eq. 3.10 and Eq. 3.11) to ensure numerical stability. In this case, reaching a desired time in the simulation can require many time steps, increasing the computational costs. In principle, this issue is not important for us, since at the early times a small time step is required, possibly smaller than that required under the CFL conditions.

$$\Delta t \left(\frac{|u_i|}{\Delta x_i}\right)_{\max} \leq C_{\text{conv}} \tag{3.10}$$

$$\Delta t \left(\frac{\nu}{\Delta x_i^2}\right)_{\max} \leq C_{\text{visc}} \tag{3.11}$$

The CFL condition from Eq. 3.11 can be applied to any diffusive process, not just viscosity (ν) as it was originally referred to. Generally, the values of the Courant numbers (C_{conv} and C_{visc}) that ensure stability will need to be adjusted. Nevertheless, some recommendations for these values are available in the literature [68],[70]. What must always be satisfied is for the Courant number to be equal or less than unity, since it expresses a ratio of the time that

a particle takes to cross a cell of the discretized domain.

In our problem, we do not have viscous diffusion since we are not working with the momentum equation. Thus, Eq. 3.11 is not necessary to be implemented at this stage. However, we do have two other diffusive processes: mass diffusion (Eq. 3.12) and thermal diffusion (Eq. 3.13), which can be accounted as seen in He and Ghoniem [23]. In their work, some other recommendation for the value of the Courant numbers are suggested. Recall that the mass diffusion coefficient is D_{jk} and the thermal diffusion coefficient is $\alpha = \lambda/(\rho C_P)$.

$$\Delta t \left(\frac{D_{jk,i}}{\Delta x_i^2} \right)_{\max} \leq C_{\text{diff}} \tag{3.12}$$

$$\Delta t \left(\frac{\lambda_i}{\Delta x_i^2 \rho_i C_{p,i}} \right)_{\max} \leq C_{\text{thermal}} \tag{3.13}$$

The algorithm of the code works as follows. First, the initial conditions of our equations are set. Then, the solution algorithm will first solve explicitly the species continuity equation and the energy equation, obtaining mass fractions and temperature at the new step (n+1) from the available information of step (n), as seen in Figure 3.2. To solve any variable for the node P at (n+1), the code requires information of that variable on the node P, E and W at (n). If the node P is a neighboring node of the interface, it uses previously computed values of the matching conditions at the interface.

It is easy to realize that the interface acts as a face or boundary of our domain, imposing certain conditions to be satisfied (i.e., the matching conditions). Therefore, the solution of the equations is taken in two separate domains: the liquid phase and the gas phase. Each one of them presents boundary conditions defined at the interface and at "infinity". A full detailed description of the boundary conditions is shown in Section 3.4.

Once the mass fractions and temperature have been computed throughout the domain, matching conditions at the interface are solved using the new computed values for the mass and mole fractions and temperature on the neighboring nodes of the interface. Therefore, this solution is taken implicitly using the values of the variables at the new time step. It allows us to obtain the temperature at the interface, mass and mole fractions and relative velocities of the fluid on each side of it for the new time step, too. The procedure explaining how to solve the matching conditions is explained in Section 3.3.

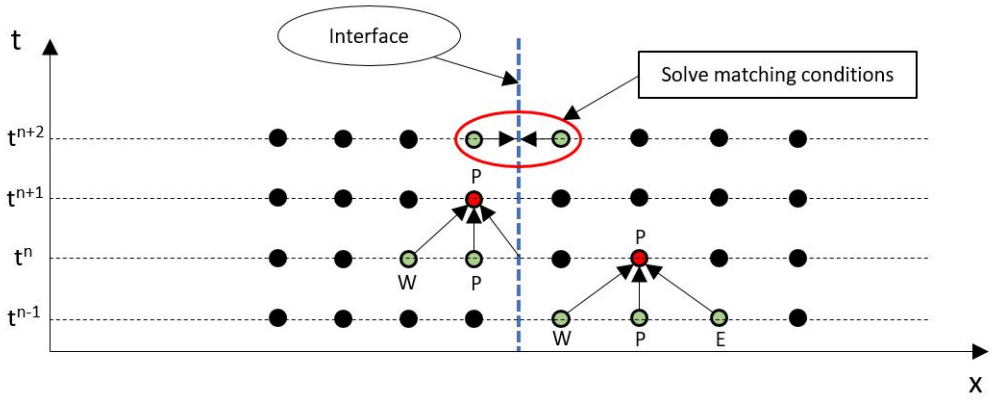

Figure 3.2: Sketch of the proposed time integration.

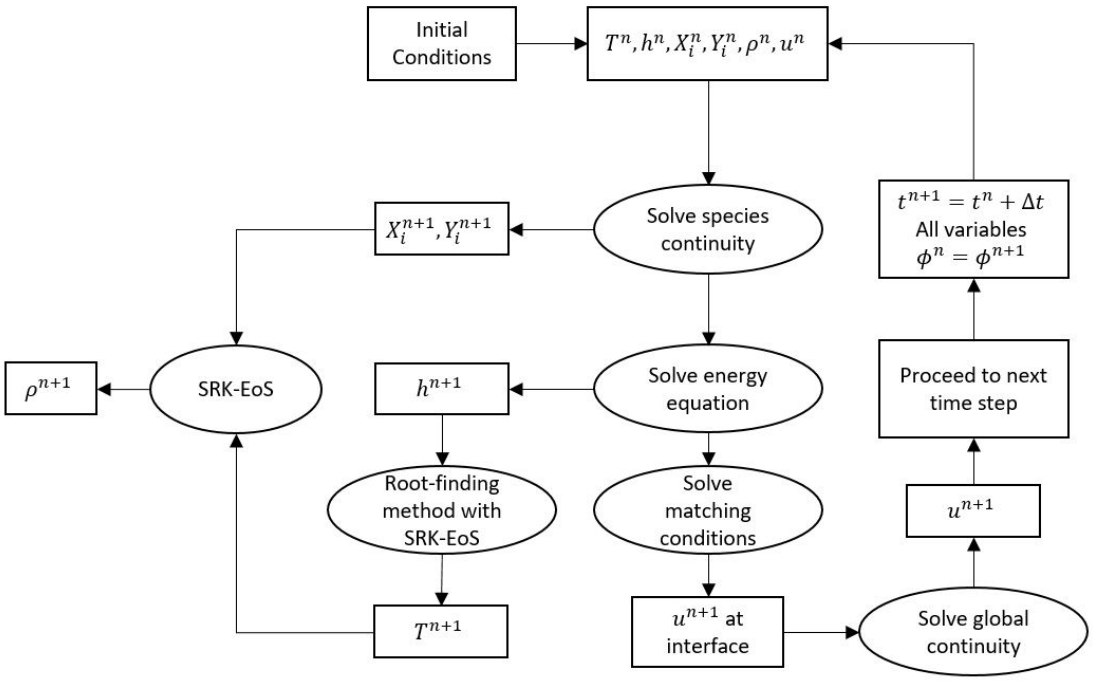

Figure 3.3: Flow diagram of the solution algorithm.

When working with a fixed interface location in time, the interface velocity U becomes zero and the relative velocities $\hat{u}_l$ and $\hat{u}_g$ become the actual fluid velocities at the interface. Thus, a simple numerical integration of Eq. 2.1 and Eq. 2.2 from each side to the interface to "infinity" allows us to obtain the velocity field for both the liquid and gas phases. Since in this frame of reference the liquid will be flowing into the interface, we can identify the velocity the interface would have if the liquid was sitting on a wall and vaporizing under the studied conditions. This velocity, which gives us an idea of how fast the interface is moving, is given by the velocity at $x \to -\infty$.

For this approach to be done, we would need to balance momentum at the ends of our domain, where a velocity different than zero is present. Otherwise, the interface would be moving. However, working with high pressures allows us to discuss that momentum terms such as ρu^2 are far less important than pressure terms, so they can be neglected and no balance is needed as a first approximation. When checking this issue, it is only seen that at the very first time steps neglecting the momentum balance may be a wrong assumption, but rapidly becoming admissible. As pressure is reduced, this assumption may become even wrong at large simulation times; so, care is needed.

At this point, all variables have been evaluated for a particular time step and we can proceed to the following step and repeat the aforementioned procedure. For a more schematic view, Figure 3.3 presents the algorithm as a flow diagram.

3.3 Solution method for the matching conditions

The matching conditions shown in Section 2.4 become a closed system of equations when working with the relative velocities of the liquid phase and the gas phase with respect to the interface velocity U,

$$\hat{u}_g = u_g - U \tag{3.14}$$

$$\hat{u}_l = u_l - U \tag{3.15}$$

For a mixture of N species, we have a system of 2N+7 equations for 2N+6 variables to be solved. There is no need to count an equation for pressure matching since under our assumptions pressure is constant throughout the domain. Nevertheless, the matching conditions for global continuity and species continuity are related through the summation over all species of the species mass balances, so the system actually becomes 2N+6 equations. Multi-component phase equilibrium algorithms are shown in different works [23], [43], [55], [56], each one under certain conditions to be met. However, this work currently focuses on binary mixtures.

For a binary mixture (N=2), where we have species A and B, the phase equilibrium solution provides two points in the thermodynamic space; so it is decoupled from the diffusion mass fluxes. If mixtures with $N > 2$ are considered, the phase equilibrium compositions must be compatible with the mass fluxes across the interface. For the binary mixture, the system of equations becomes

$$\rho_g \hat{u}_g = \rho_l \hat{u}_l \tag{3.16}$$

$$\rho_g Y_{gA} \hat{u}_g + J_{gA} = \rho_l Y_{lA} \hat{u}_l + J_{lA} \tag{3.17}$$

$$\rho_g Y_{gB} \hat{u}_g + J_{gB} = \rho_l Y_{lB} \hat{u}_l + J_{lB} \tag{3.18}$$

$$X_{gA}\Phi_{gA} = X_{lA}\Phi_{lA} \tag{3.19}$$

$$X_{gB}\Phi_{gB} = X_{lB}\Phi_{lB} \tag{3.20}$$

$$X_{gA} + X_{gB} = 1 \tag{3.21}$$

$$X_{lA} + X_{lB} = 1 \tag{3.22}$$

$$\rho_l \hat{u}_l (h_l - h_g) - \lambda_l \left(\frac{\partial T}{\partial x}\right)_l + \sum_{i=1}^{2} J_{li} h_{li} = -\lambda_g \left(\frac{\partial T}{\partial x}\right)_g + \sum_{i=1}^{2} J_{gi} h_{gi} \tag{3.23}$$

$$T_{l,\mathrm{int}} = T_{g,\mathrm{int}} \tag{3.24}$$

$$\left(\frac{\partial T}{\partial x}\right)_l = f(T_{l,\mathrm{int}}, T, x) \tag{3.25}$$

$$\left(\frac{\partial T}{\partial x}\right)_g = f(T_{g,\mathrm{int}}, T, x) \tag{3.26}$$

Summarizing, from Eq. 3.16, Eq. 3.17 and Eq. 3.18, which provide matching conditions for mass flux, only two of them are needed to be solved. Eq. 3.23 provides information for the energy flux balance. Finally, Eq. 3.19, Eq. 3.20 and Eq. 3.24 become the phase equilibrium requirements.

Additionally, Eq. 3.21 and Eq. 3.22 relate mole fractions of each species in each phase and Eq. 3.25 and Eq. 3.26 provide information on the temperature gradient on each side of the interface in terms of the interface temperature and the temperature and location of each node surrounding it. A full analysis on how to compute these gradients is shown in Section 3.3.1.

This system of equations can be simplified to one equation depending only on the interface temperature T_{int}. Then, it can be solved with any root-finding algorithm, such as the Secant Method. The derivative of the objective function cannot be easily obtained in order to use the Newton-Raphson method [45],[54].

Recognizing that all terms in Eq. 3.23 can ultimately depend on temperature for a given pressure, the final problem consists in finding the root of $f(T_{\text{int}})$, being it

$$f(T_{\text{int}}) = \rho_l \hat{u}_l (h_l - h_g) - \lambda_l \left(\frac{\partial T}{\partial x}\right)_l + \sum_{i=1}^{2} J_{li} h_{li} + \lambda_g \left(\frac{\partial T}{\partial x}\right)_g - \sum_{i=1}^{2} J_{gi} h_{gi} \tag{3.27}$$

Given a value for T_{int}, Eq. 3.19, Eq. 3.20, Eq. 3.21 and Eq. 3.22 form a decoupled closed system to solve for the mole fractions of each species on each side of the interface. A simply iterative procedure can be used to solve these equations: from guessed values for the mole fractions, the fugacity coefficients are obtained using the SRK-EoS and, rearranging the equations, the new computed values for the mole fractions become

$$X_{gB} = \frac{1 - \Phi_{gA}/\Phi_{lA}}{\Phi_{gB}/\Phi_{lB} - \Phi_{gA}/\Phi_{lA}} \tag{3.28}$$

$$X_{lB} = X_{gB}\frac{\Phi_{gB}}{\Phi_{lB}} \tag{3.29}$$

$$X_{gA} = 1 - X_{gB} \tag{3.30}$$

$$X_{lA} = 1 - X_{lB} \tag{3.31}$$

and an iterative procedure is done until the desired convergence is achieved.

Once mole fractions are known, mass fractions, density, enthalpy, diffusion mass fluxes and thermal conductivity on each side of the interface are readily known for a given temperature, either by using the EoS or the corresponding model.

Temperature gradients can be obtained using Eq. 3.25 and Eq. 3.26 and, after some rearranging of the mass balance equations, the relative velocities $\hat{u}_l$ and $\hat{u}_g$ can be expressed as

$$\hat{u}_g = \frac{\rho_l}{\rho_g}\hat{u}_l \tag{3.32}$$

$$\hat{u}_l = \frac{J_{lA} - J_{gA}}{\rho_l(Y_{gA} - Y_{lA})} \tag{3.33}$$

With all these considerations, it is possible to solve for the root of Eq. 3.27 and obtain a converged solution for the interface temperature that satisfies the matching conditions.

3.3.1 Computation of gradients at the interface

At the interface, we know information of our variables by approaching only from one side of the interface (i.e., left side for the liquid phase and right side for the gas phase). Therefore, using central differences to compute the gradient at the interface is not valid. To compute it, an approach considering the gradient at the interface to be the same as the gradient computed as $(\partial T/\partial x)_l = (T_{l,\text{int}} - T(IL))/\Delta x$ could be done. However, we are only using one known value of the temperature field close to the interface and the computed gradient could be wrong. To solve this issue, the temperature gradient is computed using more known points based on a second-order Taylor series expansion at the interface (Eq. 3.34).

$$f(x) = f(a) + \frac{f'(a)}{1!}(x-a) + \frac{f''(a)}{2!}(x-a)^2 + O(x^3) \tag{3.34}$$

From the Taylor series expansion, we can determine any value around the interface. The point a becomes the location of the interface and $f(a)$ the value of the variable of interest at the interface (e.g., temperature). Implementing the expansion to two points (at IL and $IL-1$ or at IR and $IR+1$) we can solve for the first derivative of the variable at the interface (i.e., the gradient). Solving the system, we get

$$\left(\frac{\partial T}{\partial x}\right)_g = \frac{T(IR+1) - T_{int} + \frac{T_{int}-T(IR)}{(\Delta x_{1,g})^2}\left(\Delta x_{1,g} + \Delta x_{2,g}\right)^2}{\left[(\Delta x_{1,g} + \Delta x_{2,g}) - \frac{1}{\Delta x_{1,g}}(\Delta x_{1,g} + \Delta x_{2,g})^2\right]} \tag{3.35}$$

$$\left(\frac{\partial T}{\partial x}\right)_l = \frac{T(IL-1) - T_{int} + \frac{T_{int}-T(IL)}{(\Delta x_{1,l})^2}\left(-\Delta x_{1,l} - \Delta x_{2,l}\right)^2}{\left[-(\Delta x_{1,l} + \Delta x_{2,l}) + \frac{1}{\Delta x_{1,l}}(-\Delta x_{1,l} - \Delta x_{2,l})^2\right]} \tag{3.36}$$

The same approach can be done to compute the gradients of the mass fractions at the interface, since they are needed to find the diffusion mass fluxes. The parameters from Eq.

3.35 and Eq. 3.36 are defined in Figure 3.4.

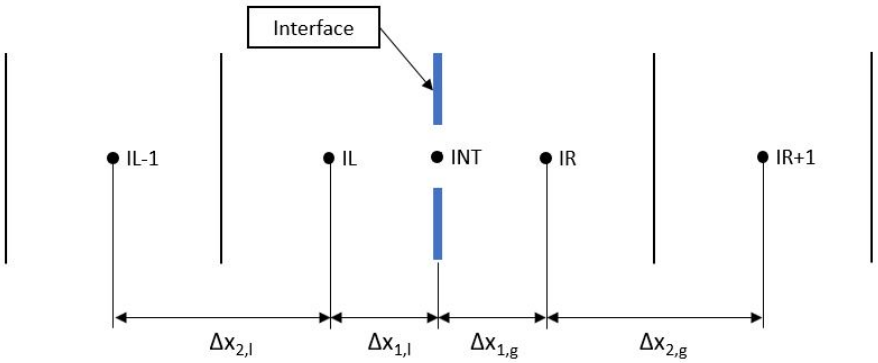

Figure 3.4: Approach to compute gradients at the interface.

3.4 Boundary conditions and initial conditions

The solution of the governing equations will be determined by the boundary conditions and the initial conditions we impose in our domain. As said in the previous lines, the numerical domain is divided in two sections: the liquid phase and the gas phase.

Each domain will have its boundary conditions, imposed at the "infinite" location and at the interface. To solve the energy equation and the species continuity equations, which are second-order PDEs, we need two boundary conditions. We want the pure liquid and the pure gas to come from a fixed temperature reservoir, different for each phase. Under these conditions, temperature and mass fractions are imposed at the "infinite" locations. On the other hand, the matching conditions at the interface will impose temperature and mass fractions at the interface location. Thus, we are implementing Dirichlet boundary conditions to both the energy equation and the species continuity equation.

To solve continuity, only one boundary condition is needed since it is a first-order PDE. In this case, matching conditions will determine the velocity of each phase at the interface, assuming the interface to be fixed (i.e., $U = 0$). Again, these velocities become a Dirichlet

boundary condition for the continuity equation.

Finally, we need to discuss the initial conditions implemented in the simulations. Since we want to estimate the initial behavior of a liquid suddenly introduced into a gaseous environment, the liquid phase is set to be composed only by the pure liquid species and at the reservoir temperature while the gas phase is set to be composed by the pure gas species at the respective reservoir temperature.

3.5 Grid independence study

The validity of the code is checked by doing a grid independence study for a test case. Precisely, it has been chosen as a test case the problem composed by liquid n-decane ($C_{10}H_{22}$) in contact with gaseous oxygen (O_2). The pure liquid temperature at the left end of our domain is set to 450 K and the pure gas temperature at the right end of the domain is set to 550 K. Pressure is kept constant at $P_r = 2 \rightarrow P = 4.206$ MPa, that is, twice the critical pressure of pure n-decane ($P_c = 2.103$ MPa). Table 3.1 shows the 9 test cases, refining both the mesh size, Δx, and the time step size, Δt.

Table 3.1: Test cases for the grid independence study (a).

Δt	400 nm	200 nm	100 nm
50 ns	C1	C2	C3
5 ns	C4	C5	C6
0.5 ns	C7	C8	C9

Since our domain is set large enough to be considered "infinite" for our physical phenomena around the interface, we expect the interface to reach steady-state values for the velocity, the temperature, etc. Therefore, it seems reasonable to compare steady-state solutions for these interface properties as reference values to check our grid independence. In this case, the interface temperature, T_{int}, and the interface densities, $\rho_{l,int}$ and $\rho_{g,int}$, have been selected

for comparison purposes. Another feature to check is if the domain has actually been set large enough so its size does not affect the obtained result. For the test cases, the length of the domain is 400 μm, with the interface located at 100 μm (liquid on its left side and gas on its right side).

The total simulation time is 100 μs, and the value of our fluid properties at that time is chosen as the reference value to compare with. Furthermore, different profiles of the fluid properties (i.e., temperature, density, etc.) are shown.

The analysis of the study cases shown in Table 3.1 proves the consistency of the code. The following Table 3.2, Table 3.3 and Table 3.4 show results for the obtained interface temperature, gas density and liquid density, respectively. These results are compared to those obtained with case C9, established as the test case with more mesh refinement, both in the spatial domain and the temporal domain. Cases C2, C3 and C6 showed no stable solution, where the CFL conditions are not satisfied.

Table 3.2: Grid independence study: Interface temperature and absolute error compared with C9.

Interface temperature (K)			
Δt	400 nm	200 nm	100 nm
50 ns	456.65418 (225.069 %)	-	-
5 ns	458.89911 (0.576 %)	458.89732 (0.756 %)	-
0.5 ns	458.90312 (0.176 %)	458.90493 (0.006 %)	458.90487 (0 %)

Table 3.3: Grid independence study: Interface gas density and absolute error compared with C9.

Interface gas density (kg/m^3)			
Δt	400 nm	200 nm	100 nm
50 ns	40.86633 (10.367 %)	-	-
5 ns	40.96972 (0.028 %)	40.96963 (0.037 %)	-
0.5 ns	40.96991 (0.009 %)	40.97000 (0 %)	40.97000 (0 %)

One of the main requirements when it comes to decide what mesh is going to be used is the computational costs associated to it. That is, the time it takes the simulation to finish.

Table 3.4: Grid independence study: Interface liquid density and absolute error compared with C9.

Interface liquid density (kg/m^3)			
Δt	400 nm	200 nm	100 nm
50 ns	499.82259 (203.225 %)	-	-
5 ns	497.79557 (0.523 %)	497.79721 (0.687 %)	-
0.5 ns	497.79194 (0.160 %)	497.79029 (0.005 %)	497.79034 (0 %)

Although a clock has not been set to measure exactly the simulation time, the test cases C1 to C9 had a running time ranging from a few minutes to some hours, respectively. In this sense, using the mesh size and the time step of the test case C5 seems reasonable. Its computational cost can be assumed and the absolute deviation with respect to the more refined mesh case is less than 1 % for the variables of interest.

However, only interface properties have been presented so far. There are other issues to be taken into account, such the capacity of the mesh to represent accurately temperature or density distribution around the interface for the early times or the independence of their profiles along the x-axis. It is clear that case C5 seems to provide enough accuracy. Therefore, it is going to be compared with more accurate cases (i.e., cases C8 and C9), to see if there is any appreciable difference between them. The results are shown in Figure 3.5, from which it can be inferred that the cheapest mesh arrangement, C5, is sufficient for our purposes. In this figure, the properties are given at $t = 10$ μs and the interface is located at x = 100 μm and is represented by a dashed line.

Therefore, the final mesh conditions for the simulations performed in this thesis can be set to $\Delta x = 200$ nm and $\Delta t = 5$ ns. Using a finer mesh would rise considerably the computational costs. The only disadvantage of using this spatial discretization is that for early times (i.e., $t \leq 1\mu$s) the resolution of the diffusion layer may becomes under-resolved depending on the diffusivity of the species in the studied mixture, especially affecting the liquid phase. For some low-pressure cases it may be necessary to redefine the mesh.

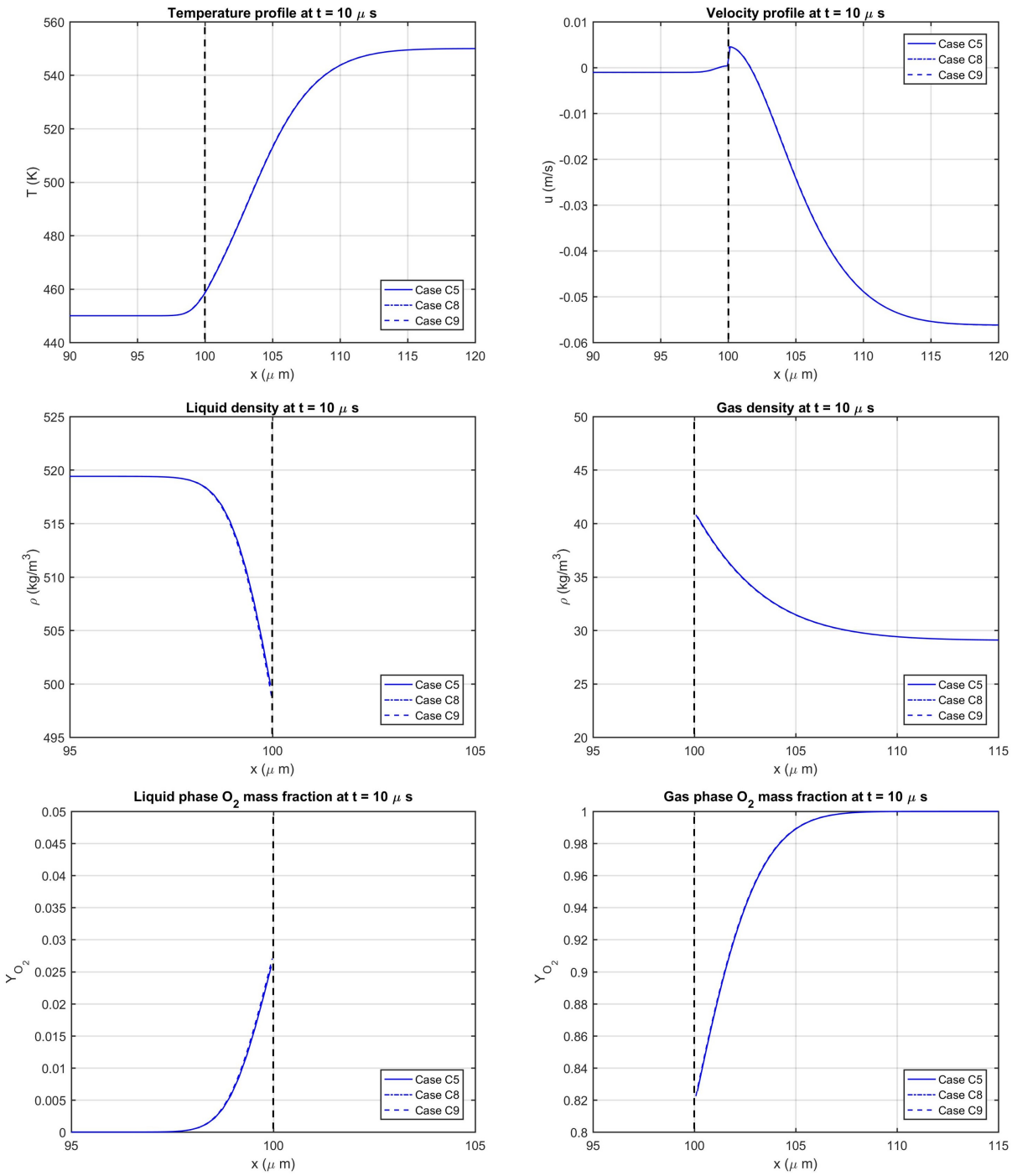

Figure 3.5: Grid independence study: Variable profiles for test cases C5, C8 and C9.

Finally, it is only left to see if the dimensions of the numerical domain are large enough for the interface to behave as if the domain was infinitely large. Taking the mesh discretizations of case C5, it is studied the effects of changing the domain length on the reference variables

at the interface. Table 3.5 summarizes the new test cases.

Table 3.5: Test cases for the grid independence study (b).

Domain length	Cases
200 μm	C5.a
400 μm	C5.b
600 μm	C5.c

The results obtained with these new test cases at $t = 100$ μs are shown in Table 3.6, where it can be seen that the domain size is sufficiently large for the infinite conditions to be valid in any of the cases. This holds true when we only want to simulate up to 100 μs of physical time where diffusion processes occur in a narrowed area around the interface. Value changes are observed to happen in the fifth or sixth decimal.

Table 3.6: Grid independence study: Domain length influence.

Cases	T_{int} (K)	$\rho_{g,int}$ (kg/m^3)	$\rho_{l,int}$ (kg/m^3)
C5.a	458.89732	40.96963	497.79720
C5.b	458.89732	40.96963	497.79721
C5.c	458.89731	40.96963	497.79721

After this grid independence study, it is decided to use a domain length of 400 μm with the interface located at x = 100 μm. The grid size is set to $\Delta x = 200$ nm and the time step to $\Delta t = 5$ ns, as in the test case C5.

Chapter 4

Results

4.1 Phase equilibrium at high pressures

The first question to be addressed in this thesis is the existence of a liquid phase in thermodynamic states well above the critical pressure of the pure liquid being injected. At the interface, the equilibrium conditions between the liquid and the gas phase shown in Section 2.4 (Eq. 2.62, Eq. 2.63 and Eq. 2.64) have to be satisfied.

Contrary to the wrong belief that the liquid fuel cannot exist anymore in that state and transitions to a supercritical state, it is proved that phase equilibrium conditions allow mixing to occur at the interface. When this happens, the mixture critical properties may differ considerably from those of the pure liquid species, thus allowing the liquid phase to be present. This fact is corroborated from other works, such in Jorda-Juanos and Sirignano [55], where the RK-EoS (Eq. 2.12) is used instead of the SRK-EoS (Eq. 2.13) used in the present work. In the Master's Project done by Zembal [56], other equations of state are tested with similar results. Figure 4.1 shows the phase equilibrium results for different pairs of species: oxygen (O_2) and nitrogen (N_2) represent the pure gas species and are combined

with heavy hydrocarbons injected in the liquid state, such as n-octane (C_8H_{18}), n-decane ($C_{10}H_{22}$) and n-dodecane ($C_{12}H_{26}$).

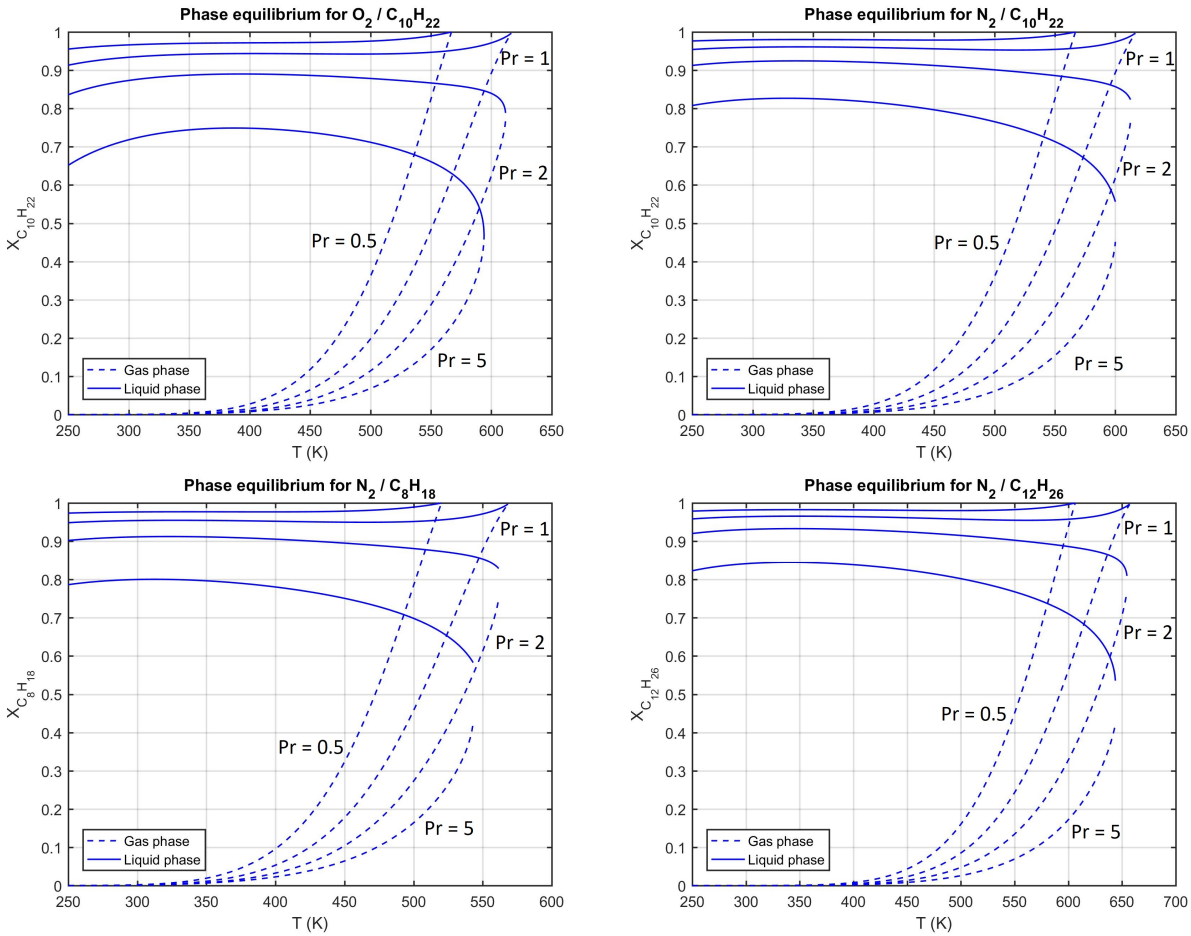

Figure 4.1: Phase equilibrium results for different pairs of species.

The plots show different curves for different reduced pressures expressed in terms of the liquid or fuel species critical pressure, $p_r = p/p_{c,fuel}$. For $p_r = 1$, we are at the critical point of the pure liquid and the critical temperature (i.e., where phase equilibrium cannot be satisfied anymore) corresponds to the critical temperature of the pure liquid too. Values for these critical properties are shown in Appendix A.

For pressures below $p_{c,fuel}$, the liquid phase is almost entirely composed by the fuel species, with mole fractions close to unity. That is, almost no diffusion occurs in the liquid phase since solubility of gaseous species is negligible. However, as pressure increases above $p_{c,fuel}$,

this mole fraction is reduced, meaning that gas species is dissolved into the liquid phase more easily to satisfy the equilibrium conditions at the interface. When this happens, mixing of species due to diffusion is enhanced, modifying the critical properties of the new formed mixture. It is observed that for pressures well above $p_{c,fuel}$ two distinguished phases still exist, thus the critical pressure of the mixture is much higher than the critical pressure of the injected fuel.

4.2 The diffusion process: oxygen/n-decane mixture

This section presents results of the diffusive process around the liquid-gas interface for liquid n-decane injected into a gaseous environment composed by oxygen. Results for the pressure effects on our fluid and for the temporal evolution at some specific pressures are shown. Recall that in all cases the interface is located at $x = 100$ μm and is represented by a dashed line. Moreover, it is helpful to clarify again that the liquid phase is sitting on the left side of the interface while the gas yields on the right side. Similar results are shown for liquid n-octane injected into gaseous nitrogen in Appendix F.

4.2.1 Pressure effects

The interface problem for a fluid composed by n-decane and oxygen has been studied for 4 different pressures: one subcritical case at 10 bar and three supercritical cases at 50, 100 and 150 bar, respectively. The critical pressure for n-decane, which defines the subcritical and the supercritical range, is 21.03 bar. As we have seen in Section 4.1, two phases coexist and form the interface we study here, even at supercritical pressures.

The immediate effects on our variables of increasing pressure are shown in Figure 4.2 and Figure 4.3. Plots for the mass fraction of oxygen, density and velocity are shown for both

the liquid and the gas phase. The temperature profile is also given.

From Figure 4.2, it can be identified one of the main changes that occur at supercritical pressures. For the subcritical case (10 bar), almost no gas species has been dissolved into the liquid phase, thus remaining close to the pure liquid that has been injected. For even lower pressures (e.g., 1 bar), this effect would be stronger. This fact reflects the change in behavior of the phase equilibrium results shown in Figure 4.1. Then, as pressure is increased, more gas species is dissolved into the liquid at the interface, allowing diffusion to become more important in the liquid phase.

Another immediate effect of increasing pressure is the increase in density on both phases. That is, the fluid is being compressed as pressure becomes higher. The density profiles for each pressure also show variations due to species diffusion occurring within each phase. The increase in density also relates to a decrease in species diffusion (i.e., high densities oppose the diffusion process). This effect is clearly seen in the penetration of n-decane into the gas phase, where the mass diffusion layer is reduced as pressure increases. The change in composition of the interface as pressure increases may also affect it. However, the liquid phase shows an opposite behavior. As pressure increases, diffusivity may be reduced but more gas species is being dissolved. In this case, we can observe that the diffusion layer on the liquid side can increase, slightly, as pressure increases.

In Figure 4.3, the velocity profiles and the temperature profiles are shown. Far-field velocity is seen to decrease in the gas phase and increase in the liquid phase as pressure increases. That is, enhanced mixing in the liquid phase produces higher density variations which induce higher velocity variations. Furthermore, for a fixed interface, the liquid goes from flowing into the interface to flowing out of it as pressure is increased (the opposite happens for the gas). This is, the change in thermodynamic behavior of our fluid may cause that a clear vaporization problem at low pressures changes to a condensation problem at higher pressures. This result is further analyzed in Section 4.2.4. Finally, the thermal layer

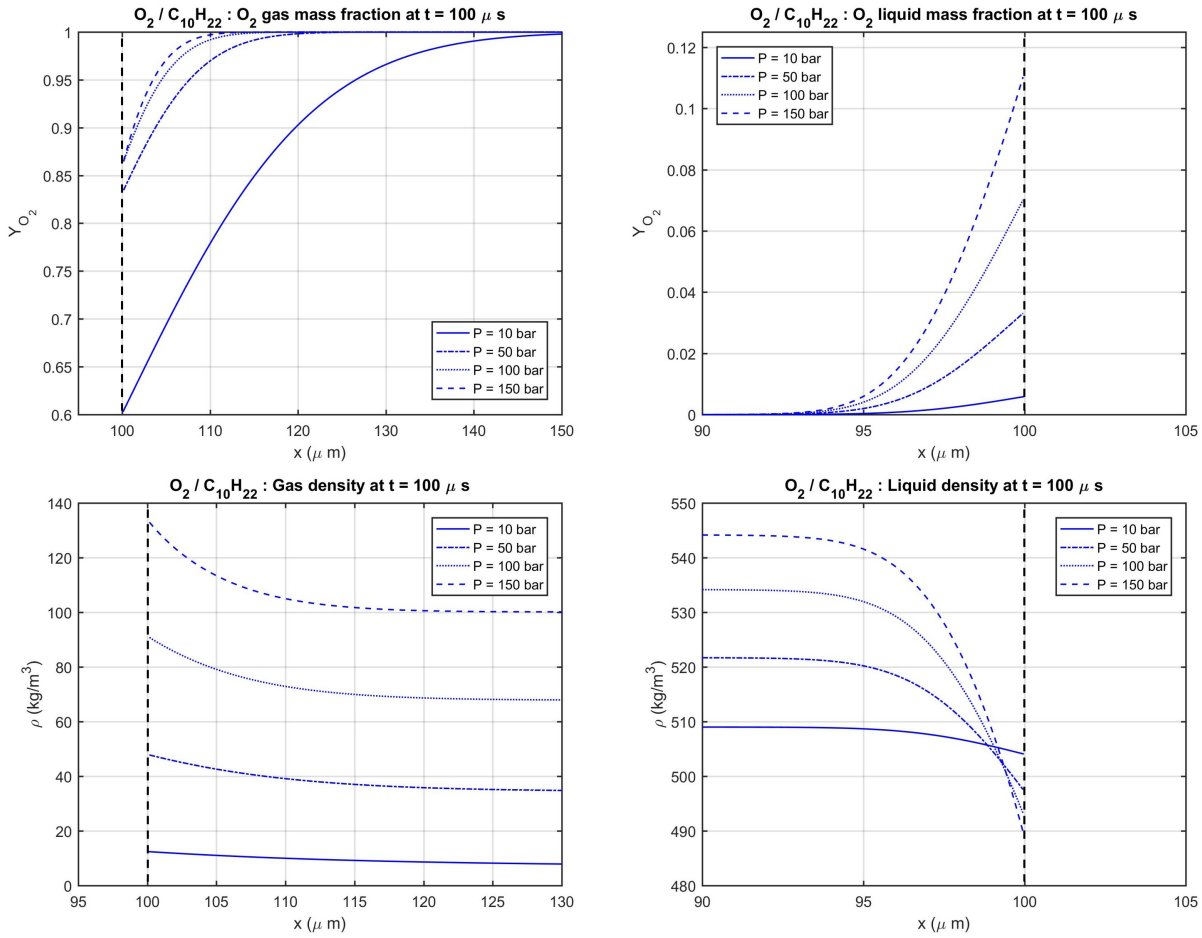

Figure 4.2: Oxygen mass fraction and fluid density on each side of the interface for the oxygen/n-decane mixture.

shows a similar behavior as the diffusion layer, where the increase of pressure translates to a decrease in the layer thickness in the gas phase.

It is also interesting to show how much our fluid deviates from the ideal behavior as pressure is increased. Figure 4.4 shows plots of the normalized enthalpy departure function and entropy departure function with the ideal gas enthalpy, H^*, and the ideal gas entropy, S^*, respectively, computed with the composition of each point in our domain ($(H^* - H)/H^*$ and $(S^* - S)/S^*$). Also, showing how the compressibility factor, Z, changes is interesting, keeping in mind that for an ideal case, $Z = 1$ for a gas and $Z \to 0$ for a liquid.

On the liquid side it is seen that both enthalpy and entropy deviate from the ideal gas

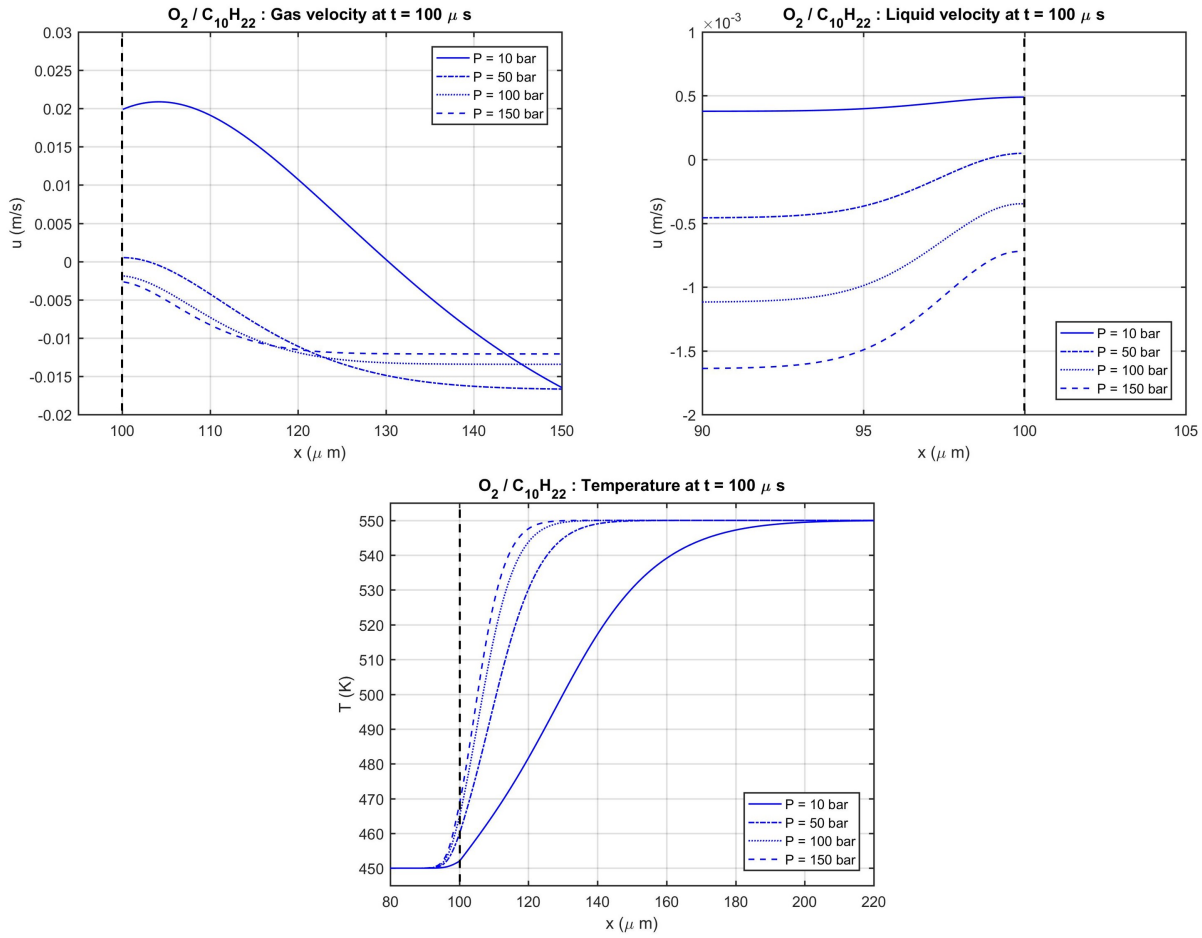

Figure 4.3: Fluid velocity and temperature distribution for the oxygen/n-decane mixture.

values considerably. First of all, this is logical since we are dealing with a liquid phase and not a gas phase. But what becomes interesting is the fact that the deviations become smaller as pressure is increased. This can be explained because the liquid and the gas phase will become very similar close to the critical point of the mixture and the deviations with respect to the ideal gas will tend to be similar. On the gas side, these deviations become larger as pressure increases.

The compressibility factor presents the expected behavior. The gas side becomes more compressed than an ideal gas, thus having $Z > 1$. For the 10 bar case, Z looks very close to 1 as we would expect, since deviations form ideal behavior are small at that pressure. On the liquid side, Z is close to 0. As pressure increases, the compressibility factor of the liquid

increases drastically to values above 1 in the 150 bar case. For the gas phase, as the fluid is highly compressed, the molar volume is reduced. This fact makes the product Pv to become nearly the same in any fluid state, without taking into account v variations due to diffusion. This is why deviations from $Z = 1$ are small. However, compressibility effects are not that strong in the liquid phase and molar volume variations are small and mainly only related to mass diffusion. Therefore, as pressure increases, the product Pv also increases and Z may have values equivalent to those typical of gases.

Finally, some results for the variation of interface properties with pressure are presented. First, Figure 4.5 shows what was said in the grid independence study (Section 3.5), which is that for the treatment of our problem with fixed interface and infinite domain considerations, it is expected that the values for temperature, velocity, density, etc. at the interface will tend to a value.

Then, Figure 4.6 shows how temperature, gas density, liquid density and interface velocity change with pressure. The properties are evaluated at $t = 100$ μs. The interface velocity is computed as if the liquid was sitting on a wall (i.e., $u = 0$ at $x = 0$). Phase equilibrium imposes higher temperatures at the interface as pressure is increased. Also, since pressure increases, the gas density is also increased, but enhanced solubility of light gas species in the liquid phase makes the liquid density decrease with pressure. Lastly, it is observed that the behavior of the interface changes drastically with pressure. For low pressures, the liquid phase is contracting, but as pressure is increased, it reverses its behavior and starts expanding as lighter species are being dissolved more easily.

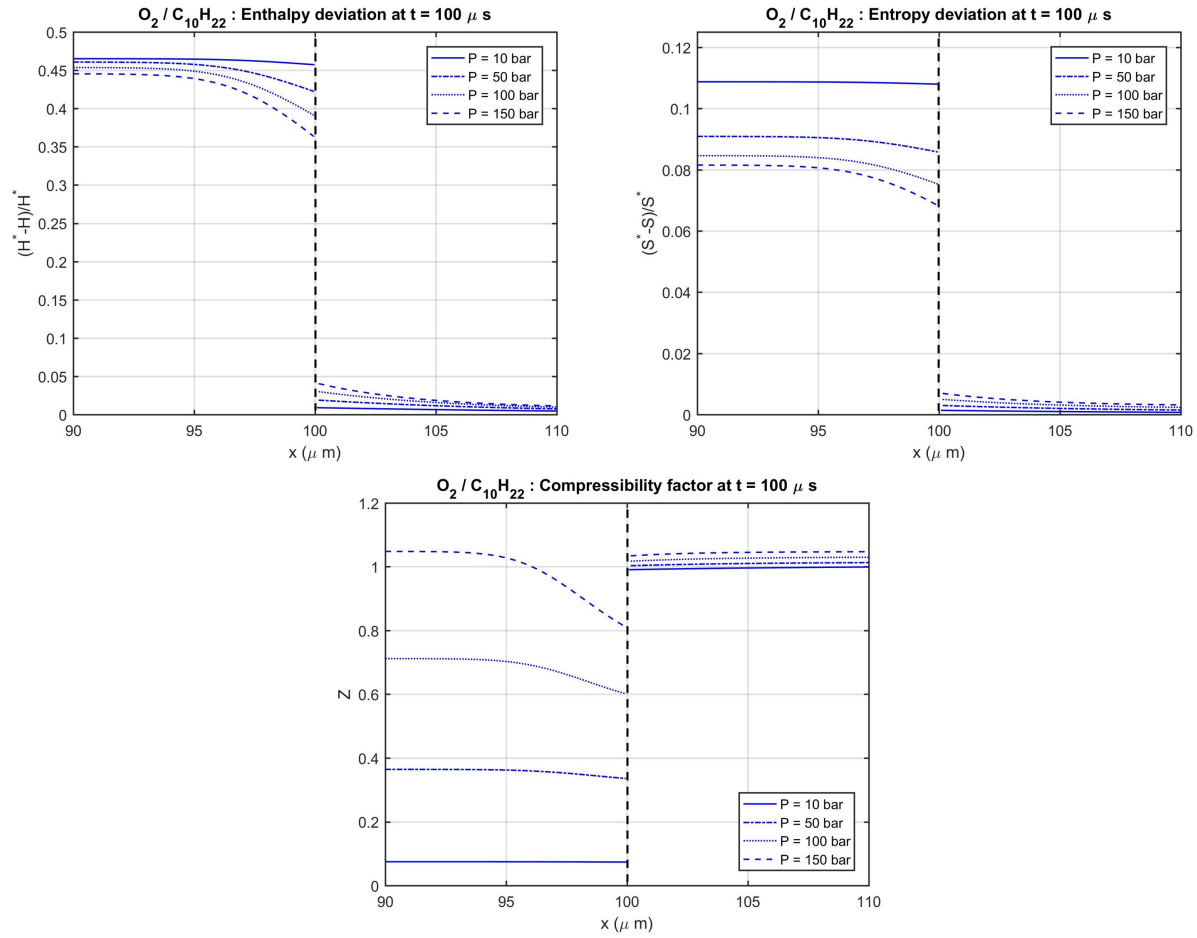

Figure 4.4: Deviations from the ideal case for the oxygen/n-decane mixutre.

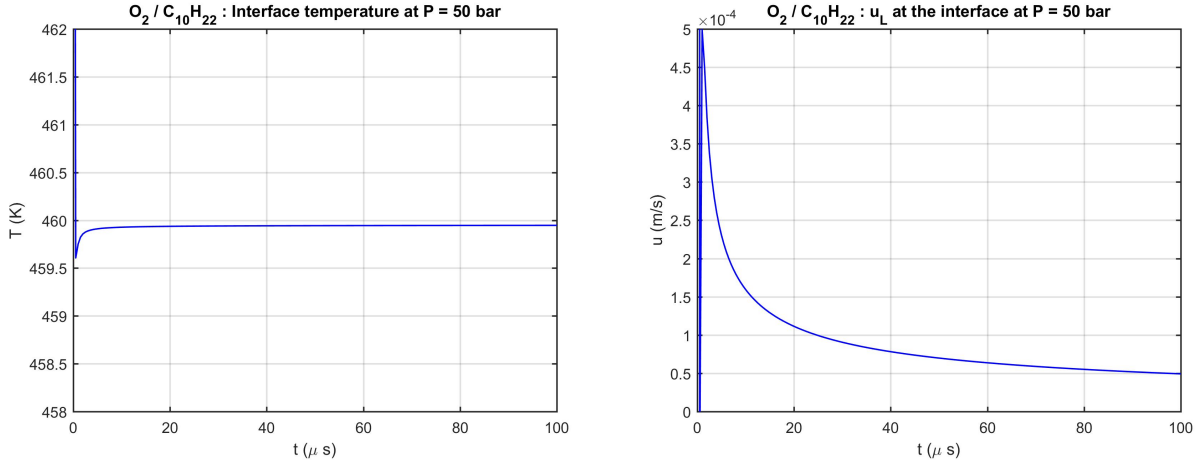

Figure 4.5: Temperature and liquid velocity at the interface for the oxygen/n-decane mixture.

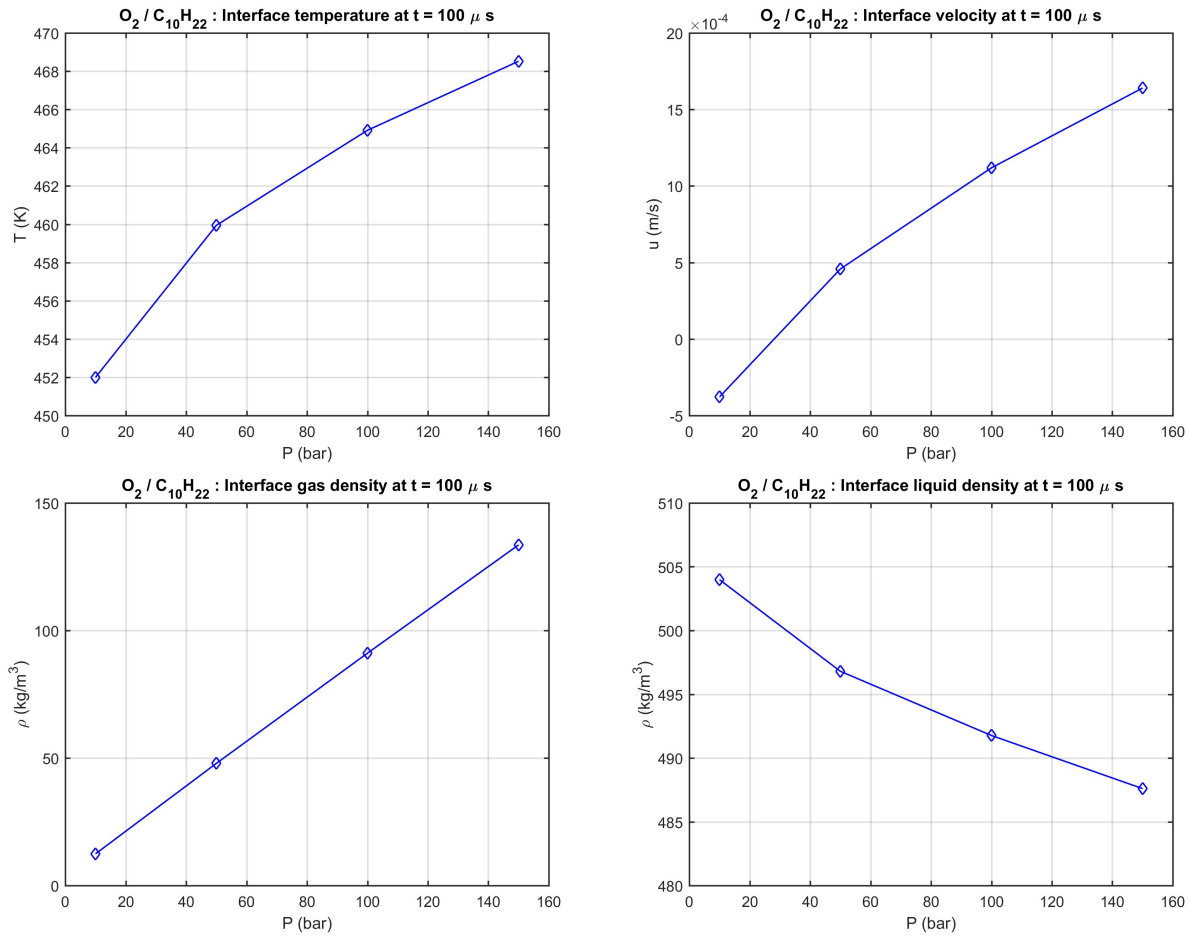

Figure 4.6: Variation of interface properties with pressure for the oxygen/n-decane mixture.

4.2.2 Temporal evolution

This section aims to analyze how fast the diffusion process occurs at high pressures, in order to infer if the changes in the fluid properties due to mass diffusion will be able to affect the breakup mechanisms of liquid injection. For this, the cases at 50 bar and 150 bar are studied.

The temporal evolution of the fluid properties at $p = 50$ bar is shown in Figure 4.7 and the $p = 150$ bar case is shown in Figure 4.8. From these results it is observed that both the thermal layer and the density profile present a similar temporal evolution in their thickness. However, as seen in Figure 4.2, the species diffusion layer is thinner.

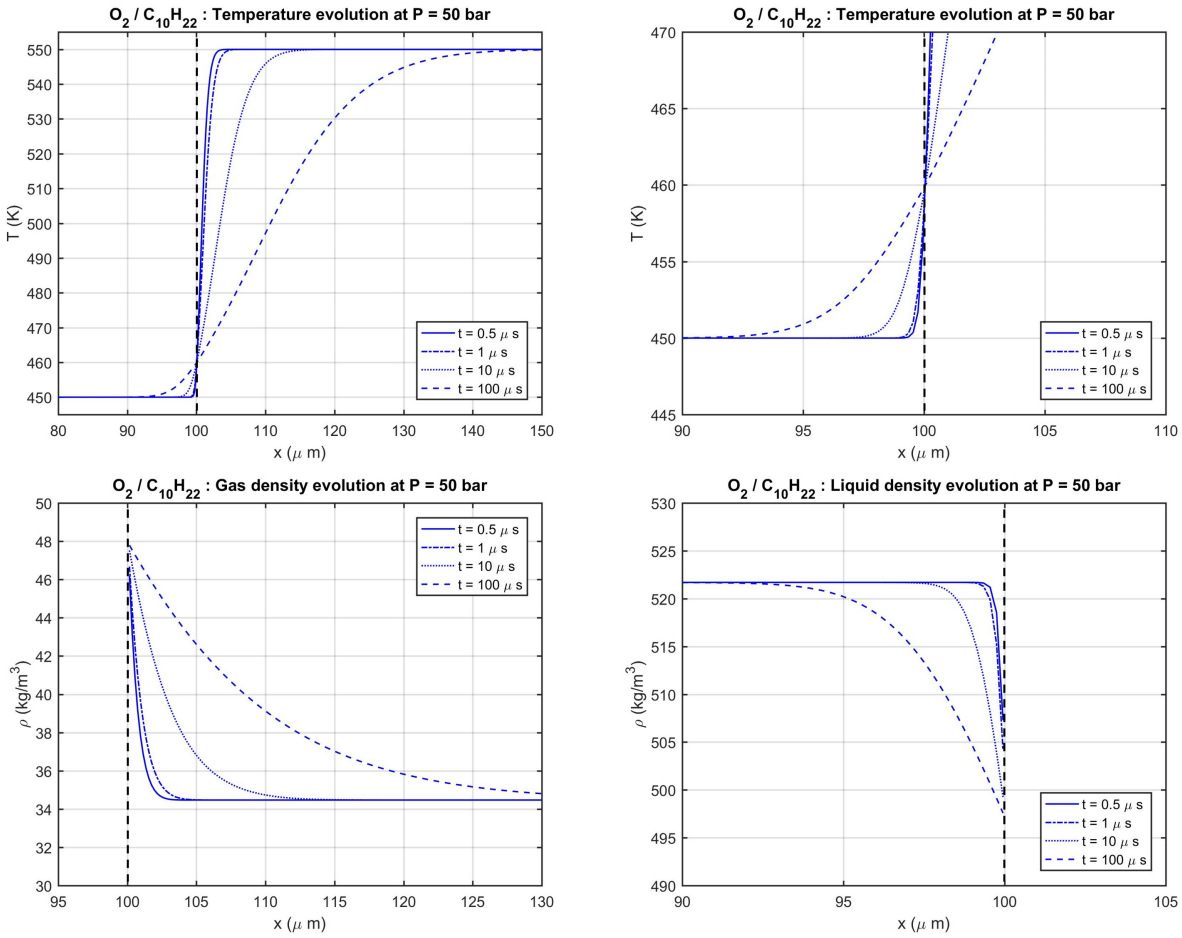

Figure 4.7: Temporal evolution of the temperature distribution and the fluid density for the oxygen/n-decane mixture at p = 50 bar.

The disruption process of a liquid jet usually begins in the temporal range of 20-100 μs [2],[12]. In this time, the fluid properties are seen to change considerably up to 10 μm penetration in the liquid phase and 30 μm in the gas phase. Thus, it is expected that this layer where the fluid properties vary from the pure liquid properties to the pure gas properties will influence the breakup mechanisms, their evolution in time and how they disrupt the liquid structure.

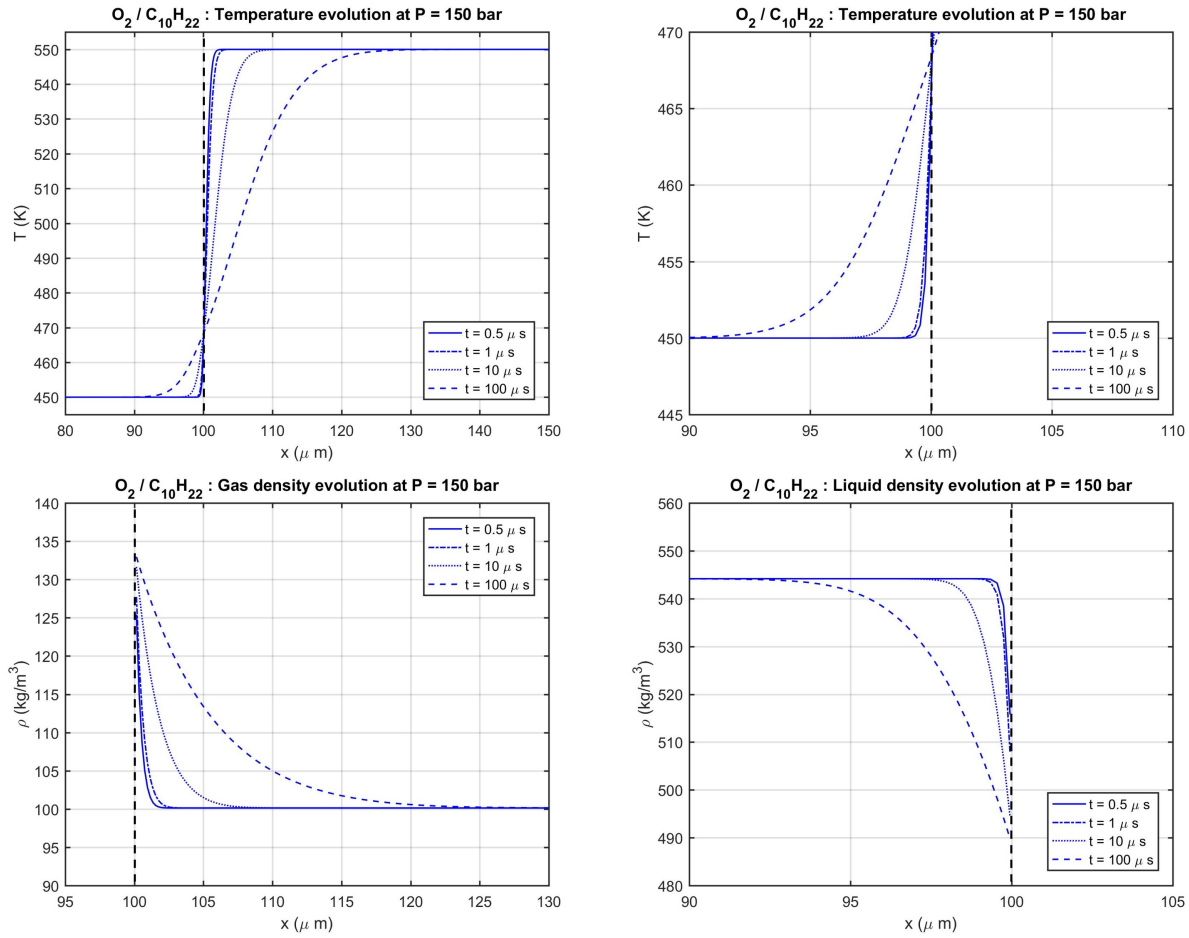

Figure 4.8: Temporal evolution of the temperature distribution and the fluid density for the oxygen/n-decane mixture at p = 150 bar.

4.2.3 Analysis of the equation terms

Up to this point, only the overall results have been discussed. However, it is useful to gain some insight on the physical phenomena by analyzing the influence of each term in our equations. To better understand the diffusion process, both mass diffusion and thermal diffusion, Figure 4.9 presents the profiles of the total derivatives and the local derivatives of mass fraction and enthalpy at $t = 100$ μs. Remember that,

$$\frac{\mathrm{D}Y_i}{\mathrm{D}t} = -\frac{1}{\rho}\frac{\partial}{\partial x}(J_i) \tag{4.1}$$

$$\frac{\partial Y_i}{\partial t} = -\frac{1}{\rho}\left(\rho u \frac{\partial Y_i}{\partial x} + \frac{\partial}{\partial x}(J_i)\right) \tag{4.2}$$

$$\frac{\mathrm{D}h}{\mathrm{D}t} = \frac{1}{\rho}\left(\rho \sum_{i=1}^{N} h_i \frac{\partial Y_i}{\partial t} + \rho u \sum_{i=1}^{N} h_i \frac{\partial Y_i}{\partial x} + \frac{\partial}{\partial x}\left(\lambda \frac{\partial T}{\partial x}\right) - \sum_{i=1}^{N} J_i \frac{\partial h_i}{\partial x}\right) \tag{4.3}$$

$$\frac{\partial h}{\partial t} = \frac{1}{\rho}\left(- \rho u \frac{\partial h}{\partial x} + \rho \sum_{i=1}^{N} h_i \frac{\partial Y_i}{\partial t} + \rho u \sum_{i=1}^{N} h_i \frac{\partial Y_i}{\partial x} + \frac{\partial}{\partial x}\left(\lambda \frac{\partial T}{\partial x}\right) - \sum_{i=1}^{N} J_i \frac{\partial h_i}{\partial x}\right) \tag{4.4}$$

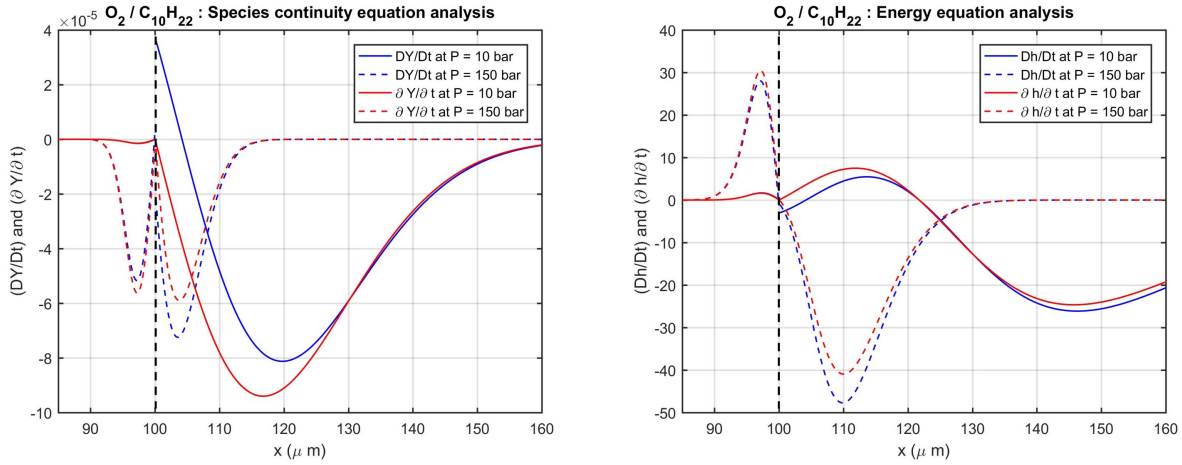

Figure 4.9: Total and local derivatives of the species continuity equation and the energy equation for the oxygen/n-decane mixture.

The species continuity plot shows the equation terms on the left side of the interface related to the n-decane continuity equation and, on the right side of the interface, it shows the terms related to the oxygen continuity equation. It is observed that a sink in mass concentration is generated due to the gradient of diffusion mass fluxes (i.e., gradient in species concentration). This sink travels out of the interface and its magnitude decreases with time. For the case at $p = 150$ bar, sinks are present in both fluid phases, since phase equilibrium conditions dissolve oxygen into the liquid phase. However, at $p = 50$ bar, the sink in n-decane mass fraction is very small because little oxygen has been dissolved into the liquid. The convective terms affect more the low-pressure case, as it would be expected since Figure 4.3 showed that fluid velocities were higher at lower pressures.

When looking at the energy equation, the high-pressure case presents again a sink in energy in the gas phase and a source in energy in the liquid phase, almost not dependent on the convective terms. On the other hand, the low-pressure situation shows a small source of energy in the liquid phase and a traveling source and sink in the gas phase, looking like the sink has been generated first. To look into more detail to try to understand this change in behavior, Figure 4.10 presents the profiles of each term of the energy equation at $t = 100$ μs for the cases at $p = 10$ bar and $p = 150$ bar.

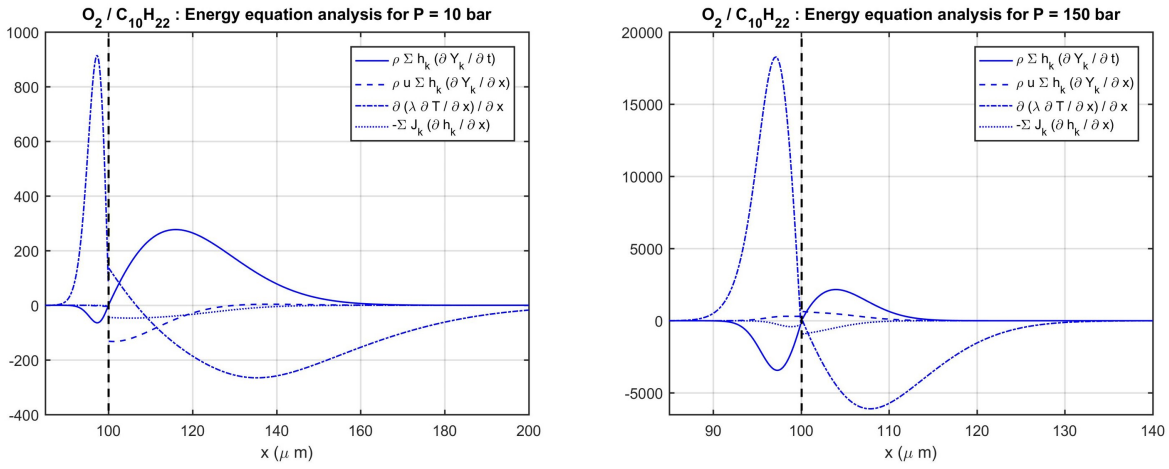

Figure 4.10: Analysis of the terms of the energy equation for the oxygen/n-decane mixture.

For the high-pressure situation, the dominant term driving the energy equation is the heat flux associated to heat conduction. This term overcomes all other terms, clearly defining the energy source and sink observed in Figure 4.9. However, for the case at $p = 10$ bar, the situation becomes more complex in the gas phase. Again in the liquid phase, the heat conductivity becomes dominant over all other terms, generating an energy source. But in the gas phase, this term does not present a clear dominance. When first the liquid and the gas enter in contact, heat conductivity generates a sink in energy traveling to the right of the interface. However, as n-decane is evaporated and mixed with oxygen, this "generation" of n-decane mass fraction or dissolution brings an associated higher enthalpy or energy to the mixture compared to that of the pure oxygen, thus creating a source in energy to our fluid. This source is capable to overcome the sink introduced due to conductivity. In conclusion, thermal conductivity is larger as pressure increases. This is why the wavy shape for $p = 10$ bar is observed in Figure 4.9.

4.2.4 Phase change analysis

An interesting result obtained from the simulations of the oxygen/n-decane mixture is seen in Figure 4.3. As pressure is increased, interface dynamics change from a vaporization to a condensation phenomenon. That is, the velocity behavior is reversed: from liquid flowing into the interface and gas flowing outwards to gas flowing into the interface and liquid exiting it. For the nitrogen/n-octane mixture shown in Appendix F, this behavior is not observed though. However, it is plausible that higher pressures will cause condensation to occur (see Figure F.2).

The effect of this condensation is also observed in Figure 4.6, where the velocity of the interface computed as if the liquid was sitting on a wall is shown. A transition from a reduction to an increase of the liquid phase volume is observed as pressure is increased. For

low pressures, vaporization reduces the volume of liquid. However, as pressure increases the dissolution of lighter species increases the volume of the liquid phase while it still vaporizes. Later, the volume keeps increasing as the condensation phenomenon occurs.

In this scenario, condensation through the increase of pressure is achieved even though we are dealing with a supercritical pressure environment. Mixing of species due to the diffusion process allow this phenomenon to occur. Furthermore, this condensation is achieved while heat is still being conducted from the hotter gas to the colder liquid. For the low pressure cases (10-50 bar), the energy flux summed from heat conduction and energy transport by mass diffusion decreases from the gas to the liquid phase across the interface, thus causing vaporization. However, for higher pressures (100-150 bar), this energy flux increases across the interface and condensation occurs. Although gas enthalpy is always higher than liquid enthalpy at the interface, the internal energy of the liquid phase exceeds the internal energy of the gas phase for high-pressure situations. For the nearly-ideal 10-bar case, gas-mixture internal energy is higher than the liquid-solution internal energy.

At this point, it becomes important to check that basic thermodynamic laws are obeyed to determine if the physical phenomena observed in the simulations can take place. For this, the First Law and the Second Law of thermodynamics are analyzed tracking a fixed mass element containing all diffusion layers. In this system, the enclosed mass remains constant and heat transferred across its boundaries is zero, as well as species diffusion. Then, the integrated First Law becomes

$$\Delta U = W = \int_i^f p(u_{l,-\infty} - u_{g,+\infty})dt \tag{4.5}$$

where the work done on the mass element is computed as the time-integral of pressure, p, times the velocity of each respective boundary, $u_{l,-\infty}$ for the liquid phase and $u_{g,+\infty}$ for the gas phase.

Assuming quasi-static processes, the mass-based First Law can be written as follows, together with the definition of enthalpy $h = u + pv = u + p/\rho$,

$$du = Tds - pdv = dh - pdv - vdp \tag{4.6}$$

where the specific internal energy, u, should not be confused with the velocity of the fluid, which also appears in the work, W, term.

For a constant-pressure process, the previous equation provides a relation for entropy variation of the system,

$$dh = Tds \tag{4.7}$$

Integrating Eq. 4.7, it is obtained that the integrated product of temperature and entropy of the mass element must balance with time, since $\Delta H = Q|_p = 0$ for a constant-pressure process containing all diffusion layers.

$$\Delta H = \int Tds = 0 \tag{4.8}$$

Enthalpy and entropy are computed according to Sections 2.3.2 and 2.3.5 and internal energy is computed using the definition of enthalpy shown in the previous lines as $u = h - p/\rho$. Figure 4.11 provides an analysis of the First Law for the different studied pressures. Integrated results for the mass element are provided per unit area because of the 1-D behavior of the domain. The computed work on the mass element equals the increase of internal energy of the enclosed mass, but small numerical errors may show a slight variation between the computed ΔU and W.

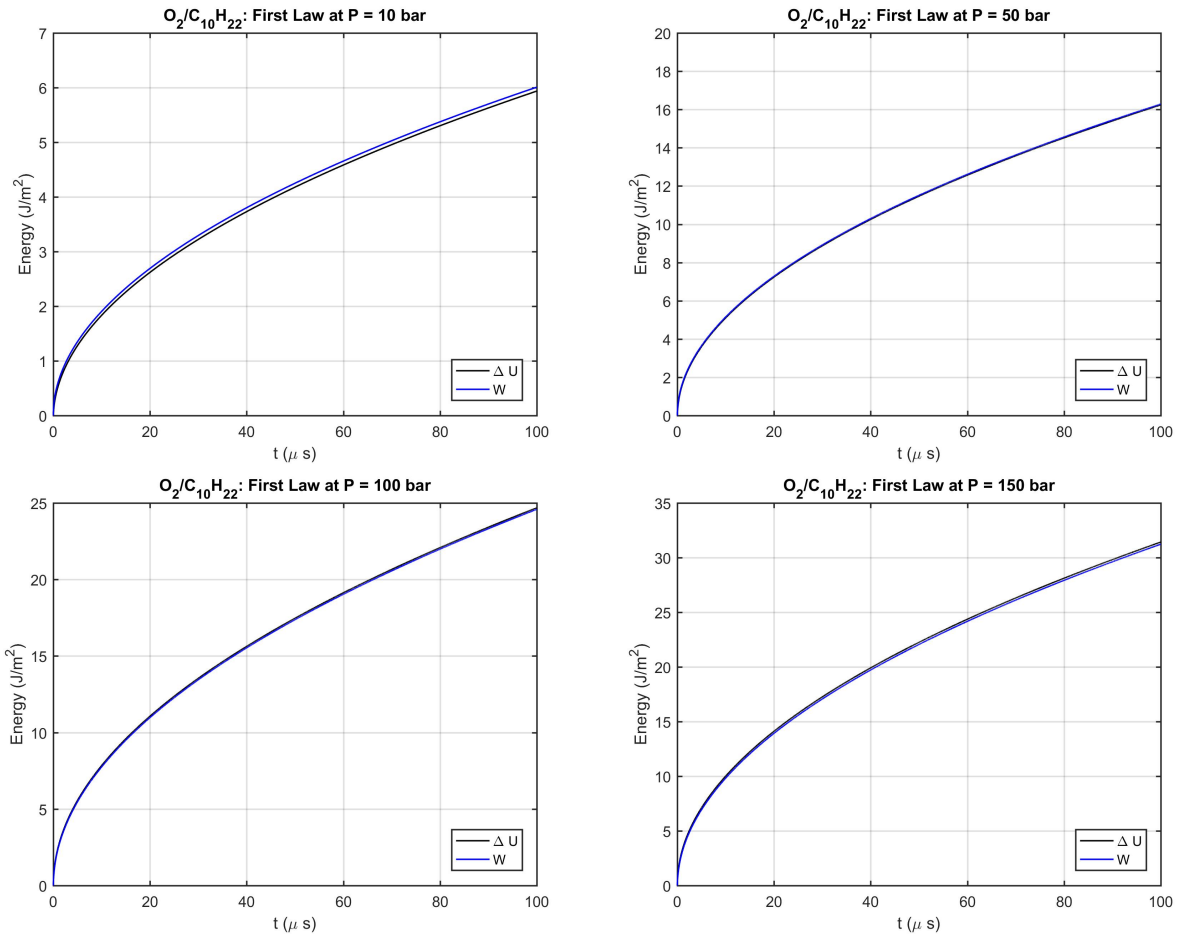

Figure 4.11: First Law results for the oxygen/n-decane mixture at different pressures.

To analyze these numerical errors, a mesh refinement study using the configurations of Table 3.1 shows some expected effects (see Figure 4.12). The first conclusion is that Eq. 4.8 is better satisfied as the mesh is refined, both in Δx and Δt, where the absolute variation of enthalpy tends to zero as it is expected. Then, because of the difficulty of evaluating the integral of Tds in Eq. 4.8, a local evaluation of the error in Eq. 4.7 is computed at each time step at each node and then integrated over the mass element. On one hand, the integrated error decreases with time as the gradients to which the flow field is subjected decrease in magnitude. On the other hand, only refining the mesh in the temporal scale has a significant impact in the reduction of these errors.

Therefore, it is possible to conclude that basic thermodynamic laws are being satisfied in

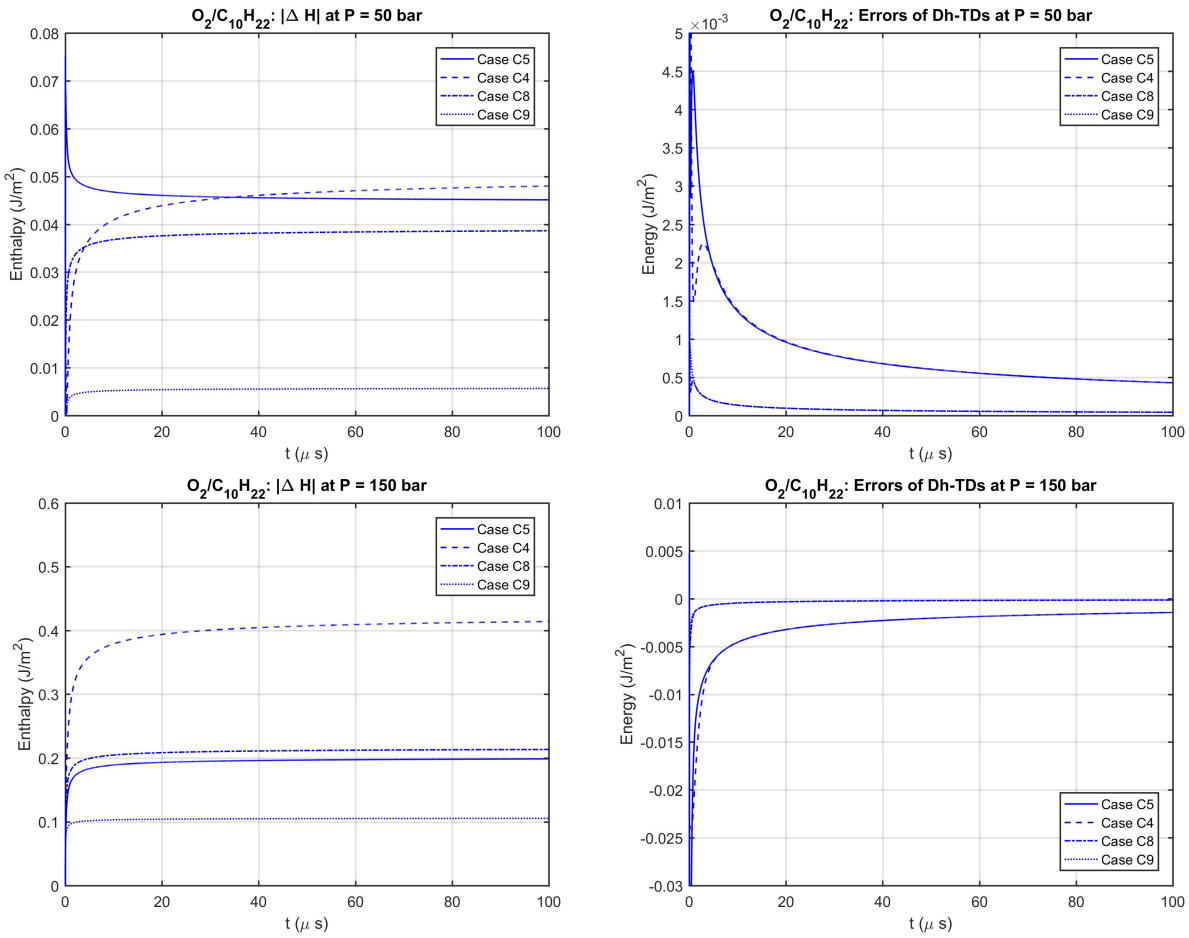

Figure 4.12: Mesh refinement effects on thermodynamic laws for the oxygen/n-decane mixture.

our simulations. It is important to notice that variations in the thermodynamic properties are independent of the selected mass element, as long as it includes all diffusion layers.

To understand better how the First Law and the Second Law are obeyed, the following Figure 4.13 and Figure 4.14 show the temporal evolution of the specific enthalpy and the specific entropy on each side of the interface. In Figure 4.13, the evolution of the specific enthalpy agrees with the results from Eq. 4.8. For 50-150 bar, enthalpy rises in the liquid phase and decreases in the gas phase. Thus, the expected balance to give $\Delta H = 0$ can occur. For the 10-bar case, since enthalpy does not change considerably in the liquid phase, the gas phase presents an enthalpy distribution with a minimum which again allows for Eq. 4.8 to

be satisfied. This distribution is a consequence of the effects of the different terms in the energy equation (see Section 4.2.3), where the diffusion of n-decane into the gas phase acts as a source of energy overcoming the initial sink caused by heat conduction.

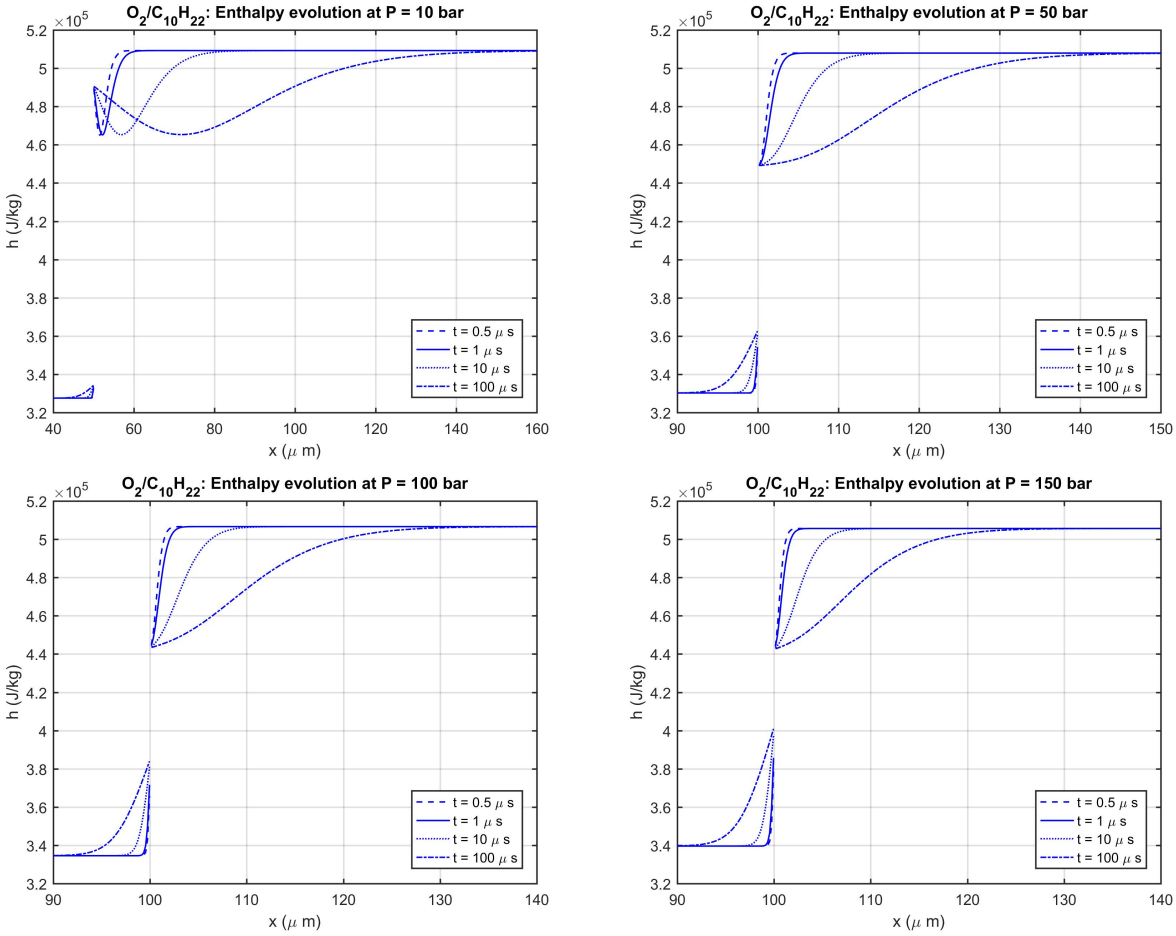

Figure 4.13: Temporal evolution of enthalpy for the oxygen/n-decane mixture at different pressures.

Figure 4.14 shows that specific entropy is increased in the liquid phase and is decreased in the gas phase. However, as the 10-bar case suggests, the integrated variation of entropy in the element of mass is negative: entropy decreases. This is corroborated in Figure 4.15, showing the variation of the integrated entropy for different pressures. This overall decrease in entropy, once integrated accounting for the temperature evolution, must satisfy Eq. 4.8.

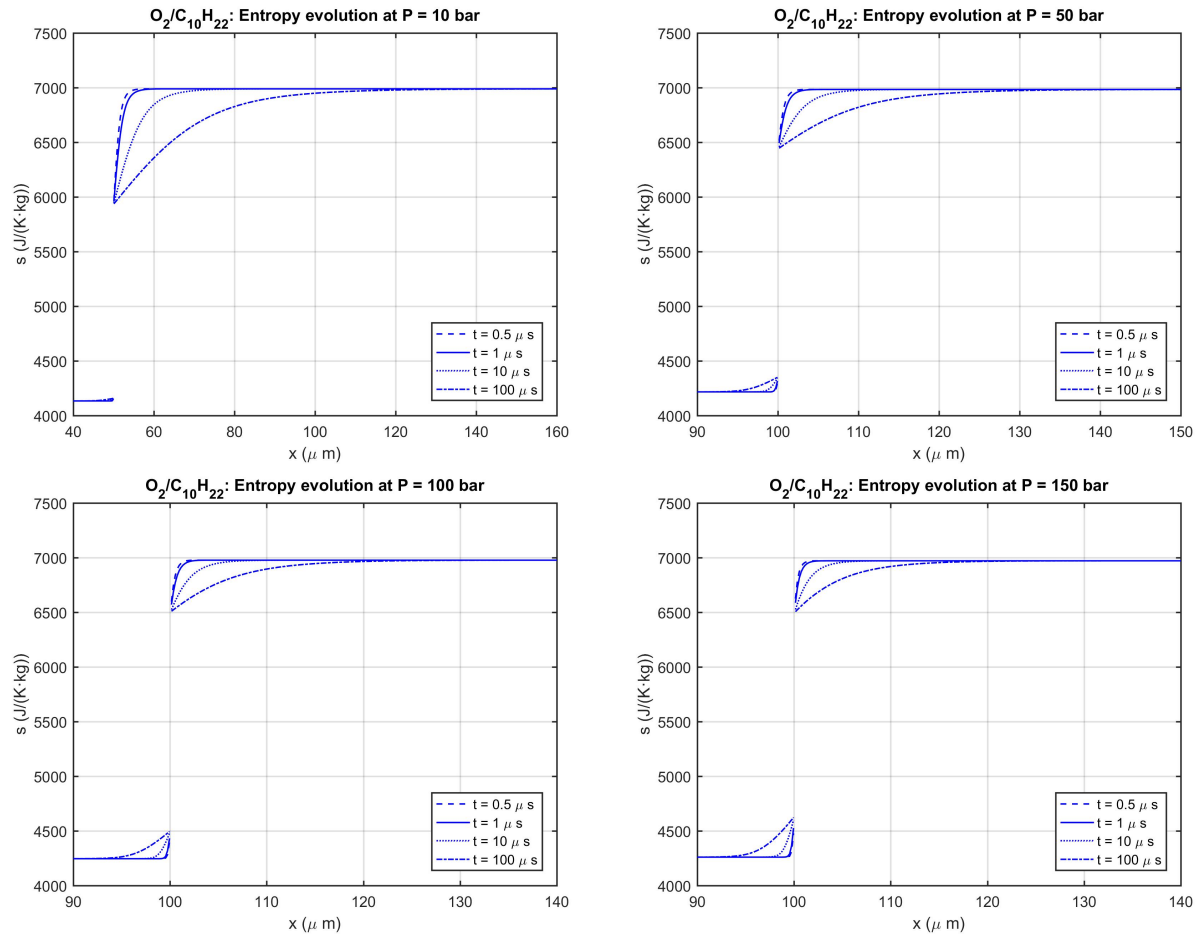

Figure 4.14: Temporal evolution of entropy for the oxygen/n-decane mixture at different pressures.

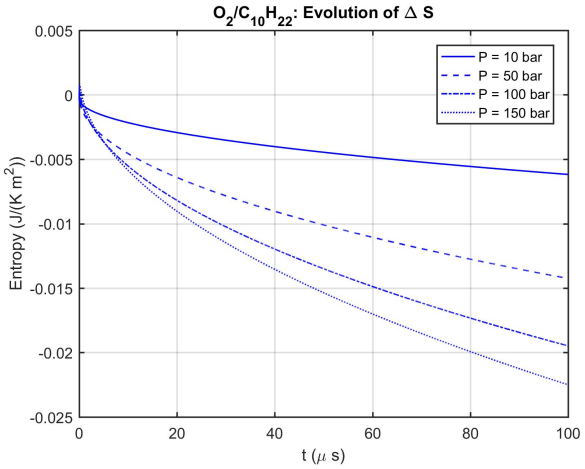

Figure 4.15: Temporal evolution of integrated entropy for the oxygen/n-decane mixture at different pressures.

4.3 Instability analysis: Kelvin-Helmholtz

One of the most common instabilities that generate liquid disruption is the Kelvin-Helmholtz (KH) instability and it is related to the interface behavior between two fluids flowing parallel to each other. Perturbations in the flow will affect the interface and, depending on the wavelength associated to this perturbations, the interface will grow and start curving, yielding to a break up of the liquid stream. An schematic of the problem is seen in Figure 4.16.

The KH instability is usually studied linearizing the equations that govern the interface and fluid behavior. For uniform properties (that is, uniform velocity, density, etc. on each fluid), a discontinuity in velocity appears at the interface, where a vortex sheet is present. The perturbation at the interface can be represented by assuming that its vertical oscillation follows [68],[71],

$$\eta(x,t) = \hat{\eta} e^{ct} e^{ikx} \tag{4.9}$$

where $k = 2\pi/\lambda$ is the wave number. Perturbations in the fluid would follow a similar expression.

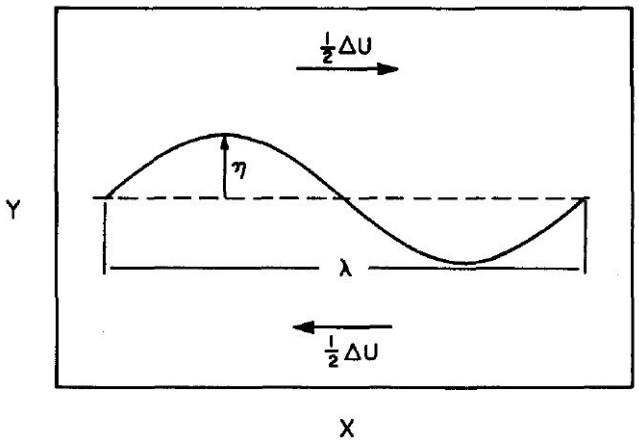

Figure 4.16: Sketch of the Kelvin-Helmholtz instability (source [7]).

From Eq. 4.9, what becomes determinant to identify if the perturbation is stable or unstable is the sign of the real part of the growth rate c. For $c_{\mathrm{R}} < 0$, the perturbation becomes stable; for $c_{\mathrm{R}} = 0$, it is neutral stability; and for $c_{\mathrm{R}} > 0$ it becomes unstable and the perturbation will grow in time. Analyzing the linearized equations and the problem, an expression for c is found to be [71],

$$\begin{aligned} c = &- i\frac{k(\rho_g u_g + \rho_l u_l)}{\rho_g + \rho_l} - k^2\frac{\mu_g + \mu_l}{\rho_g + \rho_l} \pm \left[\frac{\rho_g\rho_l k^2(u_g - u_l)^2}{(\rho_g + \rho_l)^2} - \frac{(\rho_l - \rho_g)gk}{\rho_g + \rho_l}\right. \\ &\left. - \frac{\sigma k^3}{\rho_g + \rho_l} + \frac{k^4(\mu_g + \mu_l)^2}{(\rho_g + \rho_l)^2} + 2ik^3\frac{(\rho_g\mu_l - \rho_l\mu_g)(u_g - u_l)}{(\rho_g + \rho_l)^2}\right]^{1/2} \end{aligned} \tag{4.10}$$

From this expression, it is inferred that viscosity and surface tension will induce stability to the perturbations. In this model, viscous potential flow has been considered. Thus, no vorticity or shear stress exists. Only normal viscous stress is considered. The gravity term will become stable or unstable depending on what fluid is on top. For the dense fluid on top, the term would become unstable. Velocity difference across the interface will always induce instabilities. Here, it is important to remark that the surface-tension term induces stability since we are analyzing a plane interface. For a round liquid jet, surface tension induces instabilities too.

The oxygen/n-decane mixture has been chosen to study this instability and get an estimate of its behavior at $p = 10$ bar and $p = 150$ bar. The properties at the interface are computed from the densities and compositions at $t = 50$ μs using the models explained in Chapter 2. Then, different injection velocities for the liquid are considered (10 and 100 m/s), the gas being at rest (see Table 4.1 for definition of the analyzed cases). Table 4.2 shows the obtained results for the different fluid properties at the interface. It can be observed that as pressure increases, density and viscosity become more similar in both phases and surface tension is reduced.

Table 4.1: Analyzed cases for the Kelvin-Helmholtz instability.

Case	Pressure (bar)	Injection velocity (m/s)
A	10	10
B	10	100
C	150	10
D	150	100

Table 4.2: Fluid properties at the interface.

Oxygen / n-Decane		
Pressure (bar)	10	150
Temperature (K)	451.99	468.53
$X_{g,oxy}$	0.8705	0.9650
$X_{g,dec}$	0.1295	0.0350
$X_{l,oxy}$	0.0259	0.3635
$X_{l,dec}$	0.9741	0.6365
Gas density (kg/m^3)	12.431	133.583
Liquid density (kg/m^3)	503.991	487.599
Surface tension (mN/m)	5.031	1.931
Gas viscosity (kg/(m·s))	1.948×10^{-5}	2.771×10^{-5}
Liquid viscosity (kg/(m·s))	1.001×10^{-4}	5.619×10^{-5}

The results for the analyzed cases are shown in Figure 4.17, Figure 4.18, Figure 4.19 and Figure 4.20. Then, Table 4.3 presents values for the most unstable wavelength, λ, the corresponding growth rate, c_{R}, the characteristic time, τ, for the perturbation to grow by a factor of e, the angular frequency, Ω, and the frequency, f, of the perturbations for each studied case considering viscosity and surface tension.

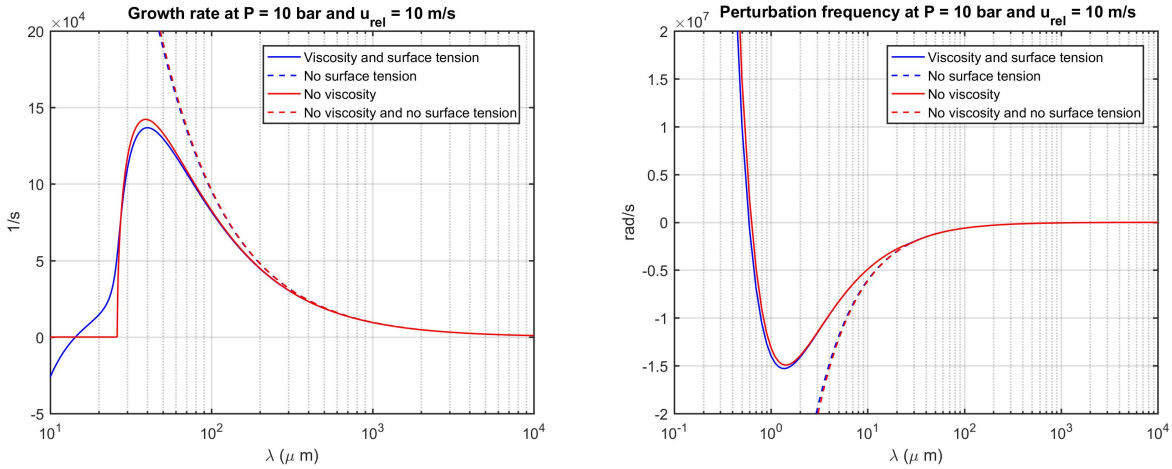

Figure 4.17: Kelvin-Helmholtz instability for oxygen/n-decane mixture at p = 10 bar and injection velocity 10 m/s (Case A).

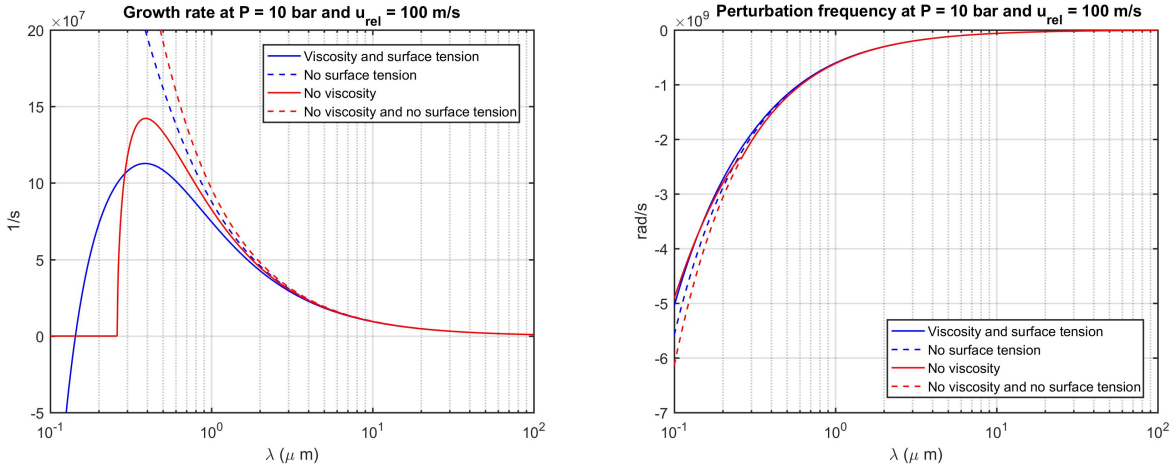

Figure 4.18: Kelvin-Helmholtz instability for oxygen/n-decane mixture at p = 10 bar and injection velocity 100 m/s (Case B).

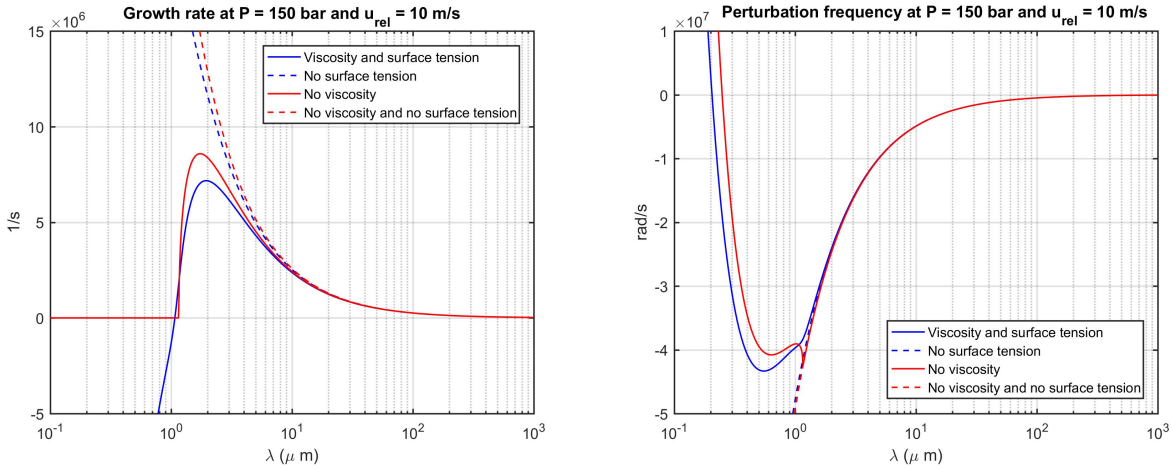

Figure 4.19: Kelvin-Helmholtz instability for oxygen/n-decane mixture at p = 150 bar and injection velocity 10 m/s (Case C).

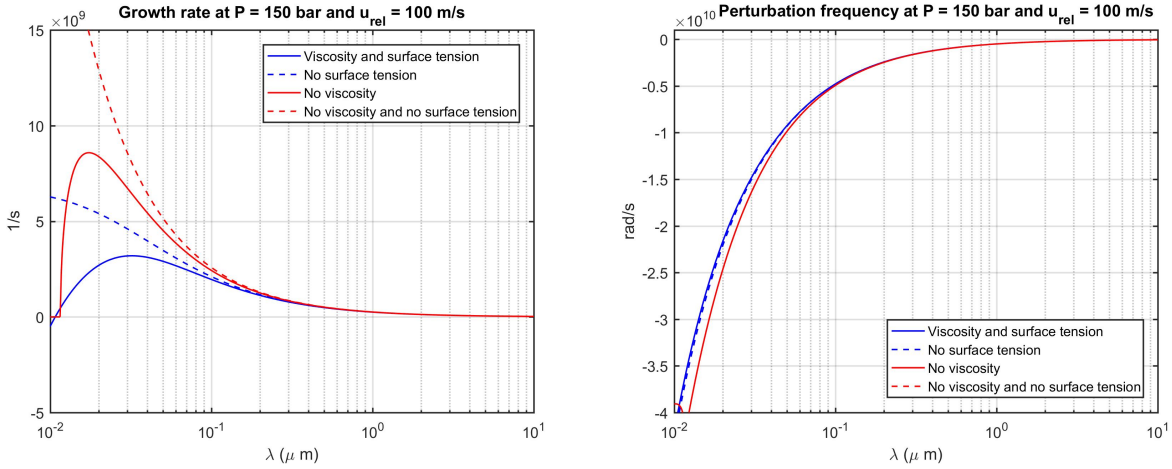

Figure 4.20: Kelvin-Helmholtz instability for oxygen/n-decane mixture at p = 150 bar and injection velocity 100 m/s (Case D).

Table 4.3: Results of Kelvin-Helmholtz instability for the oxygen/n-decane mixture.

Case	λ (μm)	c_R (1/s)	τ (μs)	Ω (rad/s)	f (1/s)
A	40	1.368×10^{5}	7.310	1.524×10^{6}	2.423×10^{5}
B	0.39	1.128×10^{8}	8.865×10^{-3}	1.492×10^{9}	2.375×10^{8}
C	1.95	7.175×10^{6}	0.139	2.469×10^{7}	3.930×10^{6}
D	0.032	3.196×10^{9}	3.129×10^{-4}	1.420×10^{10}	2.260×10^{9}

As seen in the figures, the low-pressure case presents higher wavelengths for the unstable waves than the high-pressure case. This is mainly caused by the reduction in surface tension in our liquid-gas interface. Moreover, increasing the injection velocity shows that viscous damping of the perturbations becomes stronger, displacing the most unstable waves to higher wavelengths.

When analyzing numerical results for the growth rate including viscosity and surface tension (see Table 4.3), it is observed that as pressure and injection velocity are increased, the interface perturbations will grow faster. At the characteristic times of our diffusion process (see Section 4.2), the perturbations would have affected considerably the interface shape, maybe even causing liquid breakup.

These results are not surprising. At typical injection velocities, closer to the 100 m/s case, and high pressures, the liquid will be more affected by the hydrodynamic instabilities, thus causing a faster breakup cascade induced by perturbation wavelengths much smaller than those of low-pressure and/or low injection velocity situations. This result seems to be in accordance with the experimental observations [3] and numerical simulations [2],[4],[12].

However, the wavelengths and the characteristic times that are being discussed in this section may be too small. In reality, and as it is found in simulations, the most unstable waves will tend to have wavelengths between 1-100 μm and the characteristic times that will take the instabilities to grow sufficiently are closer to 20-100 μs [4]. This fact is caused by the assumptions done in the theory being applied in this work.

Recall that fluid properties where assumed to be constant and that a velocity discontinuity at the interface was considered. In reality, a viscous layer will be formed between the two fluids, which will tend to damp the perturbation growth rate and will move the most unstable waves to higher wavelengths. Furthermore, under the considerations of this thesis, a mass diffusion layer will also be present, modifying the whole phenomena. Possibly, characteristic times for the instabilities to grow sufficiently in high-pressure situations will become closer to the characteristic diffusion times observed here. At this stage, presenting reliable results about this issue becomes extremely difficult. Therefore, more realistic simulations are going to be needed.

Chapter 5

Conclusions

5.1 Discussion

This thesis has developed a methodology to compute supercritical pressure fluid behavior by analyzing the existing literature and identifying the main issues to be considered. Density, enthalpy and entropy are computed using a real-gas equation of state in conjunction with ideal gas properties and valid thermodynamic relations. Transport properties, such as viscosity, thermal conductivity and mass diffusion coefficients, have been computed using up-to-date high-density valid correlations and models.

The liquid-gas interface has been treated with matching conditions which include phase equilibrium relations. It has been proven that at pressures higher than the critical pressure of the pure liquid species, two phases exist if the resulting critical pressure of the mixture is higher than the chamber pressure. Therefore, liquid breakup mechanisms are still present in supercritical liquid injection and must be studied to optimize and improve the performance of related engineering applications.

It has been observed that the new phase-equilibrium conditions enhance mixing of species. That is, the gas species are more easily dissolved into the liquid phase. Therefore, characteristic times of this diffusive process have been obtained to estimate where the fluid properties, such as density, vary considerably. It has been seen that, for typical instability development times (20-100 μs), the mass diffusion layer and the thermal diffusion layer present thicknesses of the order of 10 μm in the liquid phase and 30 μm in the gas phase at high pressures. For lower pressures, the liquid solution is almost not affected by diffusion processes, while the gas phase presents a larger diffusion layer thickness.

The Kelvin-Helmholtz instability has been analyzed including surface tension and viscosity, but under the assumptions of constant velocity and density profiles and no shear stress. The results confirm that under high-pressure conditions, where liquid and gas properties become more alike, liquid disruption occurs earlier and affects easily smaller scales. Thus, the liquid breakup will be dominated by aerodynamic forces and will resemble the injection of a gas. However, two main issues arise here: calculations did not include the effects of the formation of a viscous layer between the liquid and the gas and the effects that a diffusion layer around the interface may have on the disruption cascade. Only for high-pressure situations, the liquid phase shows a sufficiently large well-established diffusion layer such that its effects should be studied. On the other hand, the gas phase presents this well-formed diffusion layer in all the studied cases. Therefore, to obtain more reliable results, it is needed to solve the Navier-Stokes equations including all the real-fluid behavior defined in this thesis.

Finally, it has been shown that as pressure increases, a clear vaporization problem can turn into a condensation problem. That is, pressure can act as a liquefying agent, even at supercritial pressures, due to heat and mass transfer associated to species diffusion. To ratify it, the First and Second Law of thermodynamics have been analyzed to prove that no basic physical law is being violated. Studying a fixed-mass element, which includes all diffusion layers, it has been proven that the increase in internal energy is related to the

work done on the boundaries of this mass element. Furthermore, the global variation of enthalpy is zero while entropy decreases, with the relation between these two properties being satisfied. In overall, the effects of this transition from vaporization to condensation translate to a transition of the interface relative movement. That is, the liquid phase will change its behavior and instead of contracting, as it does for low-pressure situations, it will expand.

5.2 Further research

The following points summarize improvements that should be implemented in the methodology and some guidelines for further research in this topic:

- Improve the performance of the SRK-EoS: Correct the density mismatch in the liquid phase and find more information about the binary interaction coefficients. Then, the performance of some transport properties models and phase equilibrium results can be improved.
- Keep track of the available mass diffusion models and see how they can be fitted better with the equation of state and other models used in this methodology.
- Implement multi-component mass diffusion. That is, generate a methodology able to work with mixtures composed by more than two species.
- Implement this methodology to a Navier-Stokes solver to be able to obtain reliable results in actual fluid configurations (e.g., round jet).
- With 2-D and 3-D simulations, analyze the disruption cascade of the liquid jet at supercritical pressures. This is, study the effects of mixing and high-density phenomena in the liquid breakup.

Bibliography

[1] W. Sirignano and C. Mehring, "Review of theory of distortion and desintegration of liquid streams," *Progress in Energy and Combustion Science*, vol. 26, pp. 609–655, 2000.

[2] D. Jarrahbashi, W. Sirignano, P. Popov, and F. Hussain, "Early spray development at high gas density: hole, ligament and bridge formations," *Journal of Fluid Mechanics*, vol. 792, pp. 186–231, 2016.

[3] W. Mayer, A. Schik, B. Vielle, C. Chauveau, I. Gökalp, D. Talley, and R. Woodward, "Atomization and Breakup of Cryogenic Propellants Under High-Pressure Supercritical Conditions," *Journal of Propulsion and Power*, vol. 14, 1998.

[4] A. Zandian, W. Sirignano, and F. Hussain, "Three-dimensional liquid sheet breakup: vorticity dynamics," American Institute of Aeronautics and Astronautics, 2016.

[5] A. Gnanaskandan and J. Bellan, "Numerical simulation of jet injection and species mixing under high-pressure conditions," *Journal of Physics*, vol. 821, 2017.

[6] R. Dahms and J. Oefelein, "On the transition between two-phase and single-phase interface dynamics in multicomponent fluids at supercritical pressures," *Physics of Fluids*, vol. 25, 2013.

[7] R. Rangel and W. Sirignano, "Nonlinear growth of Kelvin-Helmholtz instability: Effect of surface tension and density ratio," *The Physics of Fluids*, vol. 31, pp. 1845–1855, 1988.

[8] J. Sierra-Pallares, J. Valle, P. Garcia-Carrascal, and F. Ruiz, "Numerical study of supercritical and transcritical injection using different turbulent Prandtl numbers: A second law analysis," *The Journal of Supercritical Fluids*, vol. 115, pp. 86–98, 2016.

[9] R. Dahms and J. Oefelein, "Liquid jet breakup regimes at supercritical pressures," *Combustion and Flame*, vol. 162, pp. 3648–3657, 2015.

[10] V. Yang, "Modeling of supercritical vaporization, mixing, and combustion processes in liquid-fueled propulsion systems," *Proceedings of the Combustion Institute*, vol. 28, pp. 925–942, 2000.

[11] W. Sirignano, *Fluid Dynamics and Transport of Droplets and Sprays*. Cambridge University Press, 2nd ed., 2010.

[12] D. Jarrahbashi and W. Sirignano, "Vorticity dynamics for transient high-pressure liquid injection," *Physics of Fluids*, vol. 26, 2014.

[13] J. Bellan, "Supercritical (and subcritical) fluid behavior and modeling: drops, streams, shear and mixing layers, jets and sprays," *Progress in Energy and Combustion Science*, vol. 26, pp. 329–366, 2000.

[14] E. Masi, J. Bellan, K. Harstad, and N. Okong'o, "Multi-species turbulent mixing under supercritical-pressure conditions: modeling, direct numerical simulation and analysis revealing species spinodal decomposition," *Journal of Fluid Mechanics*, vol. 721, pp. 578–626, 2013.

[15] G. Borghesi and J. Bellan, "Models for the large eddy simulation equations to describe multi-species mixing occuring at supercritical pressure," *International Journal of Energetic Materials and Chemical Propulsion*, vol. 13, pp. 434–453, 2014.

[16] G. Borghesi and J. Bellan, "A priori and a posteriori investigations for developing large eddy simulations of multi-species turbulent mixing under high-pressure conditions," *Physics of Fluids*, vol. 27, 2015.

[17] A. Gnanaskandan and J. Bellan, "Large eddy simulations of high pressure jets: Effect of subgrid scale modeling," American Institute of Aeronautics and Astronautics, 2017.

[18] X. Chen, D. Ma, V. Yang, and S. Popinet, "High-fidelity simulations of impinging jet atomization," *Atomization and sprays*, vol. 23, no. 12, pp. 1079–1101, 2013.

[19] X. Chen and V. Yang, "Thickness-based adaptive mesh refinement methods for multi-phase flow simulations with thin regions," *Journal of Computational Physics*, vol. 269, pp. 22–39, 2014.

[20] S. Mak, C. Sung, X. Wang, S. Yeh, Y. Chang, V. Joseph, V. Yang, and C. Wu, "An efficient surrogate model for emulation and physics extraction of large eddy simulations," *Journal of the Acoustical Society of America*, 2017.

[21] H. Huo and V. Yang, "Large-Eddy Simulation of Supercritical Combustion: Model Validation Against Gaseous H2-O2 Injector," *Journal of Propulsion and Power*, vol. 33, no. 5, pp. 1272–1284, 2017.

[22] R. Dahms and J. Oefelein, "Non-equilibrium gas-liquid interface dynamics in high-pressure liquid injection systems," *Proceedings of the Combustion Institute*, vol. 35, pp. 1587–1594, 2015.

[23] H. Ping and G. A.F., "A sharp interface method for coupling multiphase flow, heat transfer and multicomponent mass transfer with interphase diffusion," *Journal of Computational Physics*, vol. 332, pp. 316–332, 2017.

[24] H. Ping, A. Raghavan, and A. Ghoniem, "Impact of non-ideality on mixing of hydrocarbons and water at supercritical or near-critical conditions," *The Journal of Supercritical Fluids*, vol. 102, pp. 50–65, 2015.

[25] A. Raghavan and A. Ghoniem, "Simulation of supercritical water-hydrocarbon mixing in a cylindrical tee at intermediate reynolds number: Formulation, numerical method and laminar mixing," *The Journal of Supercritical Fluids*, vol. 92, pp. 31–46, 2014.

[26] G. Wu, S. Dabiri, M. Timko, and A. Ghoniem, "Fractionation of multi-component hydrocarbon droplets in water at supercritical or near-critical conditions," *The Journal of Supercritical Fluids*, vol. 72, pp. 150–160, 2012.

[27] B. Chehroudi, D. Talley, and E. Coy, "Visual characteristics and initial growth rates of round cryogenic jets at subcritical and supercritical pressures," *Physics of Fluids*, vol. 14, no. 2, pp. 850–861, 2002.

[28] B. Chehroudi, R. Cohn, and D. Talley, "Cryogenic shear layers: experiments and phenomenological modeling of the initial growth rate under subcritical and supercritical conditions," *International Journal of Heat and Fluid Flow*, vol. 23, pp. 554–563, 2002.

[29] M. Oschwald, J. Smith, R. Branam, J. Hussong, A. Schik, B. Chehroudi, and D. Talley, "Injection of fluid into supercritical environments," *Combustion Science and Technology*, vol. 178, pp. 49–100, 2006.

[30] I. Leyva, B. Chehroudi, and D. Talley, "Dark core analysis of coaxial injectors at sub-, near-, and supercritical pressures in a transverse acoustic field," 43rd AIAA-ASME-SAE-ASEE Joint Propulsion Conference and Exhibit, 2007.

[31] J. Manin, M. Bardi, L. Pickett, R. Dahms, and J. Oefelein, "Microscopic investigation of the atomization and mixing processes of diesel sprays injected into high pressure and temperature environments," *Fuel*, vol. 134, pp. 531–543, 2014.

[32] M. Benedict, G. Webb, and L. Rubin, "An empirical equation for thermodynamic properties of light hydrocarbons and their mixtures I. Methane, ethane, propane and n-butane," *The Journal of Chemical Physics*, vol. 8, pp. 334–345, 1940.

[33] M. Benedict, G. Webb, and L. Rubin, "An empirical equation for thermodynamic properties of light hydrocarbons and their mixtures II. Mixtures of methane, ethane, propane and n-butane," *The Journal of Chemical Physics*, vol. 10, pp. 747–758, 1942.

[34] A. Yang, K. Kuo, and W. Hsieh, "Supercritical evaporation and combustion of liquid oxygen in an axisymmetric configuration," *Progress in Astronautics and Aeronautics*, vol. 80, 1996.

[35] J. Oefelein and V. Yang, "Analysis of hydrogen-oxygen mixing and combustion processes at high-pressures," Aerospace Sciences Meeting, Reno, NV, American Institute of Aeronautics and Astronautics, 1997.

[36] K. Harstad and J. Bellan, "Mixing rules for multicomponent mixture mass diffusion coefficients and thermal diffusion factors," *The Journal of Chemical Physics*, vol. 120, pp. 5664–5673, 2004.

[37] K. Harstad and J. Bellan, "High-Pressure Binary Mass Diffusion Coefficients for Combustion Applications," *Industrial and Engineering Chemistry Research*, vol. 43, pp. 645–654, 2004.

[38] F. White, *Viscous Fluid Flow*. Mc Graw Hill Education, 3rd ed., 2011.

[39] H. Callen, *Thermodynamics and an Introduction to Thermostatistics*. Wiley, 2nd ed., 2005.

[40] O. Redlich and J. Kwong, "On the thermodynamics of solutions. V. An equation of state. Fugacities of gaseous solutions," *Chemical Reviews*, 1949.

[41] G. Soave, "Equilibrium constants from a modified Redlich-Kwong equation of state," *Chemical Engineering Science*, vol. 27, pp. 1197–1203, 1972.

[42] H. Huo, X. Wan, and V. Yang, "A general study of counterflow diffusion flames at subcritical and supercritical conditions: Oxygen/hydrogen mixtures," *Combustion and flame*, vol. 161, pp. 3040–3050, 2014.

[43] A. Jorda Juanos, P. Popov, and W. Sirignano, "Counterflow analysis for combustion at high pressure," American Institute of Aeronautics and Astronautics, 2016.

[44] M. Graboski and T. Daubert, "A modified Soave equation of state for phase equilibrium calculations. 1. Hydrocarbon systems," *Industrial and Engineering Chemistry Process Design and Development*, vol. 17, no. 4, pp. 443–448, 1978.

[45] G. Recktenwald, *Numerical Methods with MATLAB. Implementation and Application*. Prentice-Hall, 1st ed., 2000.

[46] D. Peng and D. Robinson, "A new two-constant equation of state," *Industrial and Engineering Chemistry Fundamentals*, vol. 15, pp. 59–64, 1976.

[47] A. Leahy-Dios and A. Firoozabadi, "Unified Model for Nonideal Multicomponent Molecular Diffusion Coefficients," *American Institute of Chemical Engineers*, vol. 53, no. 11, pp. 2932–2939, 2007.

[48] M. Graboski and T. Daubert, "A modified Soave equation of state for phase equilibrium calculations. 2. Systems containing CO2, H2S, N2 and CO," *Industrial and Engineering Chemistry Process Design and Development*, vol. 17, no. 4, pp. 448–454, 1978.

[49] M. Graboski and T. Daubert, "A modified Soave equation of state for phase equilibrium calculations. 3. Systems containing hydrogen," *Industrial and Engineering Chemistry Process Design and Development*, vol. 18, no. 2, pp. 300–306, 1979.

[50] C. Twu, J. Coon, A. Harvey, and J. Cunningham, "An approach for the application of a cubic equation of state to hydrogen-hydrocarbon systems," *Industrial and Engineering Chemistry Research*, vol. 35, pp. 905–910, 1996.

[51] G. Soave, S. Gamba, and L. Pellegrini, "SRK equation of state: Predicting binary interaction parameters of hydrocarbons and related compounds," *Fluid Phase Equilibria*, vol. 299, pp. 285–293, 2010.

[52] B. Poling, J. Prausnitz, and J. O'Connell, *The Properties of Gases and Liquids*. Mc Graw Hill, 5th ed., 2004.

[53] C. Passut and R. Danner, "Correlation of Ideal Gas Enthalpy, Heat Capacity and Entropy," *Industrial and Engineering Chemistry Process Design and Development*, vol. 11, no. 4, pp. 543–546, 1972.

[54] S. Turns, *An Introduction to Combustion: Concepts and Applications*. Mc Graw Hill, 3rd ed., 2012.

[55] A. Jorda Juanos and W. Sirignano, "Thermodynamic Analysis for Combustion at High Gas Densities," 25th International Colloquium on the Dynamics of Explosions and Reactive Systems, 2015.

[56] J. H. Zembal, "Comparison of several two-parameter cubic equations of state for calculating vapor-liquid equilibria of mixtures," Master's thesis, University of California Irvine.

[57] J. Wambui-Mutoru and A. Firoozabadi, "Form of the multicomponent Fickian diffusion coefficients matrix," *Journal of Chemical Thermodynamics*, vol. 43, pp. 1192–1203, 2011.

[58] M. Riazi and C. Whitson, "Estimating Diffusion Coefficients of Dense Fluids," *Industrial and Engineering Chemistry Research*, vol. 32, pp. 3081–3088, 1993.

[59] H. Liu, C. Silva, and E. Macedo, "New Equations for Tracer Diffusion Coefficients of Solutes in Supercritical and Liquid Solvents Based on the Lennard-Jones Fluid Model," *Industrial and Engineering Chemistry Research*, vol. 36, pp. 246–252, 1997.

[60] J. Wesselingh and R. Krishna, *Mass Transfer*. E. Horwood, 1990.

[61] T. Chung, M. Ajlan, L. Lee, and K. Starling, "Generalized Multiparameter Correlation for Nonpolar and Polar Fluid Transport Properties," *Industrial and Engineering Chemistry Research*, vol. 27, pp. 671–679, 1988.

[62] J. Ely and J. Hanley, "Prediction of Transport Properties. 1. Viscosity of Fluids and Mixtures," *Industrial and Engineering Chemistry Fundamentals*, vol. 20, pp. 323–332, 1981.

[63] J. Ely and J. Hanley, "Prediction of Transport Properties. 2. Thermal Conductivity of Pure Fluids and Mixtures," *Industrial and Engineering Chemistry Fundamentals*, vol. 22, pp. 90–97, 1983.

[64] S. Takahashi, "Preparation of a generalized chart for the diffusion coefficients of gases at high pressures," *Journal of Chemical Engineering of Japan*, vol. 7, no. 6, pp. 417–420, 1974.

[65] C. Yaws, *Yaws' Critical Property Data for Chemical Engineers and Chemists*. Knovel, 2012.

[66] H. Versteeg and W. Malalasekra, *An Introduction to Computational Fluid Dynamics*. Pearson Education Limited, 2nd ed., 2007.

[67] C. Gerald, *Applied Numerical Analysis*. Addison-Wesley, 2nd ed., 1978.

[68] P. Kundu, I. Cohen, and D. Dowling, *Fluid Mechanics*. Elsevier, 5th ed., 2012.

[69] R. Courant, K. Friedrichs, and H. Lewy, "Über die partiellen Differenzengleichungen der mathematischen Physik," *Mathematische Annalen*, vol. 100, pp. 32–74, 1928.

[70] E. Simons, *An efficient multi-domain approach to large eddy simulation of incompressible turbulent flows in complex geometries*. PhD thesis, Von Karman Institute for Fluid Dynamics, October 2000.

[71] D. Joseph, T. Funada, and J. Wang, *Potential Flows of Viscous and Viscoelastic Liquids*. Cambridge University Press, 2007.

Appendix A

Physical Properties

Table A.1: Physical properties of different species obtained from REFPROP, NIST.

Species	MW (kg/mol)	T_c (K)	P_c (MPa)	ρ_c (kg/m^3)	ω
Oxygen	0.031999	154.58	5.043	436.14	0.0222
Nitrogen	0.028013	126.19	3.3958	313.3	0.0372
Carbon dioxide	0.04401	304.13	7.3773	467.6	0.22394
Methane	0.016043	190.56	4.5992	162.66	0.01142
Propane	0.044096	369.89	4.2512	220.48	0.1521
n-Octane	0.11423	569.32	2.497	234.9	0.395
n-Decane	0.14228	617.7	2.103	233.34	0.4884
n-Dodecane	0.17033	658.10	1.817	226.55	0.574

Appendix B

SRK-EoS Derivatives

This appendix includes the needed partial derivatives of different terms associated to the Soave-Redlich-Kwong equation of state,

$$p = \frac{R_u T}{v - b} - \frac{a(T)}{v(v + b)} \tag{B.1}$$

or in the cubic form in terms of the compressibility factor, Z,

$$Z^3 - Z^2 + (A - B - B^2)Z - AB = 0 \tag{B.2}$$

When using this EoS to compute different fluid properties (e.g., enthalpy), the following derivatives appear and must be computed in terms of the parameters of the SRK-EoS.

$$\left.\frac{\partial \ln \Phi_i}{\partial T}\right|_{p,X_i} = \left.\frac{1}{\Phi_i}\frac{\partial \Phi_i}{\partial T}\right|_{p,X_i} = \left(1-\frac{b_i}{b}Z\right)\frac{1}{T} + \frac{A}{B}\left[\frac{1}{T} - \frac{1}{a}\left.\frac{\partial a}{\partial T}\right|_{p,X_i}\right]\left[2\left(\frac{a_i}{a}\right)^{0.5} - \frac{b_i}{b}\right]\ln\left(1+\frac{B}{Z}\right) + \frac{A}{B}\left(\frac{a_i}{a}\right)^{0.5}\left[\frac{1}{a}\left.\frac{\partial a}{\partial T}\right|_{p,X_i} - \frac{1}{a_i}\frac{da_i}{dT}\right]\ln\left(1+\frac{B}{Z}\right) + \left[\frac{b_i}{b} - \frac{1}{Z-B}\right]\frac{Z}{v}\left.\frac{\partial v}{\partial T}\right|_{p,X_i} + \frac{A}{B+Z}\left[2\left(\frac{a_i}{a}\right)^{0.5} - \frac{b_i}{b}\right]\frac{1}{v}\left.\frac{\partial v}{\partial T}\right|_{p,X_i} \tag{B.3}$$

$$\left.\frac{\partial \ln \Phi_i}{\partial X_j}\right|_{p,T,X_{i\neq j}} = \left.\frac{1}{\Phi_i}\frac{\partial \Phi_i}{\partial X_j}\right|_{p,T,X_{i\neq j}} = \frac{B}{Z-B}\frac{b_j}{b} + \frac{A}{Z+B}\frac{b_i b_j}{b^2} - \frac{2A}{Z+B}\left(\frac{a_i}{a}\right)^{0.5}\frac{b_j}{b} - \frac{b_i b_j}{b^2}(Z-1) + \left[\frac{b_i}{b}\left(Z-\frac{A}{Z+B}\right) - \frac{Z}{Z-B} + \frac{2A}{Z+B}\left(\frac{a_i}{a}\right)^{0.5}\right]\frac{1}{v}\left.\frac{\partial v}{\partial X_j}\right|_{p,T,X_{i\neq j}} + \frac{2A}{B}\left[\left(\frac{a_i}{a}\right)^{0.5} - \frac{b_i}{b}\right]\left[\frac{b_j}{b} - \frac{\sum_{i=1}^{N} X_i (a_i a_j)^{0.5}(1-k_{ij})}{a}\right]\ln\left(\frac{Z+B}{Z}\right) \tag{B.4}$$

$$\left.\frac{\partial v}{\partial X_i}\right|_{p,T,X_{j\neq i}} = \frac{R_u T}{p}\left(\frac{2(B-Z)(A/a)\sum_{j=1}^{N}[X_j(a_i a_j)^{0.5}(1-k_{ij})] + (Z+2BZ+A)Bb_i/b}{3Z^2-2Z+A-B-B^2}\right) \tag{B.5}$$

$$\left.\frac{\partial v}{\partial T}\right|_{p,X_i} = \frac{R_u T}{p}\left(\frac{Z}{T} + \frac{(B-Z)[(A/a)(\partial a/\partial T)_{p,X_i} - 2A/T] - (B/T)[Z+2BZ+A]}{3Z^2-2Z+A-B-B^2}\right) \tag{B.6}$$

$$\left.\frac{\partial a}{\partial T}\right|_{p,X_i} = \frac{1}{2}\sum_{i=1}^{N}\sum_{j=1}^{N} X_i X_j\left[\left(\frac{a_i}{a_j}\right)^{0.5}\frac{da_j}{dT} + \left(\frac{a_j}{a_i}\right)^{0.5}\frac{da_i}{dT}\right](1-k_{ij}) \tag{B.7}$$

$$\left.\frac{\partial^2 a}{\partial X_i \partial T}\right|_{p,X_{j\neq i}} = \sum_{i=1}^{N} X_i \left[\left(\frac{a_i}{a_j}\right)^{0.5} \frac{da_j}{dT} + \left(\frac{a_j}{a_i}\right)^{0.5} \frac{da_i}{dT}\right](1-k_{ij}) \tag{B.8}$$

$$\left.\frac{\partial a}{\partial X_j}\right|_{p,T,X_{i\neq j}} = 2\sum_{i=1}^{N} X_i (a_i a_j)^{0.5}(1-k_{ij}) \tag{B.9}$$

$$\frac{da_i}{dT} = \frac{a_i}{\alpha_i}\frac{d\alpha_i}{dT} \tag{B.10}$$

$$\left.\frac{\partial b}{\partial X_i}\right|_{p,T,X_{j\neq i}} = b_i \tag{B.11}$$

Appendix C

Development of the Energy Equation

This appendix shows the development of the energy equation used in this work (Eq. 2.8 and Eq. 2.9) starting from a more general version of the 1-D enthalpy conservation equation, Eq. C.1. The only reasonable assumption taken in this equation is expressing the heat flux using Fourier's law.

$$\frac{\partial}{\partial t}(\rho h) + \frac{\partial}{\partial x}(\rho u h) = \frac{\partial}{\partial x}\left(\lambda \frac{\partial T}{\partial x}\right) - \sum_{i=1}^{N} \frac{\partial}{\partial x}(J_i h_i) + \frac{DP}{Dt} + \tau_{ij}\frac{\partial u}{\partial x} \tag{C.1}$$

Expanding out the RHS of Eq. C.1 and applying continuity equation (Eq. 2.1), we get

$$\frac{\partial}{\partial t}(\rho h) + \frac{\partial}{\partial x}(\rho u h) = \rho \frac{\partial h}{\partial t} + \rho u \frac{\partial h}{\partial x} + h\left[\frac{\partial \rho}{\partial t} + \frac{\partial}{\partial x}(\rho u)\right] = \rho \frac{\partial h}{\partial t} + \rho u \frac{\partial h}{\partial x} \tag{C.2}$$

The term $\sum_{i=1}^{N} \frac{\partial}{\partial x}(J_i h_i)$ can also be expanded as

$$\sum_{i=1}^{N} \frac{\partial}{\partial x}(J_i h_i) = \sum_{i=1}^{N} J_i \frac{\partial h_i}{\partial x} + \sum_{i=1}^{N} h_i \frac{\partial J_i}{\partial x} \tag{C.3}$$

and applying species continuity (Eq. 2.4), it becomes

$$\sum_{i=1}^{N} \frac{\partial}{\partial x}(J_i h_i) = \sum_{i=1}^{N} J_i \frac{\partial h_i}{\partial x} + \sum_{i=1}^{N} h_i \Big[- \rho \frac{\partial Y_i}{\partial t} - \rho u \frac{\partial Y_i}{\partial x} \Big] \tag{C.4}$$

Substituting Eq. C.2 and Eq. C.4 into Eq. C.1, we get

$$\rho \frac{\partial h}{\partial t} + \rho u \frac{\partial h}{\partial x} = \frac{\partial}{\partial x}\left(\lambda \frac{\partial T}{\partial x}\right) - \sum_{i=1}^{N} J_i \frac{\partial h_i}{\partial x} - \sum_{i=1}^{N} h_i \Big[- \rho \frac{\partial Y_i}{\partial t} - \rho u \frac{\partial Y_i}{\partial x} \Big] + \frac{DP}{Dt} + \tau_{ij} \frac{\partial u}{\partial x} \tag{C.5}$$

Assuming the hypothesis of this work, viscous dissipation and pressure variations are neglected. Then, we recover the energy equations Eq. 2.8 and Eq. 2.9.

$$\rho \frac{\partial h}{\partial t} + \rho u \frac{\partial h}{\partial x} = \frac{\partial}{\partial x}\left(\lambda \frac{\partial T}{\partial x}\right) - \sum_{i=1}^{N} J_i \frac{\partial h_i}{\partial x} + \sum_{i=1}^{N} h_i \Big[\rho \frac{\partial Y_i}{\partial t} + \rho u \frac{\partial Y_i}{\partial x} \Big] \tag{C.6}$$

$$\rho \frac{\partial h}{\partial t} + \rho u \frac{\partial h}{\partial x} - \rho \sum_{i=1}^{N} h_i \frac{\partial Y_i}{\partial t} - \rho u \sum_{i=1}^{N} h_i \frac{\partial Y_i}{\partial x} - \frac{\partial}{\partial x}\left(\lambda \frac{\partial T}{\partial x}\right) + \sum_{i=1}^{N} J_i \frac{\partial h_i}{\partial x} = 0 \tag{C.7}$$

The energy equation could also be developed in terms of temperature, but in this work solving for the conservation equation of enthalpy has been chosen to be the best option, finding the temperature afterwards by applying a root-finding algorithm to the enthalpy equation Eq. 2.33.

Appendix D

Fluid Properties Models

Ideal gas enthalpy

The model used to compute the ideal gas enthalpy is that of Passut and Danner [53]. This work presents a reliable correlation to compute the ideal gas enthalpy, heat capacity at constant pressure and entropy for a wide range of temperatures.

The ideal gas enthalpy is correlated as

$$h^* = A + BT + CT^2 + DT^3 + ET^4 + FT^5 \tag{D.1}$$

where A, B, C, D, E and F are the coefficients that fit the correlation to experimental data, providing the enthalpy in btu/lb and using temperature in ^{o}R.

Their correlation can also be used to compute the ideal gas heat capacity at constant pressure, C_p^*, and the ideal gas entropy, s^*, as

$$C_p^* = B + 2CT + 3DT^2 + 4ET^4 + 5FT^4 \tag{D.2}$$

$$s^* = B \ln T + 2CT + \frac{3}{2}DT^2 + \frac{4}{3}ET^3 + \frac{5}{4}FT^4 + G \tag{D.3}$$

where C_p is given in btu/(lb·°R) and s^* is also given in btu/(lb·°R).

To convert from temperature in Kelvin degrees (K) to temperature in Rankine degrees (°R), the following conversion is used,

$$T[^\circ\mathrm{R}] = \frac{9}{5} \cdot T[\mathrm{K}] \tag{D.4}$$

To convert from enthalpy in btu/lb to J/kg, the following conversion is used,

$$h^*[\mathrm{J/kg}] = 2326.0 \cdot h^*[\mathrm{btu/lb}] \tag{D.5}$$

Similar conversions can be established for C_p^* and s^*.

The data bases are 0 btu/lb at 0 °R for the enthalpy and 0 btu/(lb·°R) at 0 °R at 1 atm pressure for the entropy. Recall that entropy must satisfy $s^* = 0$ at $T = 0$.

The following Table D.1 and Table D.2 provide some values for the constants to be used in this correlation for different species used in this work.

Table D.1: Correlation constants for Passut and Danner ideal gas model (a) (source [53]).

Species	**A**	**B**	**C** (10^3)
Oxygen	-0.98176	0.227486	-0.037305
Nitrogen	-0.68925	0.253664	-0.014549
Carbon dioxide	4.77805	0.114433	0.101132
Methane	-5.58114	0.564834	-0.282973
Propane	-1.22301	0.179733	0.066458
n-Octane	29.50114	-0.022402	0.459712
n-Decane	28.48990	-0.023837	0.461164
n-Dodecane	26.21126	-0.018522	0.453893

Table D.2: Correlation constants for Passut and Danner ideal gas model (b) (source [53]).

Species	**D** (10^6)	**E** (10^{10})	**F** (10^{14})	**G**
Oxygen	0.048302	-0.185243	0.247488	0.124314
Nitrogen	0.012544	-0.017106	-0.008239	0.050052
Carbon dioxide	-0.026494	0.034706	-0.013140	0.343357
Methane	0.417399	-1.525576	1.958857	-0.623373
Propane	0.250998	-1.247461	1.893509	0.178189
n-Octane	-0.098062	0.104754	-0.031355	0.664632
n-Decane	-0.099786	0.108353	-0.033074	0.611062
n-Dodecane	-0.096464	0.101393	-0.029665	0.542807

Viscosity and thermal conductivity

The correlations from Chung et al. [61] have been used to obtain the values of viscosity and thermal conductivity of our mixture.

The model first computes the dilute gas viscosity, η_0, and the thermal conductivity, λ_0, using the Chapman-Enskog theory.

The dilute gas viscosity becomes

$$\eta_0 = (4.0785 \times 10^{-5}) \frac{(MT)^{0.5}}{V_c^{2/3} \Omega^*} F_c \tag{D.6}$$

where η_0 is given in P (Poise), M is the molecular weight in g/mol, T is the temperature

in K and V_c is the critical volume in cm^3/mol. The parameter Ω^* is the reduced collision integral, computed as

$$\Omega^* = \frac{A}{\hat{T}^B} + \frac{C}{\exp(D\hat{T})} + \frac{E}{\exp(F\hat{T})} + G\hat{T}^B \sin(S\hat{T}^W - H) \tag{D.7}$$

In Eq. D.7, the dimensionless temperature, $\hat{T}$, is related to the potential energy parameter, ϵ, and the Boltzmann's constant, k, by the equation

$$\hat{T} = \frac{T}{\epsilon/k} \tag{D.8}$$

where ϵ/k is found to be

$$\epsilon/k = T_c/1.2593 \tag{D.9}$$

being T_c the critical temperature in K.

The constants from Eq. D.7 are $A = 1.16145$, $B = 0.14874$, $C = 0.52487$, $D = 0.77320$, $E = 2.16178$, $F = 2.43787$, $G = -6.435 \times 10^{-4}$, $H = 7.27371$, $S = 18.0323$ and $W = -0.76830$.

The factor F_c is found to be

$$F_c = 1 - 0.2756\omega + 0.059035\mu_r^4 + \kappa \tag{D.10}$$

where ω is the acentric factor, κ is a correction factor related to the hydrogen-bonding effect and μ_r is a dimensionless dipole moment. The last two parameters appear when dealing

with polar fluids.

The dimensionless dipole moment, if needed, can be computed as

$$\mu_r = 131.3\mu/(V_c T_c)^{1/2} \tag{D.11}$$

where μ is the dipole moment of the fluid.

Finally, the dilute gas thermal conductivity can be found from the dilute gas viscosity as seen in Eq. D.12, where λ_0 is given in cal/(cm·s·K).

$$\lambda_0 = 7.452(\eta_0/M)\Psi \tag{D.12}$$

$$\Psi = 1 + \alpha\left(\frac{0.215 + 0.28288\alpha - 1.061\beta + 0.26665Z}{0.6366 + \beta Z + 1.061\alpha\beta}\right) \tag{D.13}$$

In Eq. D.13, $\alpha = C_v/R - 3/2$, being C_v the ideal gas heat capacity at constant volume in cal/(mol·K) and R the universal gas constant $R = 1.987$ cal/(mol·K). Moreover, $\beta = 0.7862 - 0.7109\omega + 1.3168\omega^2$ and $Z = 2.0 + 10.5T_r^2$, with T_r being the reduced temperature $T_r = T/T_c$.

The heat capacity at constant volume, C_v, can be computed from Passut and Danner correlations too [53], knowing that $R = C_p - C_v$.

After dilute gas properties have been obtained, the next step is to obtain the viscosity for dense fluids (in P again) by applying

$$\eta = \eta_\kappa + \eta_p \tag{D.14}$$

where the following identities apply,

$$\eta_\kappa = \eta_0 \left(\frac{1}{G_2} + A_6 Y \right) \tag{D.15}$$

$$\eta_p = \left(36.344 \times 10^{-6} \frac{(MT_c)^{0.5}}{V_c^{2/3}} \right) \exp \left(A_8 + \frac{A_9}{\hat{T}} + \frac{A_{10}}{\hat{T}^2} \right) \tag{D.16}$$

being $Y = \rho V_c/6$ and $G_1 = (1.0 - 0.5Y)/(1 - Y)^3$. Moreover,

$$G_2 = \frac{A_1[1 - \exp(-A_4 Y)]/Y + A_2 G_1 \exp(A_5 Y) + A_3 G_1}{A_1 A_4 + A_2 + A_3} \tag{D.17}$$

The coefficients A_i are given by $A_i = a_0(i) + a_1(i)\omega + a_2(i)\mu_r^4 + a_3(i)\kappa$. The values for $a_0(i)$, $a_1(i)$, $a_2(i)$ and $a_3(i)$ are found in Table D.3.

Similarly, the thermal conductivity for a dense fluid (in cal/(cm·s·K)) is obtained as,

$$\lambda = \lambda_\kappa + \lambda_p \tag{D.18}$$

where the following identities apply,

$$\lambda_\kappa = \lambda_0 \left(\frac{1}{H_2} + B_6 Y \right) \tag{D.19}$$

$$\lambda_p = \left(3.039 \times 10^{-4} \frac{(T_c/M)^{0.5}}{V_c^{2/3}} \right) B_7 Y^2 H_2 T_r^{0.5} \tag{D.20}$$

$$H_2 = \frac{B_1[1-\exp(-B_4 Y)]/Y + B_2 G_1 \exp(B_5 Y) + B_3 G_1}{B_1 B_4 + B_2 + B_3} \tag{D.21}$$

The coefficients B_i are given by $B_i = b_0(i) + b_1(i)\omega + b_2(i)\mu_r^4 + b_3(i)\kappa$. The values for $b_0(i)$, $b_1(i)$, $b_2(i)$ and $b_3(i)$ are found in Table D.4.

Table D.3: Coefficients for Chung et al. model (a) (source [61]).

i	$a_0(i)$	$a_1(i)$	$a_2(i)$	$a_3(i)$
1	6.32402	50.41190	-51.68010	1189.02000
2	0.12101×10^{-2}	-0.11536×10^{-2}	-0.62571×10^{-2}	0.37283×10^{-1}
3	5.28346	254.20900	-168.48100	3898.27000
4	6.62263	38.09570	-8.46414	31.41780
5	19.74540	7.63034	-14.35440	31.52670
6	-1.89992	-12.53670	4.98529	-18.15070
7	24.27450	3.44945	-11.29130	69.34660
8	0.79716	1.11764	0.12348×10^{-1}	-4.11661
9	-0.23816	0.67695×10^{-1}	-0.81630	4.02528
10	0.68629×10^{-1}	0.34793	0.59256	-0.72663

Table D.4: Coefficients for Chung et al. model (b) (source [61]).

i	$b_0(i)$	$b_1(i)$	$b_2(i)$	$b_3(i)$
1	2.41657	0.74824	-0.91858	121.72100
2	-0.50924	-1.50936	-49.99120	69.98340
3	6.61069	5.62073	64.75990	27.03890
4	14.54250	-8.91387	-5.63794	74.34350
5	0.79274	0.82019	-0.69369	6.31734
6	-5.86340	12.80050	9.58926	-65.52920
7	81.17100	114.15800	-60.84100	466.77500

Finally, mixture rules have to be implemented to apply this model to mixtures. The following rules are used to compute mixture parameters,

$$\sigma_m^3 = \sum_{i=1}^{N}\sum_{j=1}^{N} X_i X_j \sigma_{ij}^3 \tag{D.22}$$

$$\epsilon_m/k = \frac{\sum_{i=1}^{N}\sum_{j=1}^{N} X_i X_j (\epsilon_{ij}/k)\sigma_{ij}^3}{\sigma_m^3} \tag{D.23}$$

$$V_{cm} = (\sigma_m/0.809)^3 \tag{D.24}$$

$$T_{cm} = 1.2593(\epsilon_m/k) \tag{D.25}$$

$$\omega_m = \frac{\sum_{i=1}^{N}\sum_{j=1}^{N} X_i X_j \omega_{ij}\sigma_{ij}^3}{\sigma_m^3} \tag{D.26}$$

$$M_m = \left(\frac{\sum_{i=1}^{N}\sum_{j=1}^{N} X_i X_j (\epsilon_{ij}/k)\sigma_{ij}^2 M_{ij}^{0.5}}{(\epsilon_m/k)\sigma_m^2}\right)^2 \tag{D.27}$$

$$\mu_m^4 = \frac{\sum_{i=1}^{N}\sum_{j=1}^{N} X_i X_j (\mu_i^2\mu_j^2)}{(\epsilon_{ij}/k)\sigma_{ij}^3}\sigma_m^3(\epsilon_m/k) \tag{D.28}$$

$$\kappa_m = \sum_{i=1}^{N}\sum_{j=1}^{N} X_i X_j \kappa_{ij} \tag{D.29}$$

$$\mu_{rm} = 131.3\mu_m/(V_{cm}T_{cm})^{0.5} \tag{D.30}$$

The binary parameters are given by

$$\sigma_{ij} = \xi_{ij}(\sigma_i\sigma_j)^{0.5} \tag{D.31}$$

$$\epsilon_{ij}/k = \zeta_{ij}[(\epsilon_i/k)(\epsilon_j/k)]^{0.5} \tag{D.32}$$

$$\omega_{ij} = 0.5(\omega_i + \omega_j) \tag{D.33}$$

$$M_{ij} = 2M_iM_j/(M_i + M_j) \tag{D.34}$$

$$\kappa_{ij} = (\kappa_i\kappa_j)^{0.5} \tag{D.35}$$

where ξ_{ij} and ζ_{ij} are binary interaction parameters taken to be unity for most systems or when no other information is provided.

To obtain the viscosity and the thermal conductivity in SI units, the following conversions must be applied,

$$\eta[\text{kg}/(\text{m}\cdot\text{s})] = \frac{1}{10}\eta[P] \tag{D.36}$$

$$\lambda[\mathrm{J/(m{\cdot}s{\cdot}K)}] = \lambda[\mathrm{W/(m{\cdot}K)}] = 418.4 \cdot \lambda[\mathrm{cal/(cm{\cdot}s{\cdot}K)}] \tag{D.37}$$

Diffusion coefficients

The model from Leahy-Dios and Firoozabadi [47] has been used to compute the diffusion coefficients required for the evaluation of the mass diffusion fluxes. This model combines a correlation obtained using an extensive data bank to evaluate the infinite-dilution diffusion coefficients with the Vignes relation (Eq. D.38) to obtain the binary diffusion coefficients. Then, these coefficients can be applied in the Maxwell-Stefan relations (Eq. 2.50).

$$D_{12} = (D_{12}^{\infty})^{X_2} (D_{21}^{\infty})^{X_1} \tag{D.38}$$

The infinite-dilution diffusion coefficients are evaluated with the following correlation, given that component 2 is infinitely diluted in component 1,

$$\frac{cD_{21}^{\infty}}{(cD)^0} = A_0 \left(\frac{T_{r,1} P_{r,2}}{T_{r,2} P_{r,1}} \right)^{A_1} \left(\frac{\mu}{\mu^0} \right)^{[A_2(\omega_1,\omega_2)+A_3(P_r,T_r)]} \tag{D.39}$$

where the constants A_i are given by

$$A_0 = \exp(a_1) \tag{D.40}$$

$$A_1 = 10 a_2 \tag{D.41}$$

$$A_2 = a_3(1 + 10\omega_1 - \omega_2 + 10\omega_1\omega_2) \tag{D.42}$$

$$A_3 = a_4(P_{r,1}^{3a_5} - 6P_{r,2}^{a_5} + 6T_{r,1}^{10a_6}) + a_7 T_{r,2}^{-a_6} + a_2\left(\frac{T_{r,1}P_{r,2}}{T_{r,2}P_{r,1}}\right) \tag{D.43}$$

with $a_1 = -0.0472$, $a_2 = 0.0103$, $a_3 = -0.0147$, $a_4 = -0.0053$, $a_5 = -0.3370$, $a_6 = -0.1852$ and $a_7 = -0.1914$.

In Eq. D.39, c is the molar density in mol/m^3, μ is the viscosity in Pa·s or kg/(m·s), ω_i is the acentric factor of component i, $T_{r,i} = T/T_{c,i}$ is the reduced temperature of component i and $P_{r,i} = P/P_{c,i}$ is the reduced pressure of component i. Moreover, $(cD)^0$ is the dilute gas density-diffusion coefficient product in mol/(m·s) and μ^0 is the dilute gas viscosity or low-pressure viscosity in Pa·s or kg/(m·s).

The dense-fluid viscosity, μ, can be obtained from the correlations by Chung et al., but the proposed methods by Leahy-Dios and Firoozabadi to obtain $(cD)^0$ and μ^0 are applied here.

To compute $(cD)^0$, the Fuller et al. approach is used [52] (Eq. D.44).

$$(cD)^0 = 1.01 \times 10^{-2} T^{0.75} \frac{\left(\frac{1}{M_1} + \frac{1}{M_2}\right)^{0.5}}{R\left[(\sum \nu_1)^{1/3} + (\sum \nu_2)^{1/3}\right]^2} \tag{D.44}$$

In the previous equation, $(cD)^0$ is given in mol/(m·s), M_1 and M_2 are the molecular weights of each component in g/mol, T is the temperature in K and $\sum \nu_i$ is the diffusion volume of component i. From Poling et al. [52], Table D.5 shows typical diffusion volume increments for each atom in the molecule and some diffusion volumes for simple molecules.

Table D.5: Diffusion volumes obtained from Poling et al. (source [52]).

Component	**Diffusion volume**	**Component**	**Diffusion volume**
C	15.9	O	6.11
N	4.54	H	2.31
O_2	16.3	N_2	18.5
CO_2	26.9	H_2	6.12

The low-pressure viscosity is computed according to Stiel and Thodos correlation as

$$\mu^0 = \frac{\mu_1^0 M_1^{0.5} + \mu_2^0 M_2^{0.5}}{M_1^{0.5} + M_2^{0.5}} \tag{D.45}$$

where μ_i^0 is computed as follows, for $T_{r,i} < 1.5$,

$$\mu_i^0 \xi_i = 34 \times 10^{-8} (T_{r,i})^{0.94} \tag{D.46}$$

or as follows, for $T_{r,i} > 1.5$,

$$\mu_i^0 \xi_i = 17.78 \times 10^{-8} (4.58 T_{r,i} - 1.67)^{5/8} \tag{D.47}$$

The following expression is used to compute ξ_i,

$$\xi_i = \frac{T_{c,i}^{1/6}}{M_i^{1/2} (0.987 \times 10^{-5} P_{c,i})^{2/3}} \tag{D.48}$$

Surface tension

To compute the surface tension, it has been used the Macleod-Sugden correlation as suggested by Poling et al. [52]. The model is explained in Section 2.3.8, but this appendix provides

information on how to compute the parachor for each component of our mixture.

The empirical method consists in adding structural contributions accounting for each atom forming the molecule and the type of bonding between them. Table D.6 shows some of the values taken for each type of contribution.

Table D.6: Parachor contributions obtained from Poling et al. (source [52]).

Element	**Contribution**	**Element**	**Contribution**
C	9.0	O	20.0
N	17.5	H	15.5
Double bond	19.1	Triple bond	40.6
Single bond	0.0	Semipolar bond	0.0

For instance, to compute the parachor of the molecule of n-decane, $C_{10}H_{22}$, it would be found to be $P = 10 \cdot 9.0 + 22 \cdot 15.5 = 431$.

Appendix E

Validation of the Models

This appendix intends to justify the selected equation of state and fluid properties models by comparing the results obtained with them with other works or references. The REFPROP program from NIST is used here as one of the main references to compare with, since the results they provide are based on an extended experimental data set and high-fidelity equations of state or models. Usually, it is expected that it will provide better results than those obtained with the models of this thesis. However, as discussed in the report, working with cubic equations of state and correlations for the fluid properties represents a significant competitive advantage when code implementation is considered.

Figure E.1 presents a comparison of the density obtained using the SRK-EoS and the density that the REFPROP program provides for oxygen and decane. The testing is done for a low-pressure case and for a high-pressure case. Similarly, Figure E.2 shows the same kind of results but for different mixtures of oxygen and decane. In overall, it is seen that the SRK-EoS predicts accurate results for a wide range of fluid states, but it is also shown that one of its weaknesses becomes the obtainment of the liquid density, which seems to become more critical as pressure is increased and affecting more the heavier species. This fact will affect all the other fluid properties models which depend on density as a main correlation

parameter. Nevertheless, it still is accurate enough for our purposes.

When computing results for enthalpy, a better agreement is observed with the results provided by REFPROP (see Figure E.3). This fact shows how robust is the procedure of computing the enthalpy using the departure function concept with the SRK-EoS.

Recall that the cubic behavior of the SRK-EoS can predict metastable solutions which do not represent the saturation pressure of the P-v diagram. REFPROP results give an idea of where the saturation conditions lie. Our code is consistent with this issue: where only liquid or gas should be present, the solution defining that state is taken.

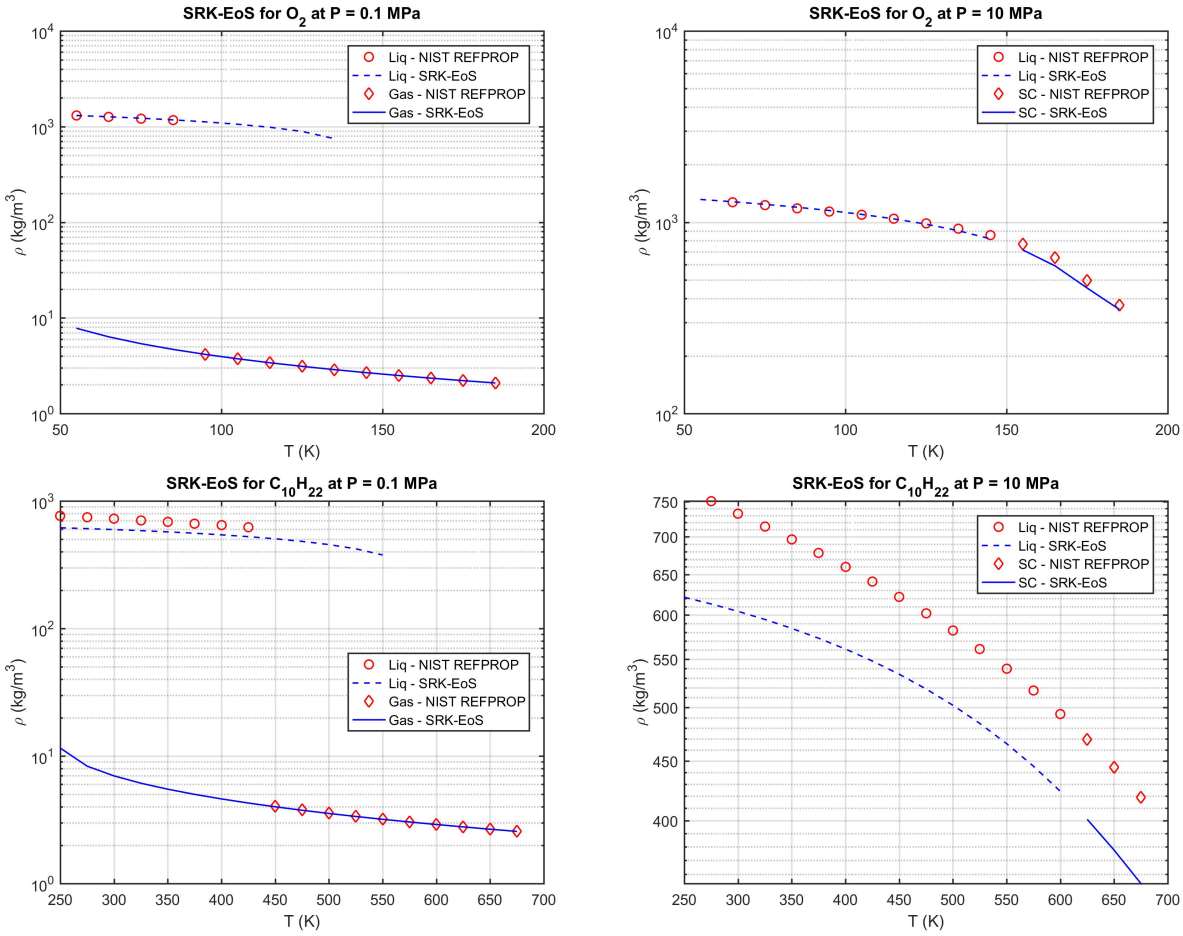

Figure E.1: Comparison of density results obtained with SRK-EoS and REFPROP (a).

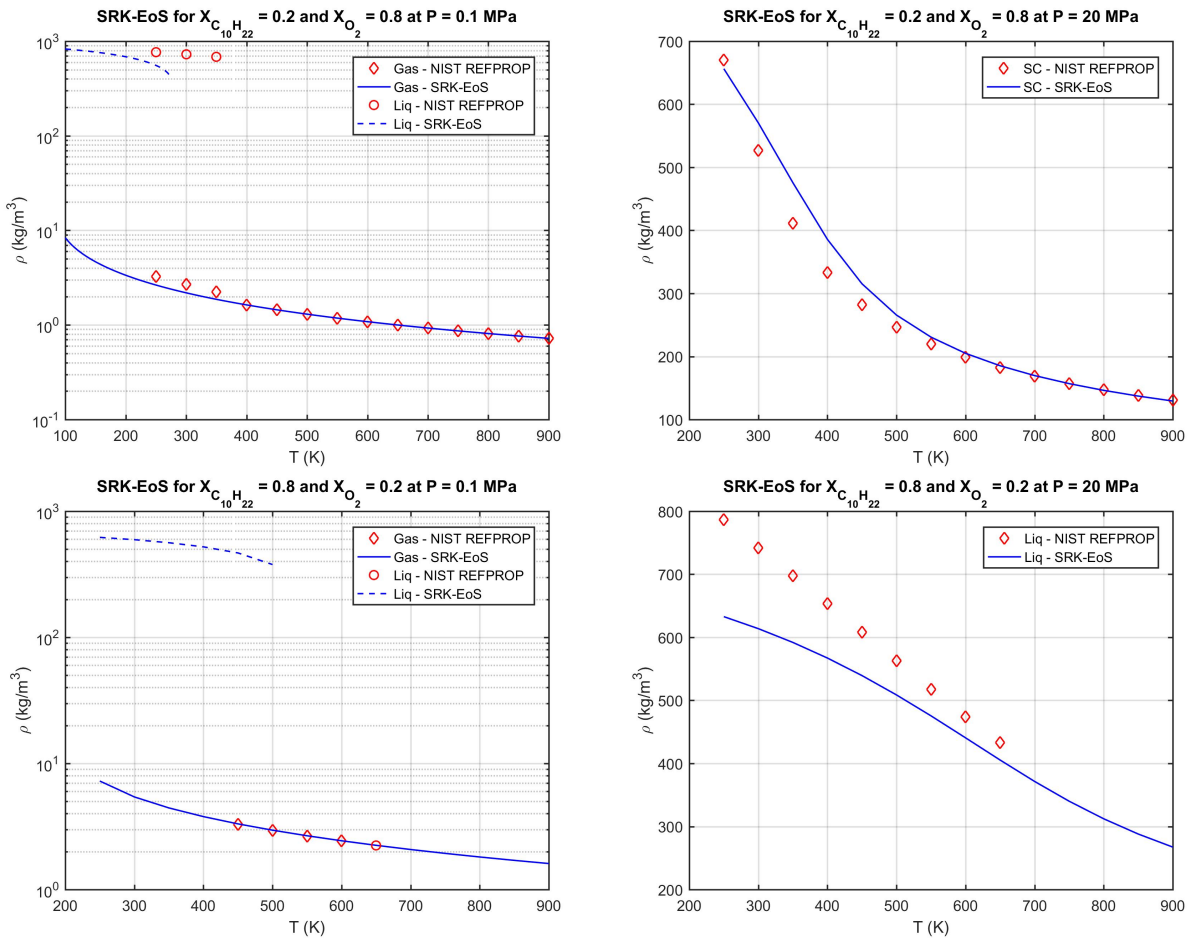

Figure E.2: Comparison of density results obtained with SRK-EoS and REFPROP (b).

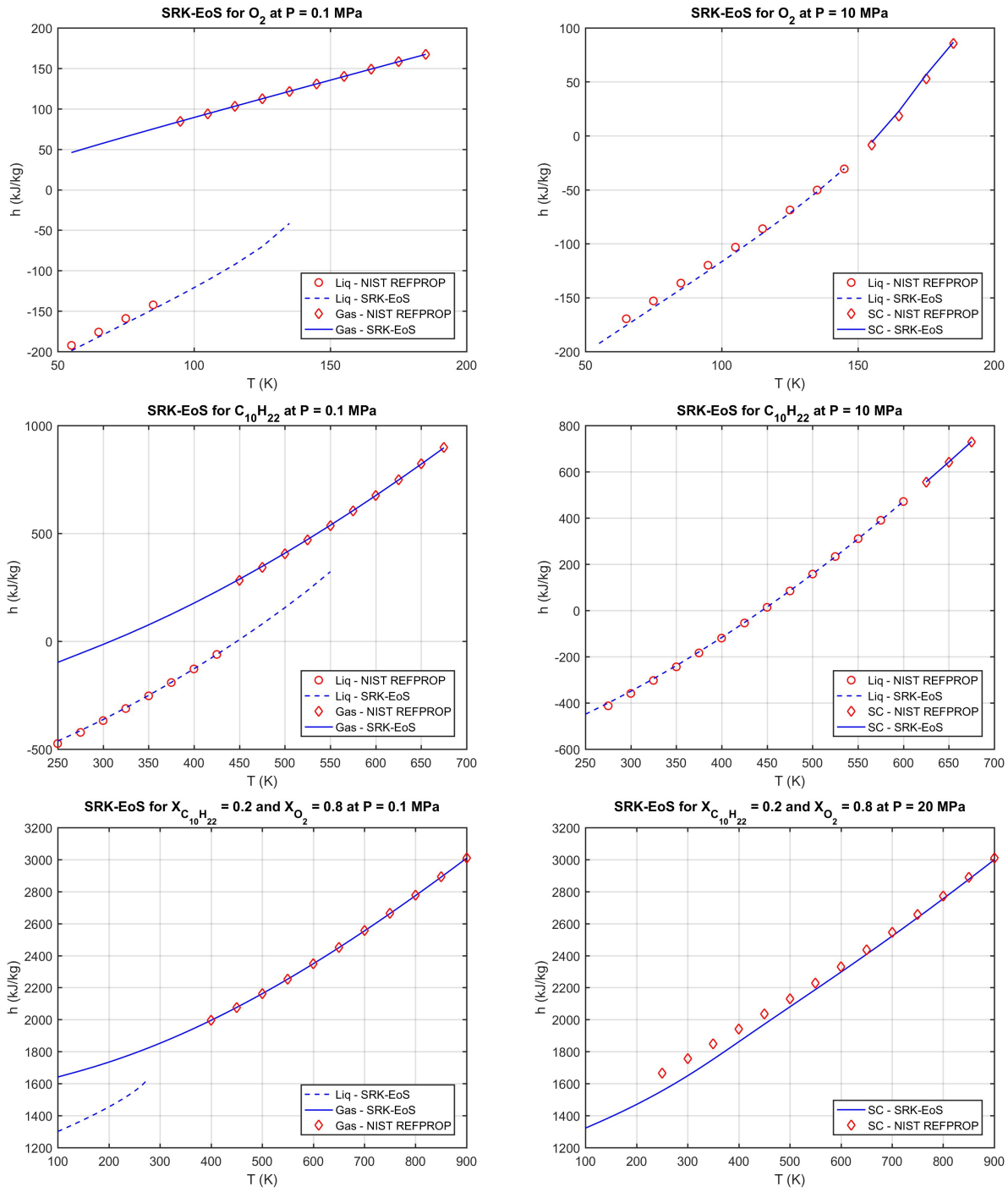

Figure E.3: Comparison of enthalpy results obtained with SRK-EoS and REFPROP.

Another feature of the SRK-EoS to be compared with other references is the phase equilibrium results. For the same test mixture, oxygen and decane, the results provided with SRK-EoS are compared with those given by REFPROP and those provided by Jorda-Juanos and Sirignano [55], who used the RK-EoS. In this case, important differences are obtained between the SRK-EoS and REFPROP, especially close to the critical point of the mixture (see Figure E.4). Thus, the implementation of binary interaction coefficients is strongly encouraged, when available, since better results may be obtained. For other mixtures, the results matched better. Therefore, it could be possible that REFPROP is giving some kind of error for the oxygen/decane mixture.

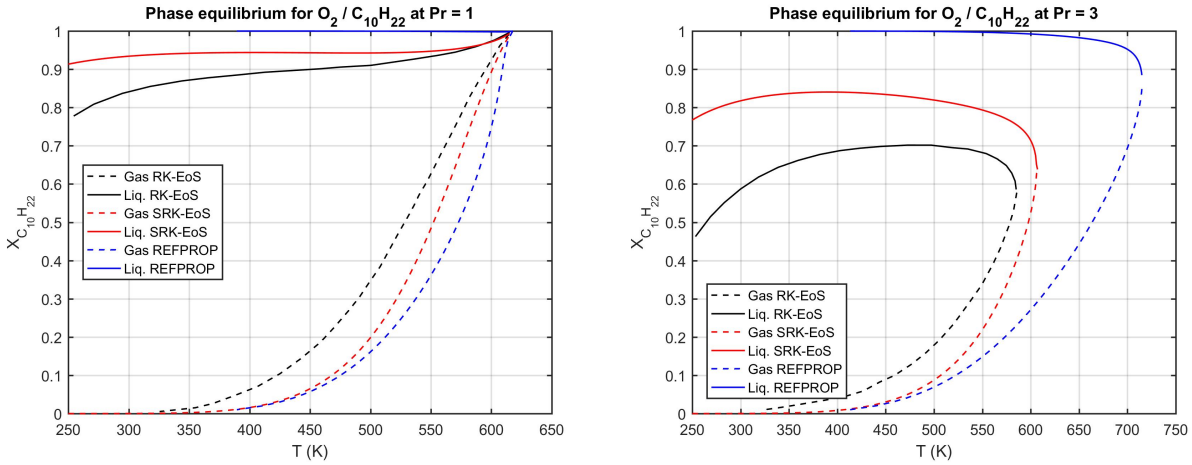

Figure E.4: Comparison of phase equilibrium results obtained with SRK-EoS, RK-EoS and REFPROP.

Viscosity and thermal conductivity are computed using Chung et al. model [61]. The following Figure E.5 and Figure E.6 show the results obtained with this model, compared with results from the paper itself and REFPROP. It is seen that the model provides reasonably accurate results, but its strong dependence in density may induce some deviations when computing these properties for the liquid phase. That is, density inaccuracy in the liquid phase due to the SRK-EoS will affect the performance of this model for computing the viscosity and thermal conductivity.

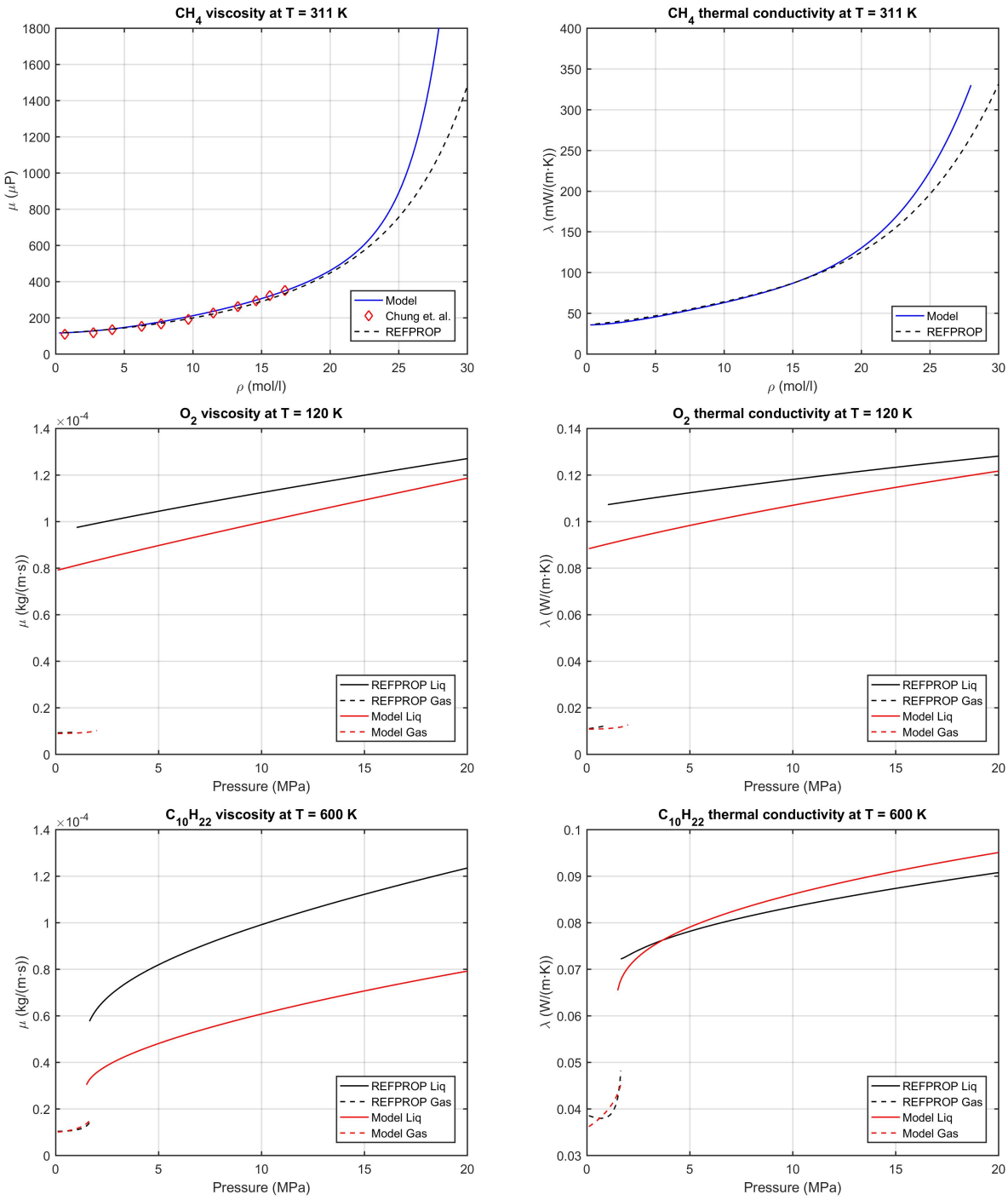

Figure E.5: Comparison of viscosity and thermal conductivity results obtained with Chung et al. model and REFPROP (a).

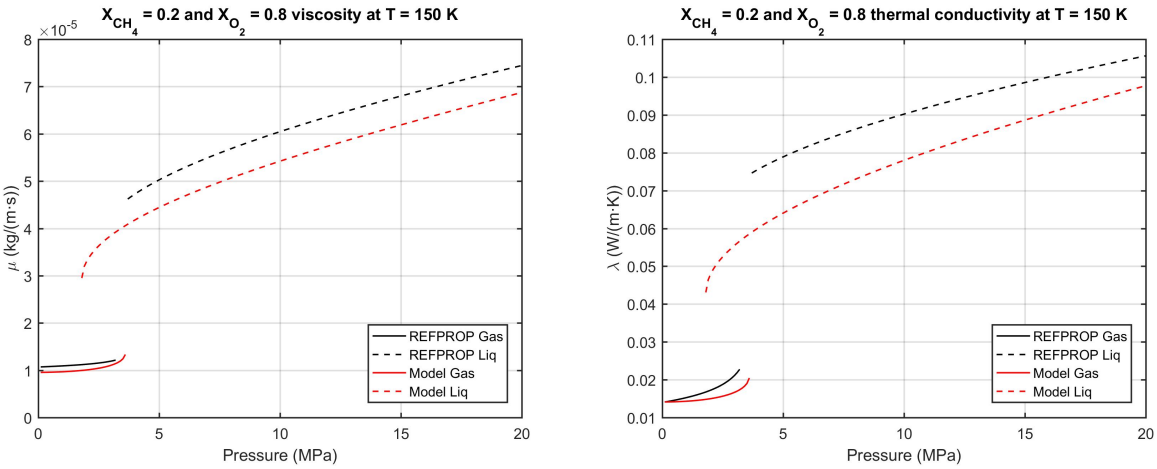

Figure E.6: Comparison of viscosity and thermal conductivity results obtained with Chung et al. model and REFPROP (b).

The most controversial model validation is perhaps the model used to compute the binary diffusion coefficients, Leahy-Dios and Firoozabadi model [47]. Validation results obtained from their paper prove the good performance of the model when compared to experimental data and other works (Figure E.7, source [47]).

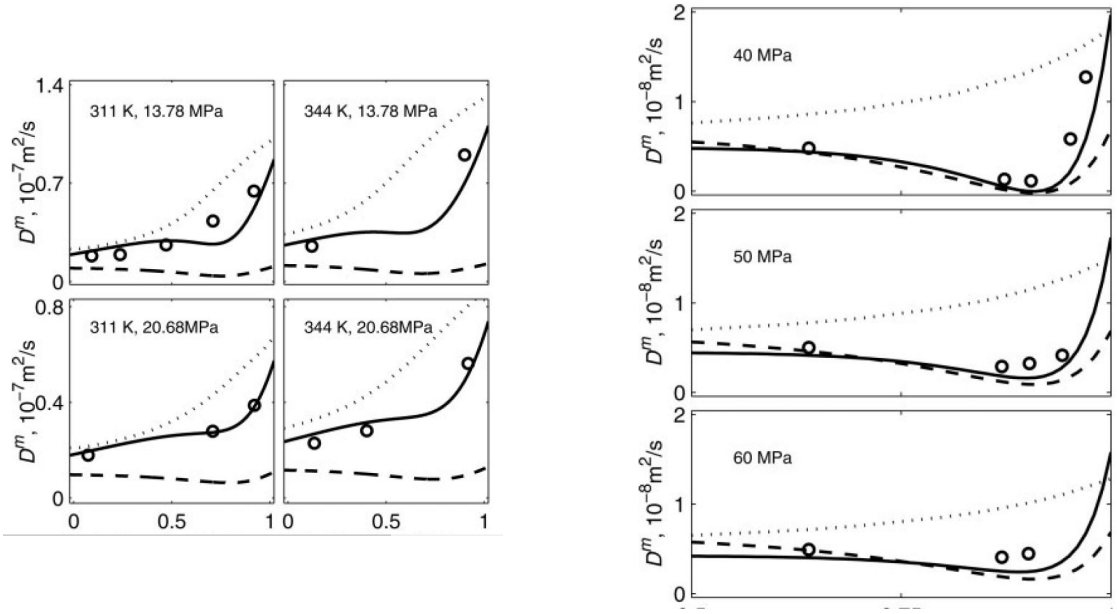

Figure E.7: Validation plots for the diffusion coefficient model of Leahy-Dios and Firoozabadi. Circles represent experimental data and continuous line represent the model. Methane/propane mixture (left) and methane/decane mixture (right). Methane mole fraction is represented in the x-axis (source [47]).

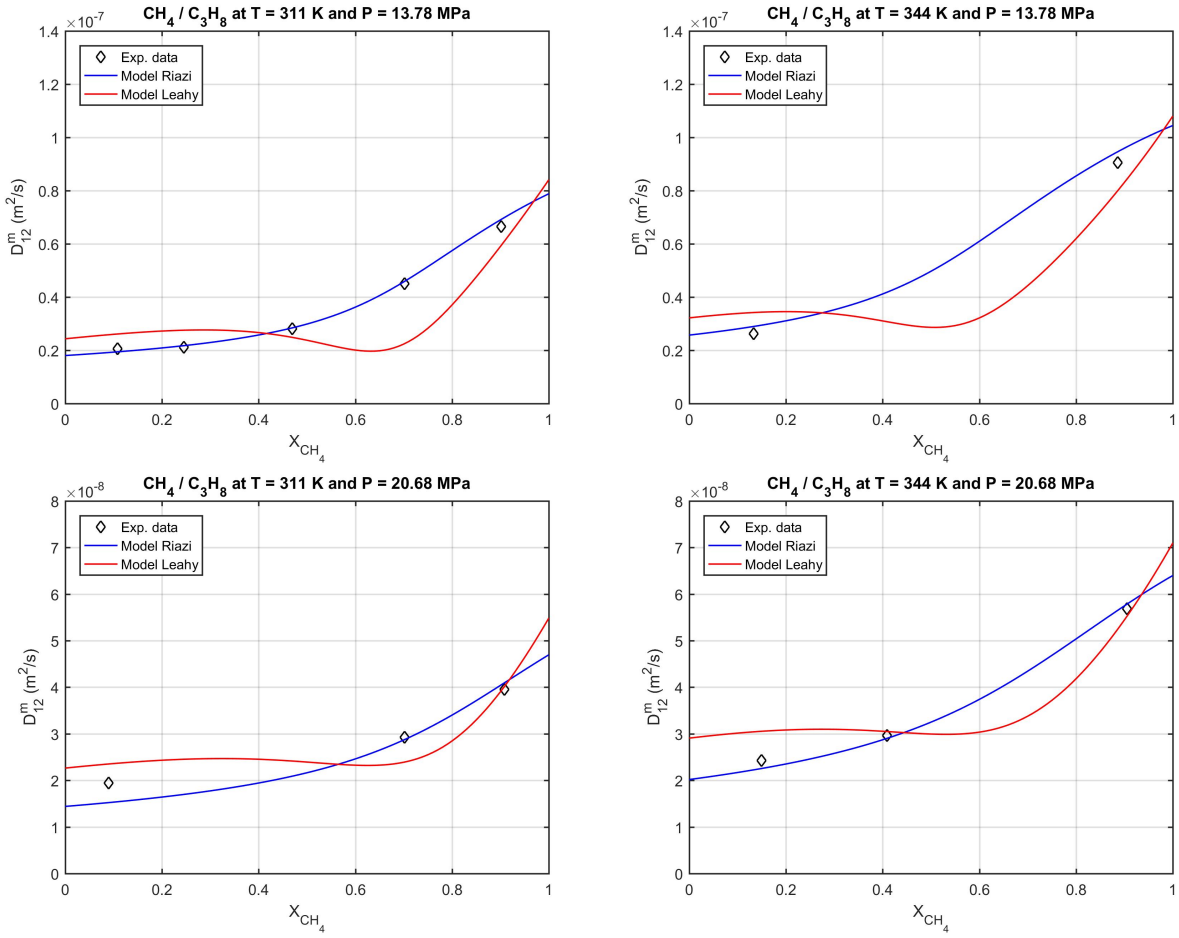

Figure E.8: Comparison of diffusion coefficients results obtained with Leahy-Dios and Firoozabadi model, Riazi and Whitson model and experimental data (a).

However, application of this model in our code provides different results, but of the same order of magnitude, as shown in Figure E.8 and Figure E.9. These differences are mainly due to the facts commented in the report. The model strongly depends on density computation, which is one of the weaknesses of the SRK-EoS in the liquid phase, and which also affects the viscosity computation, another parameter involved in the diffusion model. Furthermore, the non-ideality parameter or thermodynamic factor, Γ, introduced in Eq. 2.53, also depends on the equation of state being used and the influence of the binary interaction parameters k_{ij}. All these interactions affect the results obtained with the Leahy-Dios and Firoozabadi model applied to our code. The work done by Leahy-Dios uses high-fidelity equations of state and correlations to compute the necessary properties when experimental data is not available.

Thus, refining our models, especially the liquid density computation, would improve the performance of the diffusion model in our work.

We can see that Riazi and Whitson model performs well for the computations done for the mixture of methane and propane (Figure E.8). Nevertheless, this model only works well for some cases since its data bank includes few mixtures. For instance, Figure E.9 proves that its application to mixtures other than those appearing in its data bank do not show the expected properties of non-ideal diffusion (i.e., tending to zero as the mixture approaches the critical point).

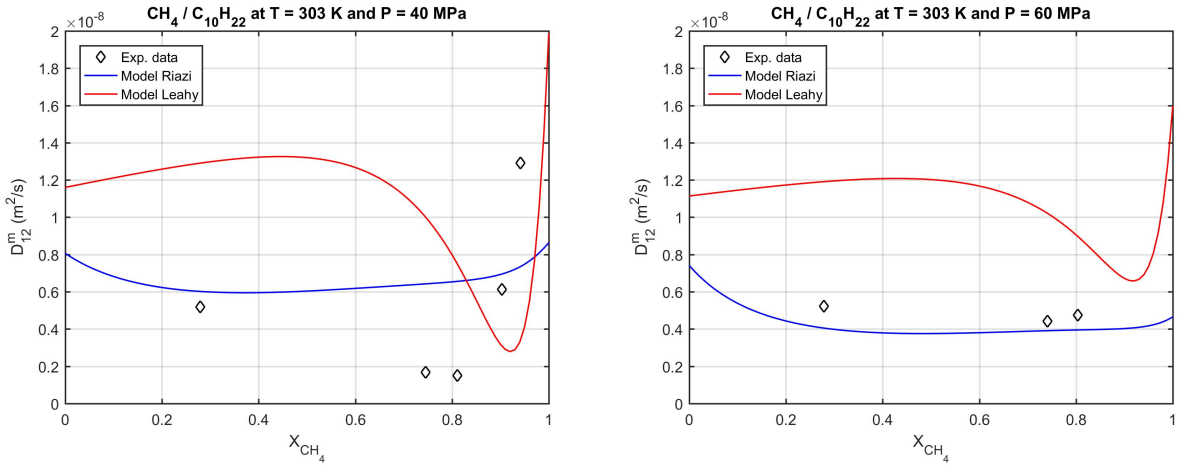

Figure E.9: Comparison of diffusion coefficients results obtained with Leahy-Dios and Firoozabadi model, Riazi and Whitson model and experimental data (b).

In summary, this model has been selected because of its expected good performance once the other models of our code are improved. At this stage, it is still capable of providing accurate and reasonable values for the diffusion coefficients.

Appendix F

Nitrogen/n-Octane Mixture Results

Pressure effects

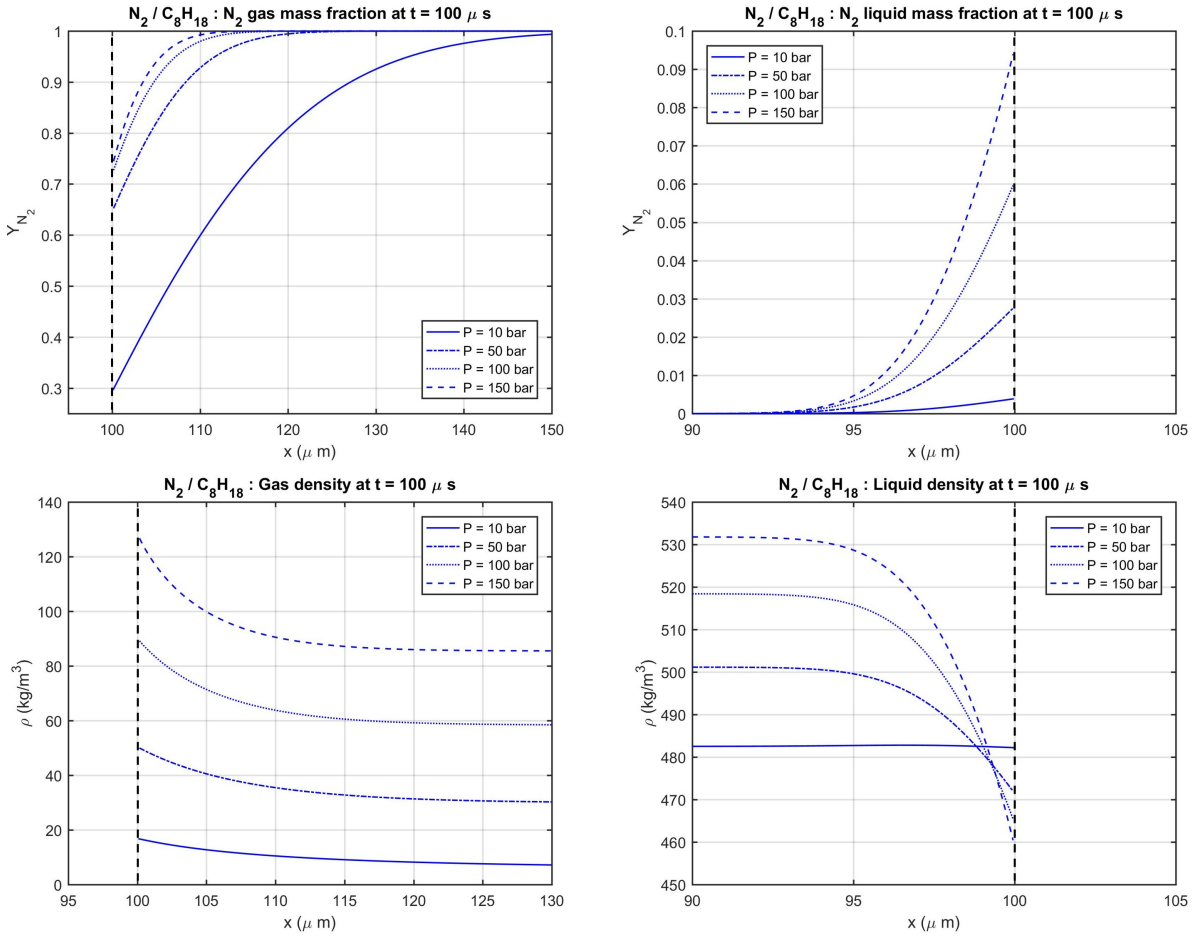

Figure F.1: Oxygen mass fraction and fluid density on each side of the interface for the nitrogen/n-octane mixture.

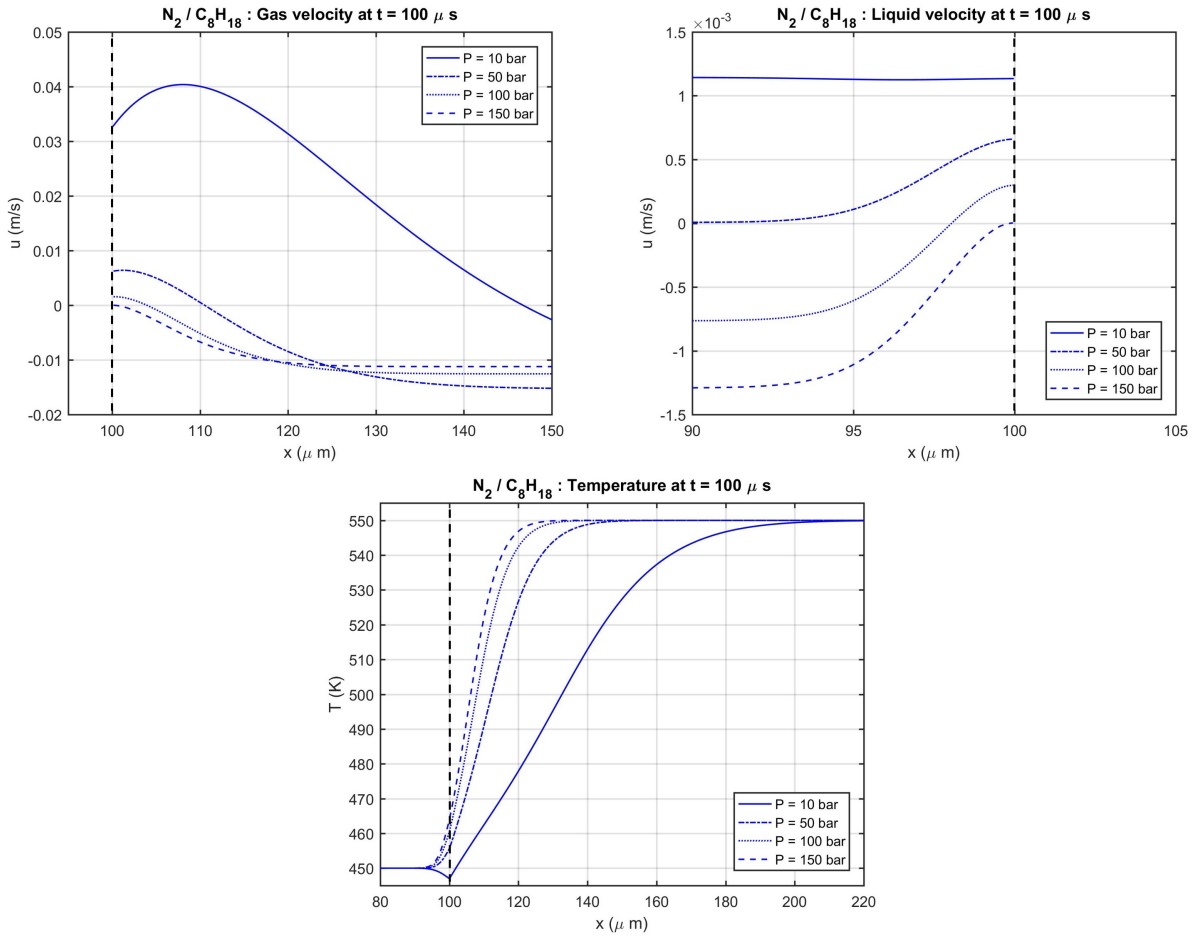

Figure F.2: Fluid velocity and temperature distribution for the nitrogen/n-octane mixture.

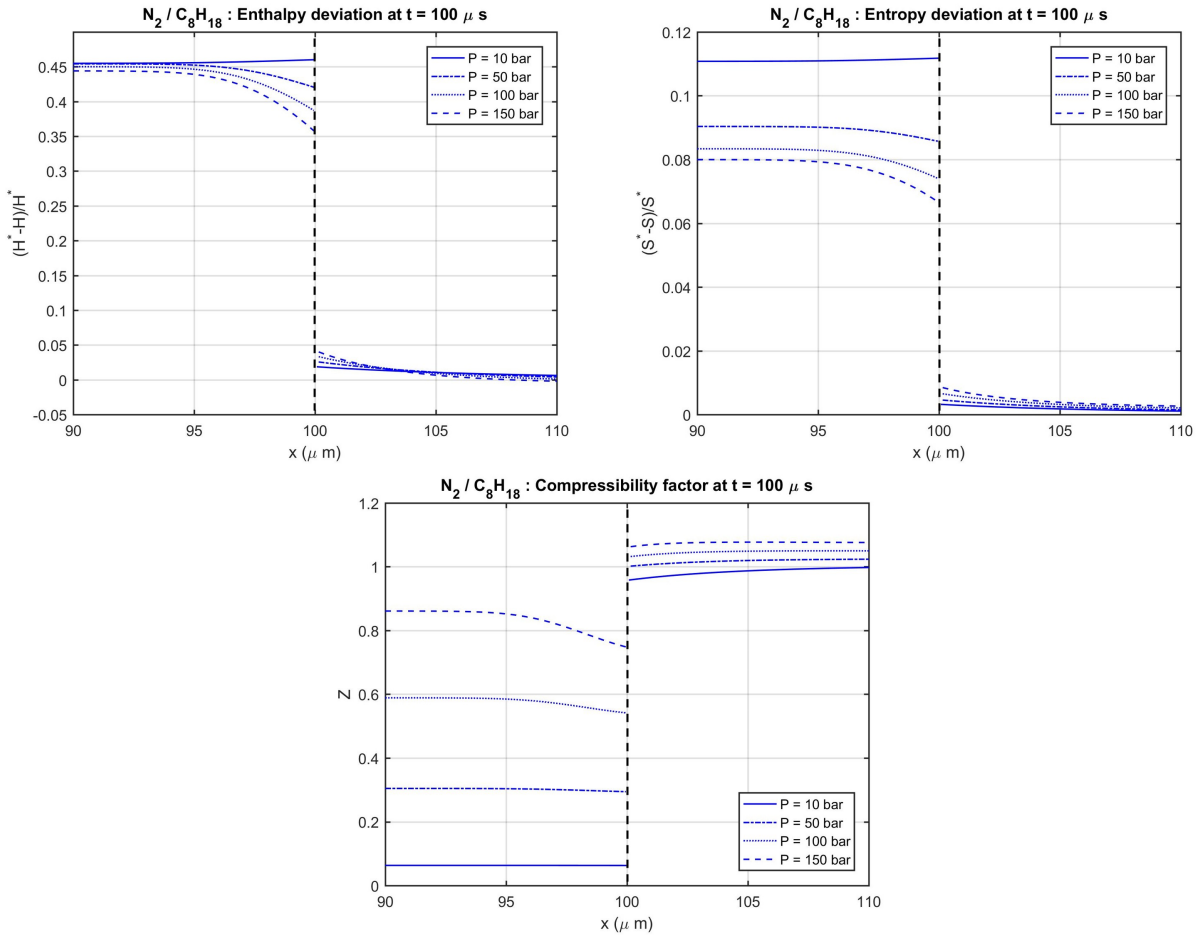

Figure F.3: Deviations from the ideal case for the nitrogen/n-octane mixutre.

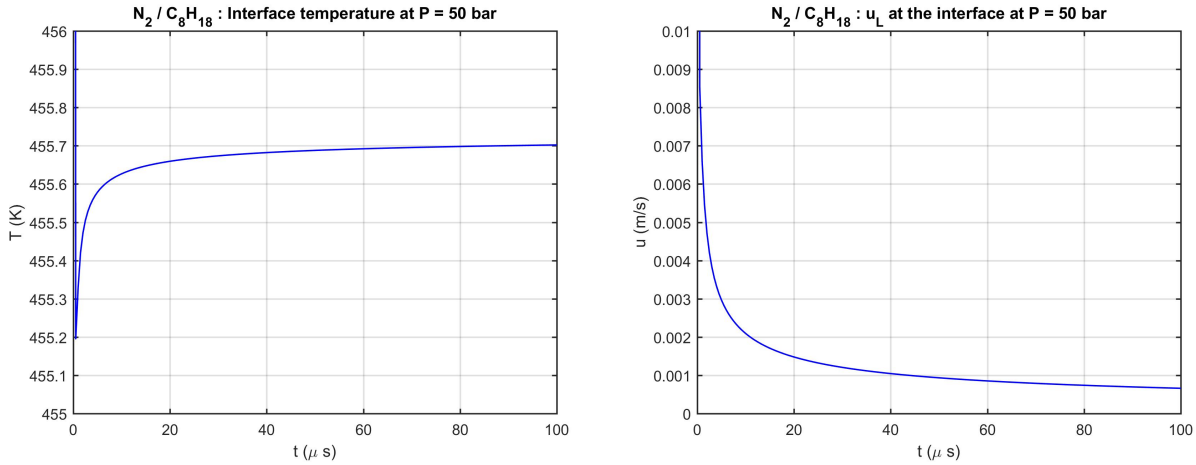

Figure F.5: Temperature and liquid velocity at the interface for the nitrogen/n-octane mixture.

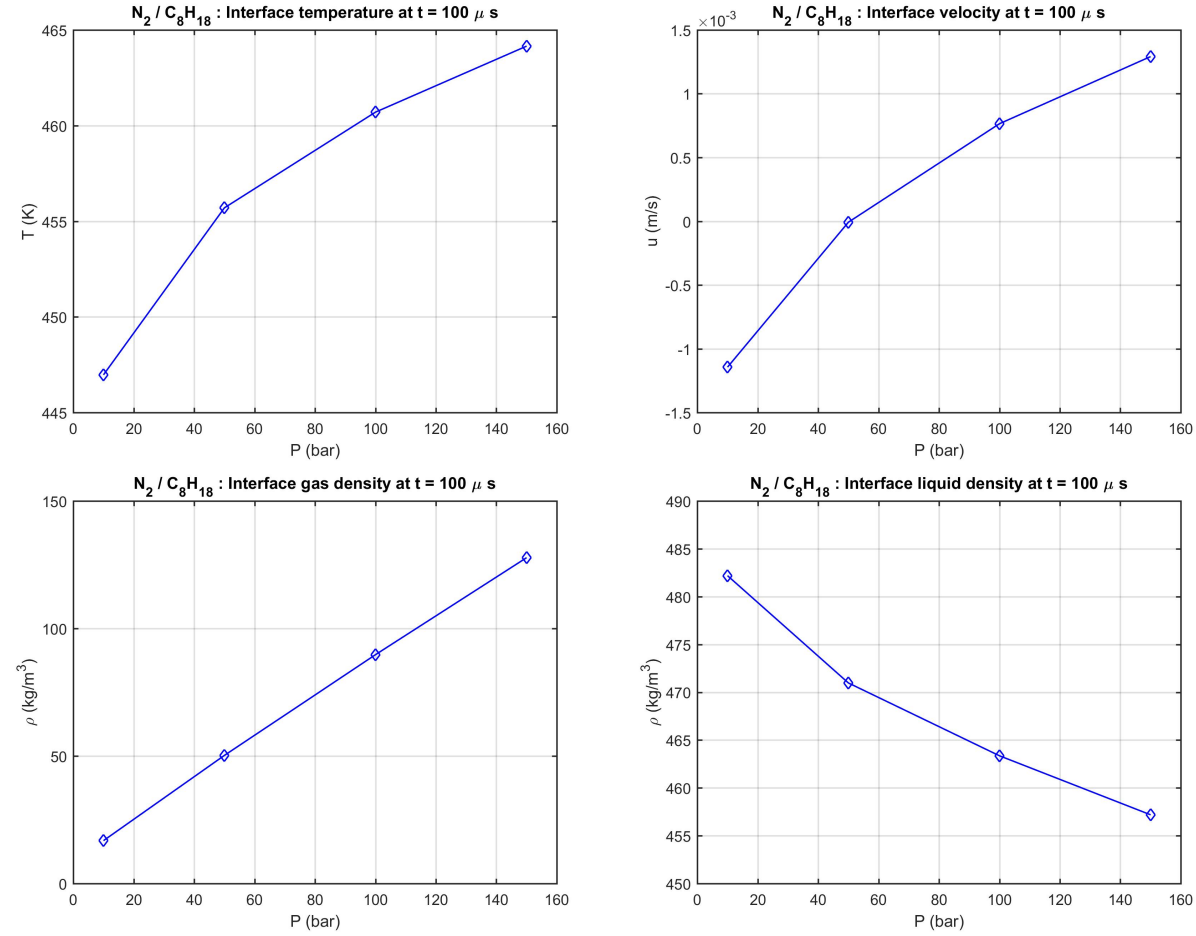

Figure F.5: Variation of interface properties with pressure for the nitrogen/n-octane mixture.

Temporal evolution

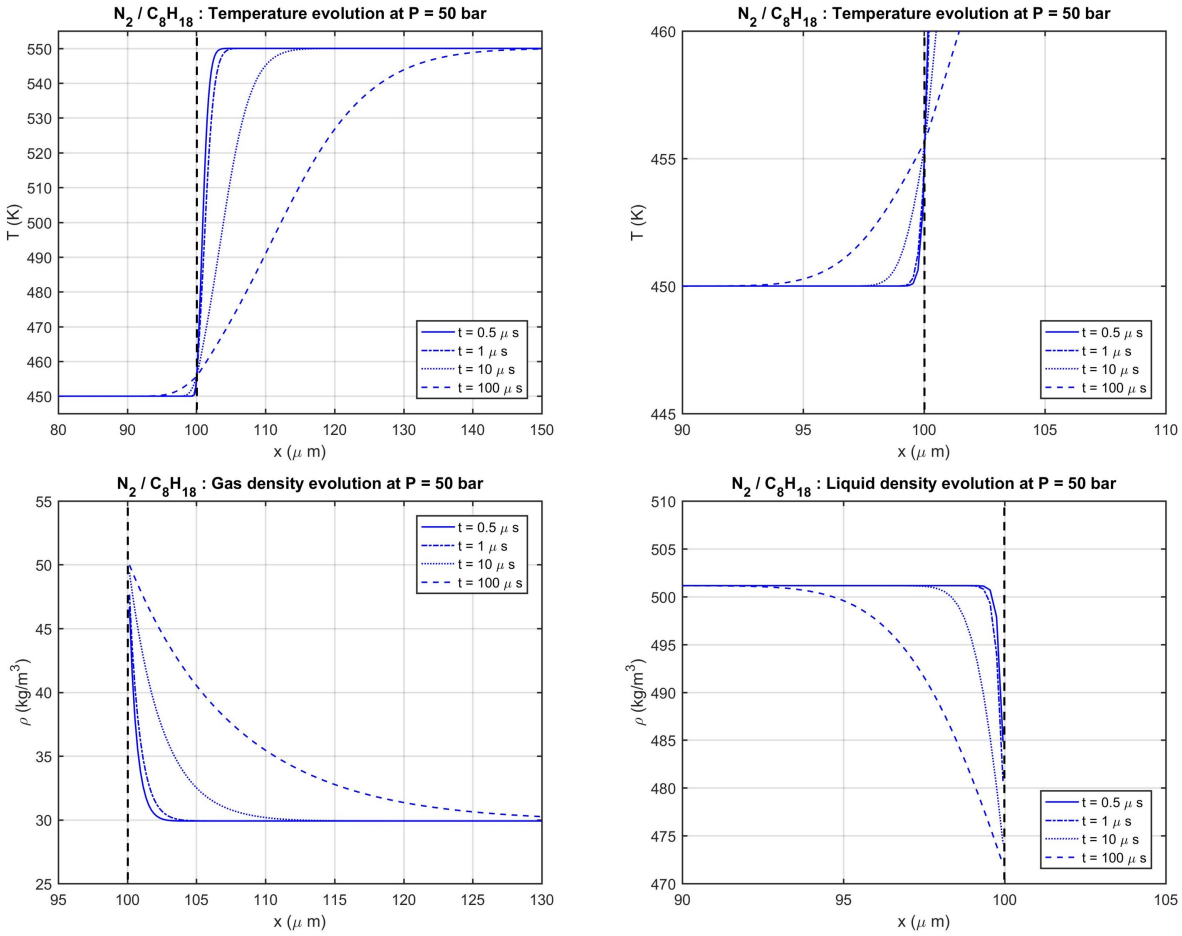

Figure F.6: Temporal evolution of the temperature distribution and the fluid density for the nitrogen/n-octane mixture at p = 50 bar.

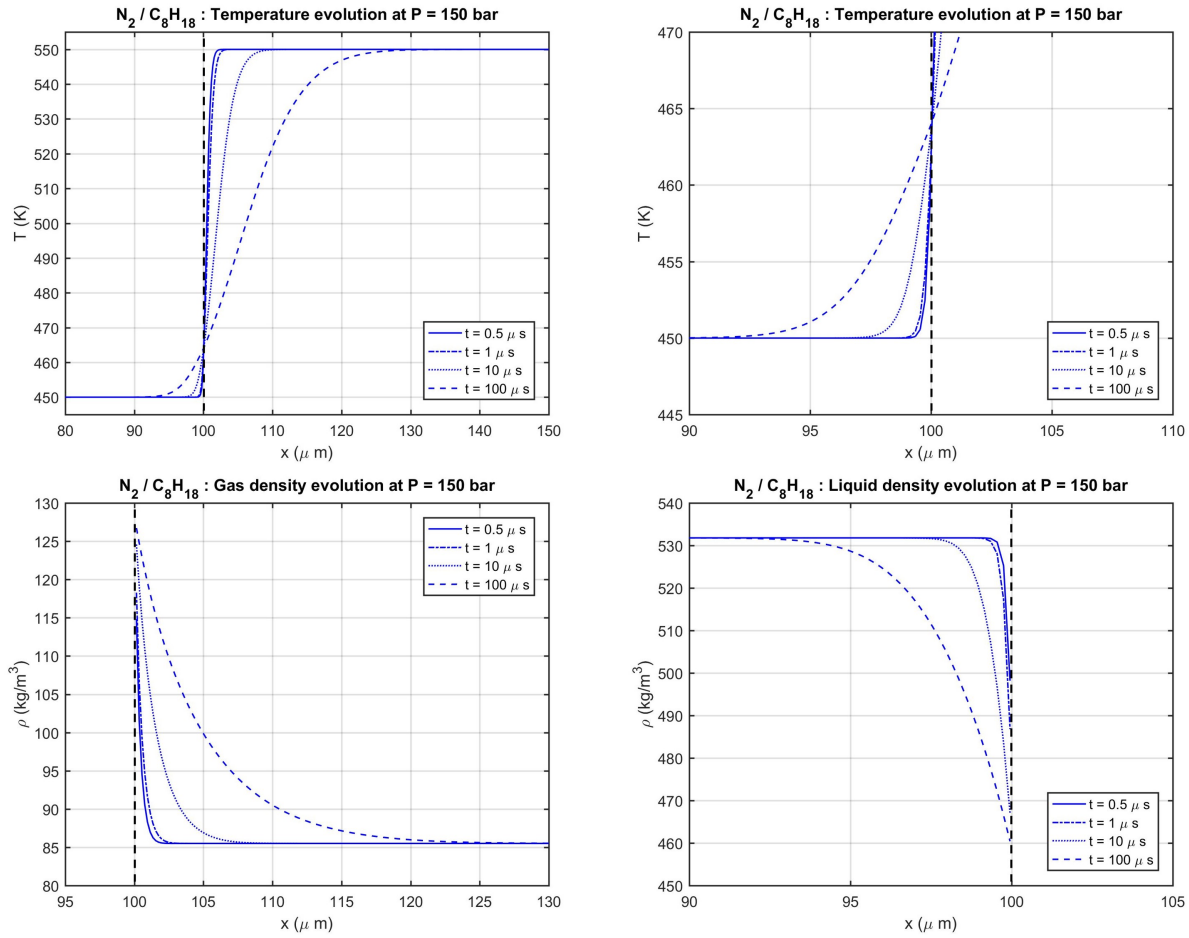

Figure F.7: Temporal evolution of the temperature distribution and the fluid density for the nitrogen/n-octane mixture at p = 150 bar.